J. Fluid Mech. (2010), *vol.* 659, *pp.* 127–190.
doi:10.1017/S0022112010002351

Detailed measurements of a statistically steady Rayleigh–Taylor mixing layer from small to high Atwood numbers

ARINDAM BANERJEE[1]†, WAYNE N. KRAFT[2] AND MALCOLM J. ANDREWS[2,3]

[1]Department of Mechanical and Aerospace Engineering, Missouri University of Science and Technology, Rolla, MO 65409, USA

[2]Department of Mechanical Engineering, Texas A&M University, College Station, TX 77840, USA

[3]Los Alamos National Laboratory, Los Alamos, NM 87545, USA

(Received 22 January 2009; revised 16 April 2010; accepted 18 April 2010)

The self-similar evolution to turbulence of a multi-mode miscible Rayleigh–Taylor (RT) mixing layer has been investigated for Atwood numbers 0.03–0.6, using an air–helium gas channel experiment. Two co-flowing gas streams, one containing air (on top) and the other a helium–air mixture (at the bottom), initially flowed parallel to each other at the same velocity separated by a thin splitter plate. The streams met at the end of the splitter plate, with the downstream formation of a buoyancy unstable interface, and thereafter buoyancy-driven mixing. This buoyancy-driven mixing layer experiment permitted long data collection times, short transients and was statistically steady. Several significant designs and operating characteristics of the gas channel experiment are described that enabled the facility to be successfully run for $A_t \sim 0.6$. We report, and discuss, statistically converged measurements using digital image analysis and hot-wire anemometry. In particular, two hot-wire techniques were developed for measuring the various turbulence and mixing statistics in this air–helium RT experiment. Data collected and discussed include: mean density profiles, growth rate parameters, various turbulence and mixing statistics, and spectra of velocity, density and mass flux over a wide range of Atwood numbers ($0.03 \leqslant A_t \leqslant 0.6$). In particular, the measured data at the small Atwood number (0.03–0.04) were used to evaluate several turbulence-model constants. Measurements of the root mean square (r.m.s.) velocity and density fluctuations at the mixing layer centreline for the large A_t case showed a strong similarity to lower A_t behaviours when properly normalized. A novel conditional averaging technique provided new statistics for RT mixing layers by separating the bubble (light fluid) and spike (heavy fluid) dynamics. The conditional sampling highlighted differences in the vertical turbulent mass flux, and vertical velocity fluctuations, for the bubbles and spikes, which were not otherwise observable. Larger values of the vertical turbulent mass flux and vertical velocity fluctuations were found in the downward-falling spikes, consistent with larger growth rates and momentum of spikes compared with the bubbles.

Key words: instability, turbulent flows, turbulent mixing

† Email address for correspondence: banerjeea@mst.edu

1. Introduction

Rayleigh–Taylor (RT) instability (Taylor 1950; Rayleigh 1884) occurs when a heavy fluid is placed over a light fluid in a gravitational field. Infinitesimal perturbations at the interface initially grow exponentially according to linear stability theory (Chandrasekhar 1961), and eventually saturate (Youngs 1984). Once in the nonlinear saturation regime, dimensional analysis suggests that the RT mixing half-width h grows quadratically with time according to the relation, $h \propto gt^2$, where t is time and g is the acceleration due to gravity. However, experiments and computations (Anuchina *et al.* 1978; Youngs 1984) suggest that a more complete description is given by

$$h_{b,s} = \alpha_{b,s} A_t g t^2 \quad (b: \text{bubble}; s: \text{spike}), \tag{1.1}$$

where the Atwood number A_t denotes the non-dimensional density difference defined by $A_t \equiv (\rho_1 - \rho_2)/(\rho_1 + \rho_2)$; ρ_1 and ρ_2 are the densities of air (heavy fluid) and air–helium mixture (light fluid) employed in the present work; h_b and h_s are the heights above/below the initial density interface of the edge of the mixing region: the 'rising' edge denoted as bubbles, while the 'falling' edge is designated as spikes; α_b and α_s denote observable growth rate parameters (for the bubbles and spikes). For low Atwood numbers (< 0.1), the RT mixing layer is practically symmetric ($h_b \sim h_s$) and α is usually taken as a constant (Snider & Andrews 1994; Dimonte & Schneider 2000; Ramaprabhu & Andrews 2004), i.e. $\alpha_b = \alpha_s = \alpha$. However, for high Atwood numbers ($\geqslant 0.1$), the RT mixing layer becomes increasingly asymmetric about the position of the initial density interface. Measured values of α_b and $\alpha_s$are found to be different (Dimonte & Schneider 1996), such that $\alpha_b < \alpha_s$, with α_s being a function of the Atwood number and α_b being approximately constant (Dimonte & Schneider 1996; Ramaprabhu & Andrews 2004).

Our main application of interest is the implosion phase of an inertial confinement fusion (ICF) capsule, where RT mixing is formed at high Atwood numbers (Clarke, Fisher & Mason 1973; Betti *et al.* 2001; Atzeni & Meyer-ter-Vehn 2004). However, in the compressible ICF problem, turbulent mixing is a low-Mach-number process and our incompressible and miscible experiment captures the same inertial dynamics associated with the fluid motion. However, since the present experimental set-up can be used over a wide range of Atwood numbers ($0 \leqslant A_t \leqslant 0.75$), it mimics a variety of other applications such as atmospheric instability associated with cold air overlaying warm air in the atmosphere (Molchanov 2004), or similar situations with cold and warm water in oceans, rivers or estuaries (Cui & Street 2004), buoyant jets (Marmottant & Villermaux 2004) and in finger-like ejecta of stellar materials present in the remnants of a young supernova (Gull 1975). Previously, several experiments have been performed to study high-Atwood-number RT mixing: the early experiments accelerated an initially stable stratified mixture of two fluids using various mechanisms like compressed air cans, rubber/elastic/bungee cords ($A_t \sim 0.99$) (Lewis 1950; Allred & Blount 1954; Emmons, Chang & Watson 1960; Cole & Tankin 1973; Ratafia 1973). The majority of these early experiments were single- or few-mode experiments. Subsequent experiments had multi-mode initial perturbations: Read (1984) used a drop-tank with $A_t \sim 0.231$–0.997 that was accelerated using rockets (Rocket Rig); and, in a similar experiment, Dimonte & Schneider (1996) studied a wide range of $A_t(0.1304$–$0.961)$ using a linear electric motor (LEM) to accelerate the tank. Linden *et al.* (1994) and Dalziel, Linden & Youngs (1999) began with a heavy fluid over a light fluid, the two fluids being separated by a plate. The plate was withdrawn and the buoyancy-driven mixing ensued between the two fluids. All these

experiments, with the exception of Linden *et al.* (1994) and Dalziel *et al.* (1999) were immiscible, involved short data collection times (∼milliseconds), and used backlit photography techniques that limited investigations to RT mixing layer width and growth rate parameters. Measurements could not be made of detailed turbulent statistics, i.e. Reynolds stresses, density–velocity correlations and their spectra, all of which lie at the heart of modern turbulence models for RT mixing.

We use an air–helium gas channel experimental facility (Banerjee & Andrews 2006) that permits long data collection times, short transients, and is statistically steady. Here we report work to measure the self-similar evolution of mixing at density differences over $0.03 \leqslant A_t \leqslant 0.6$, using digital image analysis and hot-wire anemometry. In particular, digital image analysis is used to measure statistically convergent RT mix density profiles (Snider 1994; Snider & Andrews 1994; Banerjee & Andrews 2006) at Atwood numbers of 0.04, 0.26, 0.47 and 0.6. In addition, we have also developed two different hot-wire techniques (Banerjee & Andrews 2007; Kraft, Banerjee & Andrews 2009) to measure various turbulent statistics inside the air–helium RT mixing layer. The first technique modifies the work of Rose (1973), and uses a multi-position multi-overheat (MPMO) single-wire technique (Banerjee & Andrews 2007) as a means to measure fluctuations of density, velocity and density–velocity correlations in our RT mixing layer at small and intermediate Atwood numbers ($A_t \leqslant 0.25$). The second technique uses simultaneous 3-wire/cold-wire anemometry (S3WCA) coupled with the concept of temperature as a fluid marker. The S3WCA has been used to measure instantaneous statistics inside the air–helium RT mixing layer (Kraft *et al.* 2009), and is suitable for large Atwood numbers of >0.25. We use results from the S3WCA technique to report the first detailed statistical measurements in a large-Atwood-number ($A_t = 0.6$) miscible RT mixing layer. Banerjee & Andrews (2006) presented multi-position single hot-wire (Bruun 1972) validation measurements at a small Atwood number of 0.035, that gave a late-time value for the growth parameter $\alpha(=\alpha_b = \alpha_s)$ of 0.065–0.07. Here we report the measurement of $\alpha_{b,s}$ up to $A_t = 0.6$ that employs four different measurement methodologies and formulas, and we show how the resulting values are essentially the same measurement, thus closing the loop on a long-standing source of confusion. Both the hot-wire methods used in the current work improve over the multi-position single-wire (MPSW) technique (Banerjee & Andrews 2006), by simultaneously measuring both density and velocity statistics, while our previous work gave only velocity data. We also report a novel conditional averaging technique that provides the first conditional statistics for RT mixing layers by separating the bubble (light fluid) and spike (heavy fluid) dynamics. The conditioning highlights differences in the vertical turbulent mass flux and vertical velocity fluctuations for the bubbles and spikes, which are not otherwise observable. Larger values of the vertical turbulent mass flux and vertical velocity fluctuations were found in the downward-falling spikes, which is consistent with the larger growth rates and momentum of the spikes compared with the bubbles.

2. Experimental set-up and procedures

A schematic of the experimental set-up is shown in figure 1. Two gas streams flow parallel at the same velocity (no shear) separated by a thin splitter plate. The top stream is air (heavy), at density ρ_1, while the bottom stream is a mixture of air and helium (light) at density ρ_2. The streams meet at the end of the splitter plate leading to formation of an unstable interface, and a buoyancy-driven RT mixing layer. This statistically steady buoyancy-driven mixing experiment, with miscible fluids, allows

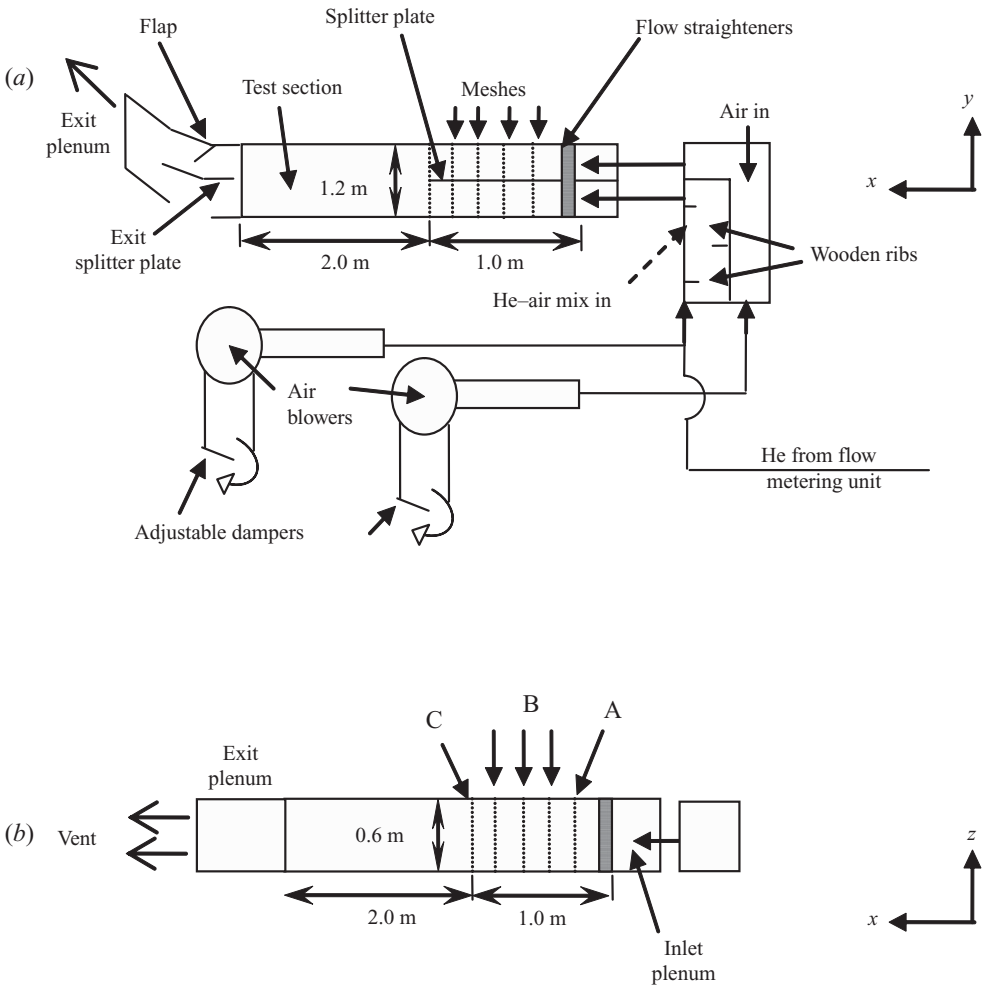

FIGURE 1. Schematic of the air–helium (He) gas channel facility ($0 < A_t < 0.75$). (a) Side view; (b) top view.

long data collection times, short transients, and is capable of large-Atwood-number studies ($0 \leqslant A_t \leqslant 0.75$) by altering the proportion of helium in the helium–air mixture in the bottom stream.

As shown in figure 1, the apparatus consists of inlet and exit plenums connected by a Plexiglas flow channel that serves as the test section. The test section is 2.0 m long, 1.2 m wide and 0.6 m deep, and is scaled up from the water channel experiment (same aspect ratio) reported in Snider & Andrews (1994) and Ramaprabhu & Andrews (2004). Snider & Andrews (1994) studied the influence of the distance between the front and back walls on the development of the RT mixing layer, and found that the width should be at least half of the depth to avoid late-time interference with the development of large structures. Moreover, they indicated that the RT mixing width is not affected by the top and bottom walls until the channel is at least 80 % filled. Both criteria were fulfilled in the present experiment. The inlet plenum is divided into two sections, connected to separate direct drive air blowers (1800 CFM at 1.5 in. static pressure, Dayton Inc.) that draw air from the atmosphere. The flow velocity

Mesh size	Wire diameter	% Open area	Letter in figure 1	Distance from C	Quantity
30×30	0.0340 cm	37.1 %	A	100 cm	1
30×30	0.0216 cm	55.4 %	B	10, 30 and 60 cm	3
22×22	0.0330 cm	49.8 %	C	0 cm	1

TABLE 1. The flow straightener and meshes in the inlet section of the facility. (Note: for location of each of the screens, see figure 1.)

is controlled by adjusting the opening of dampers connected to the suction port of the blowers. A maximum flow velocity in the test section of $2\,\mathrm{m\,s^{-1}}$ is available, having been determined to be sufficient to give a parabolic flow (i.e. mixing half-width grows as t^2) downstream from the splitter plate for the maximum available $A_t \sim 0.75$ (Snider 1994). In addition, a series of high-pressure regulators (Tescom Inc.) and an orifice plate meter helium at a constant mass flow rate into the lower section of the inlet plenum (Banerjee & Andrews 2006). Helium and air streams are uniformly mixed before they reach the inlet section by passing the streams around a series of wooden ribs placed inside the ductwork. A stainless steel splitter plate extends from the channel entrance to the start of the test section and separates the two streams of gas. The splitter plate is 0.32 cm thick, 1.0 m long and has a 1.8° knife edge at the end.

The top and bottom inlet sections of the channel are fitted with screens and flow straighteners to produce a uniform flow, assist in dissipating free-stream turbulence and minimize boundary-layer development on the splitter plate and walls (Brown & Roshko 1974; Browand & Weidman 1976; Stillinger *et al.* 1983; Snider & Andrews 1994; Banerjee & Andrews 2006). In particular, a 10 cm long polycarbonate honeycomb (0.635 cm in diameter) is placed at the entrance of each channel. The flow straightener is followed by four sets of screens; one 30×30 mesh (wires per inch) with a wire diameter of 0.034 cm (37.1 % free area), followed by three 30×30 meshes (wires per inch) with a 0.0216 cm wire diameter (55.4 % free area). A full channel screen placed at the end of the splitter plate was found to be effective in minimizing the wake from the splitter plate (Koop 1976). This end screen consists of a 22×22 mesh (wires per inch) with a 0.033 cm wire diameter, and has an open area of 49.8 % (see table 1). The honeycomb and meshes are placed sufficiently upstream to dissipate free-stream turbulence (Tan-Atichat, Nagib & Loehrke 1982), and the open area chosen was consistent with turbulence management recommendations for wind tunnels (Loehrke & Nagib 1972). The turbulence level in the free stream was experimentally measured 5 cm from the end mesh using a hot-wire (three-wire) anemometer and u'_{rms}/U, v'_{rms}/U and w'_{rms}/U were found to be $< 2\,\%$. Measurements reported by Ramaprabhu & Andrews (2004), using a water channel facility (similar in design and and flow conditions) measured negligible skewness for the axial velocity r.m.s. fluctuations, indicating a 'frozen' condition in the axial direction and thus justifying the Taylor hypothesis (Taylor 1938). Indeed, another criterion (Pope 2000) for the Taylor hypothesis is that $u'/\overline{U} \ll 1$, i.e. the axial velocity fluctuation is much less than the advective velocity. A small spread angle was designed in the experiment to ensure that the flow was parabolic, so that $w'/\overline{U} \ll 1$ (Snider & Andrews 1994). Ramaprabhu & Andrews (2004) reported that $u'/w' \approx 0.5$ and, thus, the $u'/\overline{U}$ criterion was also satisfied in the present experiment.

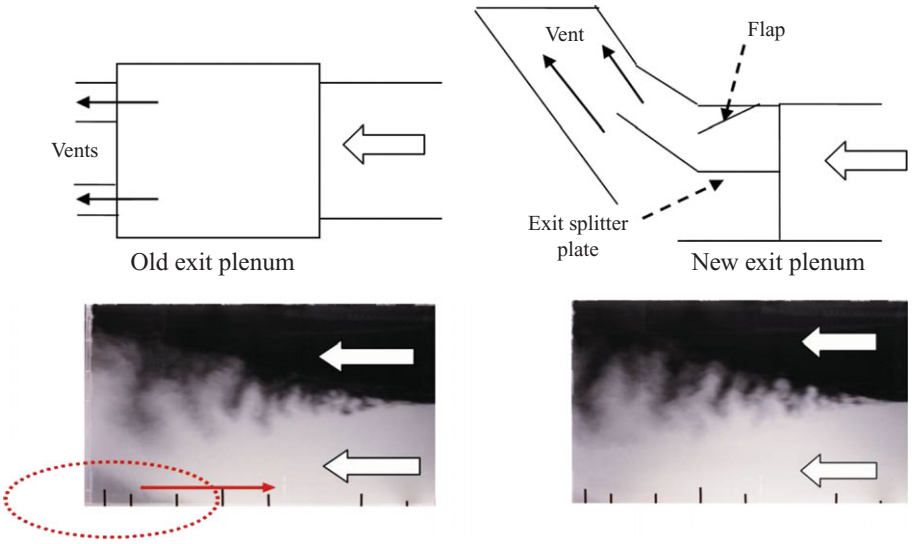

FIGURE 2. (Colour online) Schematic of design modifications in the exit plenum for high-Atwood-number experiments ($A_t > 0.1$) that eliminated gravity currents from flowing back into the test section. The arrows indicate the direction of flow. The Atwood number for the experiment is 0.259.

Preliminary experiments at $A_t \geqslant 0.1$ revealed the presence of gravity currents that induced a backflow from the exit plenum towards the splitter plate (see figure 2). Such back-flowing gravity currents were not observed in the small A_t ($=0.04$) experiments of Banerjee & Andrews (2006), but at $A_t \geqslant 0.1$, they were found to cause the centreline of the RT mixing layer to rise and interfere with the mixing process. The exit plenum was redesigned to eliminate these gravity currents by introducing an exit splitter plate that supported the heavy fluid and stopped it from falling to the bottom of the exit plenum. In addition, a flap was placed on the top half of the exit plenum and the opening was adjusted to keep the centreline horizontal for experiments up to Atwood numbers of 0.6. This design modification of the exit plenum solved a difficult problem for $A_t > 0.1$ experiments, and set the stage for high A_t experiments in the facility.

We briefly describe the operation of the facility, more details may be found in Banerjee & Andrews (2006). The Atwood number of the RT mix may be conveniently written as (Banerjee & Andrews 2006):

$$A_t = \frac{(\rho_1 - \rho_2)}{(\rho_1 + \rho_2)} = \frac{\left[\dfrac{\rho_{air}}{\rho_{He}} - 1\right] \dfrac{\dot{m}_{He}}{U_m A}}{2\rho_{air} - \left[\dfrac{\rho_{air}}{\rho_{He}} - 1\right] \dfrac{\dot{m}_{He}}{U_m A}}, \tag{2.1}$$

where $\dot{m}_{He}$ is the mass flow rate of helium, U_m is the mean flow velocity of the two streams ($U_{top} = U_{bottom} = U_m$) and A is the cross-sectional area of each stream. The temperature of each stream was measured and the densities of air and helium were obtained from equations of state (McCarty 1973; Jacobsen *et al.* 1990). The helium flow metering unit was designed based on a volumetric method (at constant outlet pressure), in which helium was delivered from a compressed supply having passed

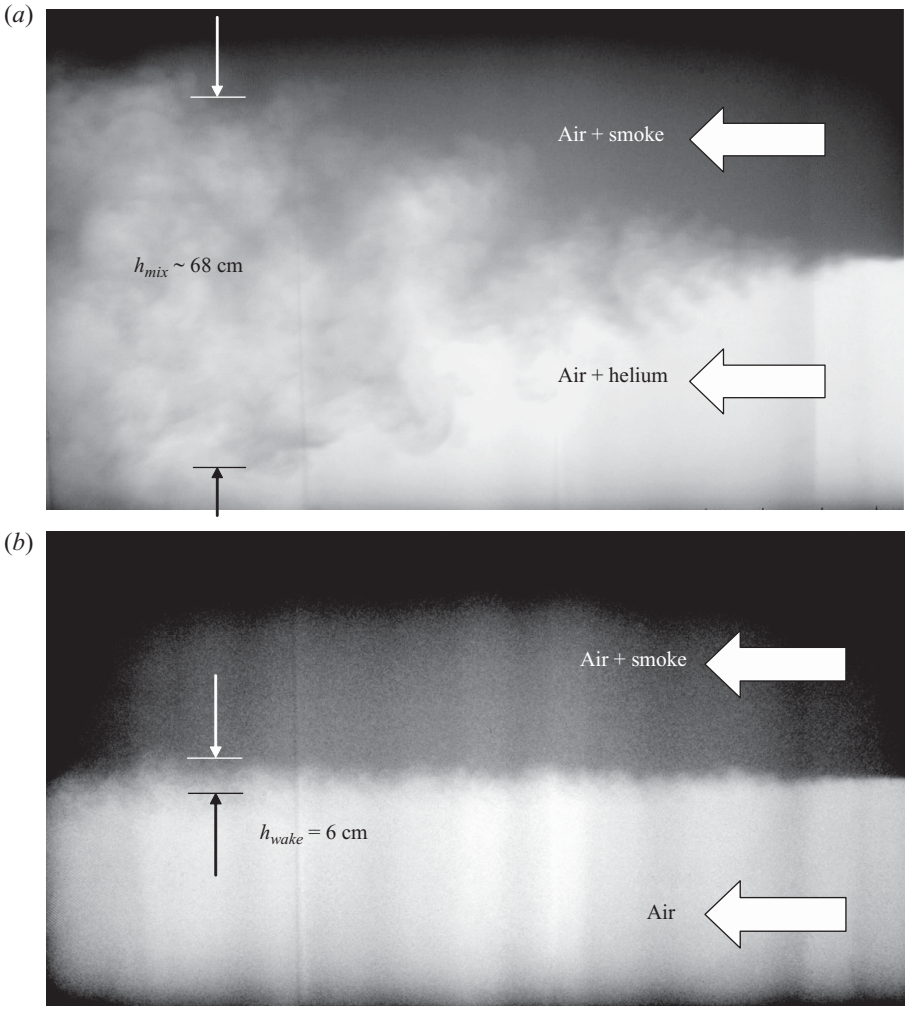

FIGURE 3. (*a*) View of the mixing process in the channel at $A_t = 0.47$; (*b*) development of the two fluid interface in the absence of shear and density gradients, i.e. at $A_t \sim 0$. The mean velocity for both the experiments is $U_m = 1.65\,\mathrm{m\,s^{-1}}$.

though an orifice (John 1984; Jitschin, Weber & Hartmann 1995). More details about the working principles of the flow metering unit and information on mass flow rate calibration at different Atwood numbers (using different orifices) can be found elsewhere (Banerjee 2006).

To illustrate the spatial and temporal RT mixing layer development within the gas channel an image of the RT mixing layer at an $A_t = 0.47$ ($U_m = 1.65\,\mathrm{m\,s^{-1}}$) is shown in figure 3(*a*). The inlet is on the right, and the outlet is on the left. Dark green smoke was added to the top (denser) stream for visualization purposes. At a location 1.75 m downstream from the splitter plate, the width of the RT mixing layer is ~68 cm. To demonstrate that the RT mixing layer is primarily due to buoyancy, and not due to the wake of the splitter plate, the gas channel was run at $A_t \sim 0$ with air on top and bottom (the neutral buoyancy case). Figure 3(*b*) shows a photograph of the interface between the two air streams that both flow at velocities of $U_m = 1.65\,\mathrm{m\,s^{-1}}$.

	$A_t = 0.04$		$A_t = 0.26$		$A_t = 0.47$		$A_t = 0.6$	
x (cm)	τ	τ_α	τ	τ_α	τ	τ_α	τ	τ_α
50	0.567	0.644	0.603	0.726	0.589	0.695	0.549	0.603
75	0.851	1.448	0.904	1.634	0.884	1.563	0.824	1.358
100	1.135	2.575	1.205	2.906	1.179	2.778	1.099	2.414
125	1.418	4.023	1.507	4.54	1.473	4.341	1.373	3.772
150	1.702	5.793	1.808	6.538	1.767	6.251	1.648	5.431
175	1.986	7.885	2.109	8.898	2.063	8.508	1.923	7.393
195	2.213	9.791	2.350	11.049	2.298	10.564	2.142	9.179

TABLE 2. Non-dimensional time scales: $\tau = (x/U_m)(A_t g/H)^{1/2}$ used in present experiments and corresponding 'α'-group (Dimonte *et al.* 2004): $\tau_\alpha = A_t g t^2/(H/2)$ values.

The thickness of the mixing layer formed by the wake for this no buoyancy case is < 6 cm (at a location 1.75 m downstream from the splitter plate), with no apparent flow structures that would result in significant mixing. Thus, the primary driving mechanism for the RT mixing layer is buoyancy, and mixing due to the wake of the splitter plate is considered to be negligible in the far field.

Inspection of the photograph in figure 3(*a*) for $A_t = 0.47$ reveals small interfacial perturbations on the right-hand side (upstream, inlet) of the photograph, which grow, interact and merge to form the RT mixing layer seen on the left-hand side (downstream, exit). The distance downstream, x, is converted to time, $t = x/U_m$, using the Taylor hypothesis (Taylor 1938; Pope 2000), where U_m is the mean convective velocity of the channel flow (in this experiment the top and bottom streams flow at the same speed so there is no superimposed shear). A non-dimensional time τ is employed that uses the characteristic buoyancy time scale (Snider & Andrews 1994; Dalziel *et al.* 1999; Ramaprabhu & Andrews 2004; Mueschke, Andrews & Schilling 2006) as

$$\tau \equiv t\left(\frac{A_t g}{H}\right)^{1/2} = \frac{x}{U_m}\left(\frac{A_t g}{H}\right)^{1/2}, \tag{2.2}$$

where g is the acceleration due to gravity and H is the depth of the channel. An alternate non-dimensional time $\tau_\alpha (\equiv A_t g t^2/(H/2))$ has been used in RT simulations (Dimonte *et al.* 2004), and the two non-dimensional times are related as $\tau = (\tau_\alpha/2)^{1/2}$. Values of τ and τ_α for our measurement positions are listed in table 2 to facilitate comparison between the two non-dimensional time scales.

3. Theory

3.1. *Reynolds number definitions for Rayleigh–Taylor mixing*

In our buoyancy-driven mix with no shear, the mean convective velocity does not contribute to the dynamics of the mix, and so the definition of Reynolds number often becomes a matter of personal preference that depends on the choice of a suitable velocity scale. For low Atwood numbers ($A_t < 0.1$), when the RT mixing layer is symmetric ($h_s = h_b = h$), Snider & Andrews (1994) formulated a Reynolds number based on a balance of kinetic and potential energy that is given as

$$Re_1 = \frac{2h}{\nu_{mix}}\sqrt{\frac{1}{3} g A_t h}. \tag{3.1}$$

Cook & Dimotakis (2001) defined a Reynolds number by using the whole RT mix-width ($h_t = h_b + h_s$) as the length scale and its time derivative ($\dot{h}_t$) as the corresponding characteristic velocity scale:

$$Re_2 = \frac{h_t \dot{h}_t}{\nu_{mix}}. \tag{3.2}$$

Daly (1967) suggested that $\dot{h} \propto \sqrt{A_t g h}$; i.e. the mix-width growth rate is proportional to the terminal velocity of an RT instability of wavelength h. Thus, it is apparent that (3.2) is similar in form to the definition of Snider & Andrews (1994).

However, at high Atwood numbers ($A_t > 0.1$), the RT mixing layer is asymmetric and a Reynolds number based on the total RT mix-width will not capture the asymmetries in the bubble and spike penetrations. To incorporate different levels of turbulence in each half of the mix (the bubble and spike sides), (3.2) may be modified to incorporate separate Reynolds numbers based on bubbles and spike velocities as

$$Re_b = \frac{h_b \dot{h}_b}{\nu_{mix}}; \quad Re_s = \frac{h_s \dot{h}_s}{\nu_{mix}}. \tag{3.3}$$

Goncharov (2002) formulated an analytical model of the nonlinear bubble evolution for a single-mode classical RT instability for arbitrary Atwood numbers. The model provides a continuous bubble evolution from the early time exponential growth to the late-time nonlinear regime. The bubble saturated to $\dot{h}_b = \sqrt{2A_t/(1+A_t)(g/k)}$, where k is the perturbation wavenumber. A similar expression for the spikes gives $\dot{h}_s = \sqrt{2A_t/(1-A_t)(g/3k)}$. Substituting these expressions for bubble and spike velocity in (3.3), we can modify the definition of Reynolds number for the bubble and spikes as

$$Re_b = \frac{h_b}{\nu_{mix}} \sqrt{\frac{2A_t}{1+A_t} \frac{g}{k}}; \quad Re_s = \frac{h_s}{\nu_{mix}} \sqrt{\frac{2A_t}{1-A_t} \frac{g}{3k}}. \tag{3.4}$$

Re_s shows a strong dependence on the Atwood number of the flow, which is also observed in our experiment as the measured value of α_s increases with an increase in the Atwood number. The bubble Reynolds number (Re_b) exhibits a weak dependence on the Atwood number and as a result α_b is approximately constant for the range of Atwood numbers reported here. Goncharov's (Goncharov 2002) theoretical predictions are based on a single-mode model and illustrate the associated asymmetry in the bubble and spike penetrations and the different levels of turbulence (and Reynolds number) in each half of the mix. The growth rates for our multi (many) mode experiments illustrate similar asymmetry in bubbles and spikes amplitudes and are calculated from conditioned hot-wire measurements of spike and bubble velocities. The mean kinematic viscosity ν_{mix} is calculated according to $\nu_{mix} = (\mu_l + \mu_h)/(\rho_l + \rho_h)$ (Youngs 1984). An alternate mixture viscosity was given by Wilke (1950):

$$\left.\begin{aligned} \mu_{mix} &= \mu_1 \left[1 + \frac{m_2}{m_1}\Phi_{12}\right]^{-1} + \mu_2 \left[1 + \frac{m_1}{m_2}\Phi_{21}\right]^{-1} \quad (l \to 1, h \to 2), \\ \text{where} \quad \Phi_{ij} &= \left[1 + \left(\frac{\mu_i}{\mu_j}\right)^{1/2} \left(\frac{M_j}{M_i}\right)^{1/4}\right]^2 \left[8\left(1 + \frac{M_i}{M_j}\right)\right]^{-1/2}, \quad i \neq j, \end{aligned}\right\} \tag{3.5}$$

with the molecular weights of the pure gases as M_1 and M_2, and the mole fraction of the individual components in the mixture as m_1 and m_2. The difference in ν_{mix} calculated based on the two methods is less than 1 % at small Atwood numbers (< 0.1).

For the present air–helium combination, when $A_t > 0.5$, the difference increases to $\sim 5.35\,\%$.

3.2. *Definition of molecular mix parameter*

The measure of molecular mixing, θ, used here was first introduced by Danckwerts (1952) as a degree of fluid segregation and defined as (Youngs 1994; Wilson & Andrews 2002)

$$\theta = 1 - \frac{B_0}{B_2}. \tag{3.6}$$

This parameter has been reported by various researchers (Dalziel *et al.* 1999; Cook & Dimotakis 2001; Cook, Cabot & Miller 2004; Ramaprabhu & Andrews 2004; Ristorcelli & Clark 2004; Cook & Cabot 2006; Mueschke *et al.* 2006, 2009) and provides a practical measure of molecular mixing as transport equations for $\overline{\rho'^2}$ and $\bar{\rho}$ can be derived, modelled and solved to predict mixing (Chassaing *et al.* 2002; Fox 2003). The density fluctuation self-correlation, B_0, includes the effect of mixing due to molecular diffusion and is defined as

$$B_0 = \lim_{T\to\infty} \frac{1}{T} \int_0^T \left(\frac{\rho - \bar{\rho}}{\Delta\rho} \right)^2 \mathrm{d}t = \overline{\rho'^2}/\Delta\rho^2, \tag{3.7}$$

where $\overline{\rho'^2}$ is the density variance and $\Delta\rho = \rho_1 - \rho_2$. B_2 is defined as the corresponding conditioned measure that would result if the two fluids were immiscible with no molecular mixing:

$$\left.\begin{aligned} B_2 &= f_1 f_2 = f_1(1 - f_1), \\ f_2 &= \lim_{T\to\infty} \frac{1}{T} \int_0^T \left(\frac{\rho - \rho_2}{\Delta\rho} \right) \mathrm{d}t, \end{aligned}\right\} \tag{3.8}$$

where f_1 is the fraction by volume of the heavy fluid, and f_2 is that of the light fluid with $f_2 = 1 - f_1$. Then $\theta = 0$ implies no molecular mixing, and $\theta = 1$ corresponds to completely molecularly mixed fluids (i.e. the density is uniform). At small Atwood numbers, the location of the initial interface corresponds to the centreline of the RT mixing layer. In the present RT mixing layer, B_0 has been found (Wilson & Andrews 2002) to couple with the mean pressure gradient as a primary source for the next mass flux due to turbulence, thus the destruction of B_0 by molecular diffusion might be expected to reduce the rate of growth of the RT mixing layer as smaller diffused scales of mixed fluid merge to form larger diffused scales that move towards the edge of the RT mixing layer (Steinkamp, Clark & Harlow 1995).

3.3. *Intermittency and conditional statistics in Rayleigh–Taylor mixing*

Since the RT mixing layer is dominated by 'rising' bubbles and 'falling' spikes, it is logical to define conditional statistics based on bubble and spike dynamics instead of the traditional turbulent non-turbulent separation which is done for shear layers. This approach is particularly useful at large Atwood numbers where asymmetries between the spikes and the bubbles were observed. Although conditional averaging techniques have been used extensively for shear-driven turbulent flows (Antonia 1981), the authors believe that the conditional measurements reported here are the first of their kind for RT experiments and allow investigation of interesting aspects in the buoyancy-driven mixing layer which is observed through conventional averaging techniques. We briefly review various conditional averaging measurements before discussing the bubble and spike dynamics of our RT mixing layer using conditioned measurements.

Early attempts to use conditional measurements for studying the dynamics of a shear layer were done by Wygnanski & Fiedler (1970), who used hot-wire diagnostics to conditionally average turbulent and non-turbulent flows using the signal: $|\partial^2 u'/\partial t^2| + (\partial u'/\partial t)^2$. However, these measurements were limited in their scope as they were performed using analogue data acquisition devices (Bruun 1995). With the advent of digital data acquisition technologies, it became more common to use a scalar as a fluid marker to conditionally sample the flow measurements as well as others parameter of interest. Conditional statistics reported by Fabris (1983*a*, *b*) used a temperature marker in a wake flow to distinguish between turbulent and potential fluid in the wake. LaRue & Libby (1980) used a scalar marker to obtain conditional statistics, using helium concentration to condition measurements of an air turbulent boundary layer entraining laminar flowing helium. Measurements were conditionally averaged according to specific ranges of helium concentration to identify the contributions of each fluid to the originally air only turbulent boundary layer. The hot-wire interference probe used by LaRue & Libby (1980) was limited to conditional measurements of concentration, and only the streamwise velocity fluctuations (u'). Conditional statistics are generally obtained using the indicator function or the intermittency function, $I(t)$ as

$$I(t) = H_s[\omega(t) - \omega_{threshold}], \tag{3.9}$$

where H_s is the Heaviside function, ω is vorticity and $\omega_{threshold}$ is a threshold chosen to identify turbulent fluid (Pope 2000) such that $I(t) = 1$ in turbulent flow, and $I(t) = 0$ if the flow is non-turbulent. The intermittency function of (3.9) can be modified to decompose the signal according to positive and negative values of any parameter, ϕ, as

$$I(t) = \frac{1 + \mathrm{sgn}[\phi(t)]}{2}. \tag{3.10}$$

4. Measurement diagnostics

4.1. *Visualization diagnostics*

The gas channel test section was backlit using a series of 35 fluorescent lamps, similar to those used by Snider & Andrews (1994). Frosted acetate paper served as the white background, and prismatic sheets were used between the lamps and acetate paper that diffused the light and made the background near uniform. Dark green smoke (RC105G, Regin HVAC) was added to one of the streams to visualize the RT mixing layer. For low-Atwood experiments ($A_t \sim 0.04$, 0.1 and 0.25), the smoke was added to the lighter stream (air–helium mixture). However, small amounts of air in the bottom stream ($\sim$22.63 % of air by volume) for the high-Atwood experiment ($A_t > 0.25$) prevented proper combustion of the smoke cartridges. Consequently, for the Atwood numbers 0.47 and 0.6 imaging experiments, smoke was added to the heavier fluid (pure air on top). The density of smoke (soot particles) emitted by the smoke cartridges is $\sim 888\,\mathrm{mg\,m^{-3}}$. For the Atwood number range of 0.04–0.6, the change in Atwood number due to addition of smoke varied between 0.03 %–0.25 % respectively, so the variation in Atwood number with addition of smoke was considered to be negligible.

Each experiment was photographed using a digital camera (Canon PowerShot A80) with a manually fixed focus. At the start of all experiments for $A_t < 0.6$, the camera shutter speed, aperture and ISO settings were fixed at 1/100 s, f/8.0 and 100;

however, for $A_t = 0.6$ the settings were 1/160 s, f/7.1 and 50. After an experiment, recorded images were cropped at the same location using a marker near the exit plenum so that the RT mixing layer spanned the entire width of the image, and then thereafter the photographs were processed with MATLAB©. The relationship between concentration and pixel intensity was determined by a calibration wedge (Andrews 1986; Snider & Andrews 1994; Banerjee & Andrews 2006), and the smoke intensity was found to be linear for a dynamic range over 100 pixel intensity values (Banerjee & Andrews 2006). For greyscale values less than 80 (lower means darker), the camera response became nonlinear so care was taken to ensure that the calibrated linear dynamic range from 100 to 200 was used during an experiment.

Notwithstanding the care described above, photographic images were found to be non-uniformly backlit. A gradual darkening at the edges was attributed to non-uniform light intensity of the fluorescent tubes, which were bright at the centre and darker towards the edges. To eliminate the effect of non-uniform background illumination, we use the Beers law method of Snider (1994). The corrected intensity, I_{corr}, is the intensity that would exist if the backlighting is uniform at $I_0^{uniform}$ and obtained from the measured intensity, I_m, and the measured background intensity, I_0 as

$$I_{corr} = \frac{I_0^{uniform}}{I_0} I_m. \tag{4.1}$$

4.2. *Hot-wire diagnostics*

We present an overview of the two different hot-wire techniques used in this work, namely an MPMO technique and an S3WCA technique, the purpose is to give insight into the methods and their relation to the flow physics; a detailed description about the related techniques and the calibration methods may be found elsewhere (Banerjee & Andrews 2007; Kraft *et al.* 2009).

4.2.1. *Multi-position multi-overheat technique*

The MPMO technique uses single normal (SN) hot-wire probes operated sequentially at different overheat ratios, and was adapted from similar techniques by Corrsin (1949) for low-velocity flows, and by Kovasznay (1950) and Rose (1973) for supersonic flows. The method has been modified in our variable density RT mixing layer to measure simultaneous density and velocity. Previous hot-wire measurements by Banerjee & Andrews (2006) at low $A_t \sim 0.035$ neglected the effect of helium on the hot-wire measurements, and used an MPSW technique (Bruun 1972) to decompose all three-dimensional velocity fluctuations. By not incorporating the effect of helium the MPSW technique was restricted to low-Atwood flows, i.e. $A_t < 0.04$. The current MPMO technique accounts for the effect of helium by employing a careful calibration in a binary air–helium mixture. Measurements were made using a hot-wire probe with a diameter of 5 μm (single wire: 55P16) coupled to a constant temperature anemometer (CTA) unit (Mini-CTA, Dantec Dynamics). The measurements were made at two overheat ratios of 1.6 and 1.9 that correspond to a $\Delta T (= T_{wire} - T_{amb})$ of 171.43°C and 257.14°C respectively. Details about the wire and anemometer properties at these overheat ratios can be found in table 3(*a*). Since the mean flow in our facility was one-dimensional $(U_m, 0, 0)$, with (x, y, z) as the axial (flow direction), vertical (y) and cross-stream (z) directions (see figure 4), with corresponding three-dimensional velocity fluctuations (u', v', w'). Table 3(*b*) gives the hot-wire angles used for the measurements, and the response function for a SN hot-wire probe, for small

Probe specific parameters		
Sensor resistance, $R_{20}(\Omega)$	3.38	
Sensor lead resist., $R_L(\Omega)$	0.9	
Support resistance, $R_s(\Omega)$	0.44	
Cable resistance, $R_c(\Omega)$	0.2	
Sensor TCR, $\alpha_{20}(/K)$	0.0036	
Wire operating parameters		
Overheat ratio ($= R_w/R_{amb}$)	1.9	1.6
$\Delta T = T_w - T_{amb}$(°C)	257.14	171.43
Operating resistance, $R_w(\Omega)$	6.51	5.47
Total resistance, $R_T(\Omega)$	7.99	6.98
Decade resistance, $R_D(\Omega)$	159.83	139.55
Bridge ratio, M	1 : 20	

TABLE 3*a*. Wire properties at overheat ratios 1.9 and 1.6.

Position	Φ	δ
1	90°	0°
2	60°	0°
3	30°	0°

TABLE 3*b*. Measurement orientations for the MPMO measurement technique. The measurement uncertainty of the positions is $\pm 2.5°$.

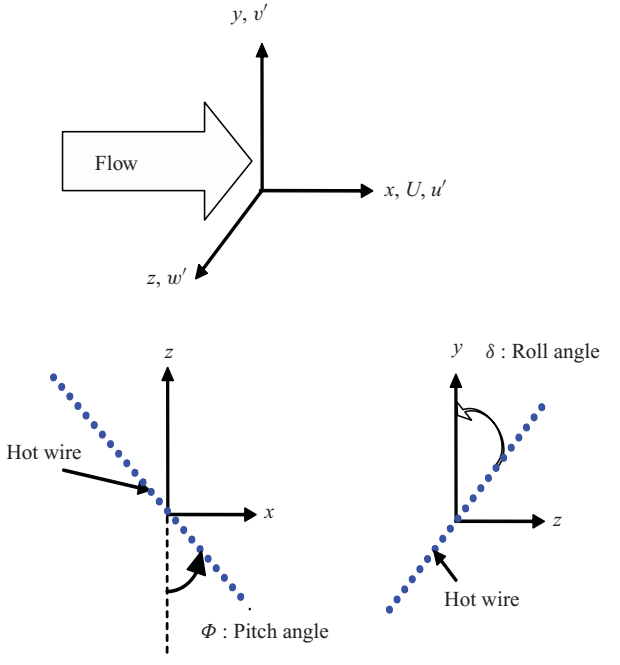

FIGURE 4. (Colour online) Wire orientations for the MPMO technique.

fluctuations in velocity and density, can be written as

$$\frac{e'}{\overline{E}} = \Delta e_u \frac{u'}{U_m} + \Delta e_v \frac{v'}{U_m} + \Delta e_w \frac{w'}{U_m} + \Delta e_\rho \frac{\rho'}{\overline{\rho}}, \tag{4.2}$$

where Δe_u, Δe_v and Δe_w are the velocity sensitivities, and Δe_ρ is the density sensitivity of an SN wire probe. Wire sensitivities are evaluated based on calibration of each wire, and defined as follows:

$$\left.\begin{aligned}
\Delta e_u &= \left.\frac{\partial \ln E}{\partial \ln U}\right|_{\theta,\Delta T_w,\rho} = \frac{U_m}{\overline{E}}\left.\frac{\mathrm{d}E}{\mathrm{d}U}\right|_{\theta,\Delta T_w,\rho},\\
\Delta e_v &= \left.\frac{\partial \ln E}{\partial \theta}\right|_{u,\Delta T_w,\rho} = \frac{1}{\overline{E}}\left.\frac{\mathrm{d}E}{\mathrm{d}\theta}\right|_{u,\Delta T_w,\rho},\\
\Delta e_w &= \left.\frac{\partial \ln E}{\partial \ln U}\right|_{\theta,\Delta T_w,\rho} = \frac{U_m}{\overline{E}}\left.\frac{\mathrm{d}E}{\mathrm{d}U}\right|_{\theta,\Delta T_w,\rho},\\
\Delta e_\rho &= \left.\frac{\partial \ln E}{\partial \rho}\right|_{u,\Delta T_w,\theta=90^\circ} = \frac{\overline{\rho}}{\overline{E}}\left.\frac{\mathrm{d}E}{\mathrm{d}\rho}\right|_{u,\Delta T_w,\theta=90^\circ}.
\end{aligned}\right\} \tag{4.3}$$

Squaring, and taking the time average of (4.2), gives ten independent terms on the right-hand side. Thus, in principle ten independent measurements are needed to evaluate all the variables. However, this was simplified by using known properties of our RT mixing layer (Ramaprabhu & Andrews 2004; Ristorcelli & Clark 2004; Banerjee & Andrews 2006). In particular, symmetry of the flow structures implies homogeneity of the fluctuations and so the horizontal fluctuation velocities $\overline{u'^2}$ and $\overline{w'^2}$ are taken equal based on earlier measurements done in our facility (Banerjee & Andrews 2006) which are in agreement with similar measurements done in the water channel facility (Ramaprabhu & Andrews 2004). Furthermore, symmetry also implies $\overline{\rho' u'}$ to be equal to $\overline{\rho' w'}$. Again, symmetry means that the cross terms in the Reynolds stress tensor are taken to be the same and negligible, i.e. $\overline{v'w'} \sim \overline{u'w'} \sim 0$. These symmetries are true for all Atwood numbers as well as for the compressible RT case. Thus, upon simplification we obtain

$$\begin{aligned}
\overline{\left(\frac{e'}{\overline{E}}\right)^2} = {} & \left(\frac{2\Delta e_u^2}{U_m^2}\right)\overline{u'u'} + \left(\frac{\Delta e_v^2}{U_m^2}\right)\overline{v'v'} + \left(\frac{\Delta e_\rho^2}{\overline{\rho}^2}\right)\overline{\rho'\rho'}\\
& + \left(\frac{2\Delta e_v \Delta e_\rho}{\overline{\rho} U_m}\right)\overline{\rho' v'} + \left(\frac{4\Delta e_u \Delta e_\rho}{\overline{\rho} U_m}\right)\overline{\rho' u'} + \left(\frac{2\Delta e_u \Delta e_v}{U_m^2}\right)\overline{u'v'}.
\end{aligned} \tag{4.4}$$

Equation (4.4) has six independent terms and thus six independent measurements are needed to obtain $\overline{u'u'}$, $\overline{v'v'}$, $\overline{\rho'\rho'}$, $\overline{\rho' v'}$, $\overline{\rho' u'}$ and $\overline{u'v'}$. By using a multi-position (see figure 4 and table 3*a*) and multi-overheats we obtained the necessary six independent traces (three positions and two overheats). Care was taken to ensure that the choice of overheat ratio of the wire and the orientations were independent. The hot wires were calibrated in a separate jet-flow calibration rig to evaluate the wire sensitivities defined in (4.3) prior to the actual experiments. Once the wires were transferred into the channel, it was placed in the air (top) stream and the voltage (signal) was matched with the calibration voltage. No drift was observed in transferring the wires between the calibration facility and the actual experiment. Figure 5(*a*,*b*) shows plots of wire sensitivities $\mathrm{d}E/\mathrm{d}U$ and $\mathrm{d}E/\mathrm{d}\rho$ at an overheat ratio of 1.6. More details about the calibration methods, techniques to evaluate wire sensitivities, and further details of the MPMO technique are given in Kraft *et al.* (2009) and Banerjee & Andrews (2007).

Limitations of MPMO. The present MPMO method is a 'time-averaged' technique and was intended to be robust enough to measure various statistics for a wide range of

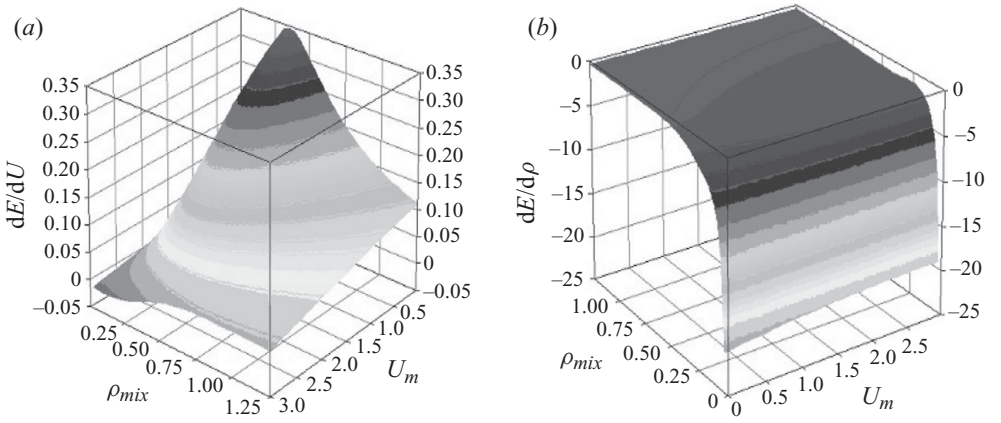

FIGURE 5. Wire sensitivities: $\mathrm{d}E/\mathrm{d}U$ (a) and $\mathrm{d}E/\mathrm{d}\rho$ (b) at an overheat ratio of 1.6 from the hot-wire calibration.

Atwood numbers for the flow. However, several limitations with the MPMO technique are described next for $A_t > 0.25$. In particular, the technique takes a constant value of $\mathrm{d}E/\mathrm{d}\rho$ for the entire experiment. In practice, this is accurate if the response of E versus ρ is linear, which is the case for a small density difference (up to $A_t < 0.25$) as can be seen in figure 5(b). However, for large density differences ($A_t > 0.25$), the response becomes significantly nonlinear as can be seen in figure 5(b). Thus, using a linear assumption (for calculating derivatives/sensitivities) would result in unacceptable errors in the measured quantities. So the MPMO method, though robust, is limited to low-Atwood measurements ($A_t \leqslant 0.25$), and also by virtue of being a 'time-averaged' method is not able to measure the fluctuation power spectrum.

4.2.2. *Simultaneous three-wire/cold-wire anemometry*

Simultaneous measurements using hot-wire (constant temperature) anemometer and cold-wire thermometer (constant current anemometers) have been used previously by Vukoslavcevic, Radulovic & Wallace (2005), Fabris (1983*a*) and Hishida & Nagano (1978), however, in these instances the additional complexity of varying fluid concentration/density was not present. Using temperature as a fluid marker for the density inside our gas RT mixing layer provides an opportunity to collect instantaneous and simultaneous measurement of velocity and density fluctuations. A three-wire probe, maintained at a $\Delta T (= T_{wire} - T_{amb})$ of 200°C is coupled with three-CTA circuits to obtain three-dimensional velocity fluctuations. To identify the gas concentration passing the probe, a temperature difference (∼5°C) between the two inlet streams is used as a marker for fluid concentration. This is valid as the Lewis number (ratio of mass diffusion to thermal diffusion) ∼1, which implies that as the two streams molecularly mix within the RT mixing layer, the temperature marker will transport and diffuse in the same manner as the gas it has marked.

For accurate measurement of the fluid concentration/density in the RT mixing layer, a temperature difference (ΔT) between the two inlet streams in the experiment must be selected. However, there are limitations with selecting an arbitrarily large temperature difference, as increasing the ΔT between the two inlet streams is detrimental to the hot-wire diagnostic, and also fluid densities can be significantly altered by a large ΔT. Table 4 illustrates the uncertainty that can be created by using a large temperature difference through its influence in the Atwood number for the RT mixing

A_t	ΔT(°C)	% change of A_t
0.01	5	45
0.10		6
0.50		3
0.75		1

TABLE 4. Effect of ΔT on the Atwood number.

layer. The Atwood numbers are determined using the temperature of the top and bottom (pure) streams. However, as the two fluids mix, both mass and temperature subsequently diffuse and the temperature of the resulting mix is different from their pure fluid temperatures. The local Atwood number calculated based on the pure fluid components of the mixture and that calculated based on the diffused temperature may be different if a large temperature difference is selected. For a small temperature increment of 5°C, it was found that the measurement uncertainty would be ~6 % for $A_t = 0.1$. Thus, when using small Atwood numbers (i.e. small concentrations of helium in air, and therefore small density differences) the role of the applied temperature difference between the inlet streams should be considered. For the current experiments at $A_t = 0.03$, the temperature difference between the two inlet streams was maintained at ~2°C, which resulted in ~9 % uncertainty in the Atwood number.

A cold-wire probe (5 μm diameter) coupled to a constant current anemometer circuit is used simultaneously to measure temperature fluctuations, and thereby identify concentration fluctuations of the mixture flowing over the probe. The cold wire has a lower frequency response of 1 kHz compared to hot wires, which have a frequency response of ~100 kHz. When used together for instantaneous density–velocity measurements the frequency response of the combined probe is limited by the frequency response of the cold-wire thermometer. The cold-wire and three-wire probes are placed side by side with a total probe resolution of ~6 mm. Information about fluid concentrations passing the cold-wire probe is compared with three-wire probe output voltages, and a calibration is performed at different concentrations, resulting in accurate measurements of the velocity fluctuations. The fluid concentration information obtained from the cold-wire probe is then converted to density fluctuations, thereby providing simultaneous and instantaneous measurements of temperature, density and velocity inside the RT mixing layer. For illustrative purposes, the order of steps in the conversion procedure and the interactions between hot-wire anemometers and cold-wire thermometers during various steps of the analysis are shown in figure 6. More details about the technique and calibration can be found in Kraft *et al.* (2009).

Limitations of S3WCA. Hot-wire anemometry is restricted to low- and moderate-turbulence intensity flows, typically less than 25 %, and thus care must be taken when using multiple hot wires in highly turbulent flows (Bruun 1995). This limitation is attributed to the insensitivity of hot wires to flow direction, ambiguity of the voltage signal when the velocity vector lies outside the approach cone, large probe volumes and the limited pitch/yaw response of the probes (Andreopoulos 1983; Frota & Moffat 1983; Bruun 1995). These issues may be avoided by limiting the instantaneous velocity vectors to approach angles (with the probe axis) of $\leqslant 20^\circ$ (Andreopoulos 1983; Frota & Moffat 1983). An application of this 20° limit approximates the instantaneous velocity vector in two dimensions using $2v'_{rms}$, as the vertical velocity component for the instantaneous velocity vector and the mean advective velocity,

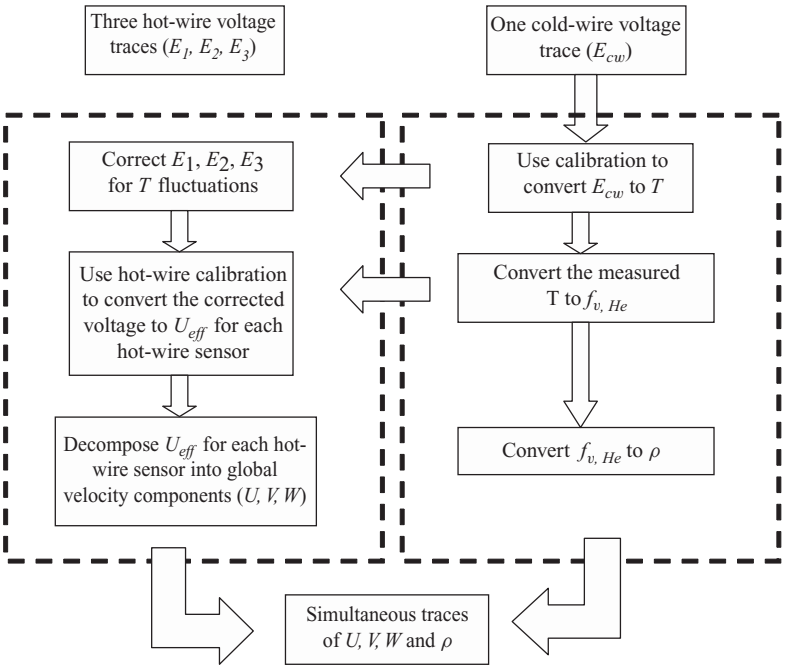

FIGURE 6. Flowchart for the determination of velocity and density inside the helium–air mixing layer simultaneously using a three wire hot-wire anemometer and a cold-wire thermometer.

U_m, as the horizontal component of the instantaneous vector. Twice the v'_{rms} is used so that the vector satisfies all vertical velocity fluctuations within a 95 % confidence interval. This approximation results in a turbulent intensity limit of 20 % for the dominant vertical velocities in our RT mixing layer, and a useful guide for design of future experiments. In addition, the spatial resolution of the cold-wire and three-wire hot-wire probes limits the frequency response of the combined system. Using a spatial resolution of 6 mm (probe diameter) and the advective velocity for the flow, the Nyquist limit implies a frequency response of approximately 50 Hz for the $A_t = 0.03$ experiments. However, as the flow channel velocity for the experiment is increased to reach higher A_t, the frequency response improves to $\sim$100 Hz at $A_t = 0.6$.

5. Results

We report flow visualization measurements of density profiles across the RT mixing layer at Atwood numbers of 0.04, 0.26, 0.47 and 0.6 that are statistically convergent. Hot-wire data were also taken at various downstream locations from the splitter plate for an Atwood number experiment of 0.04 and 0.6. Details about the various experiments can be found in table 5(*a*). The data presented cover RT mixing from $\tau = 0.56$–2.21, or corresponding 'α'-group (Dimonte *et al.* 2004) non-dimensional times $\tau_\alpha = 0.644$–9.791 (our range of non-dimensional times corresponds to a flow Reynolds number (Re_1) range of 150–25 000, which is calculated based on the definition given in (3.1)). Various velocity, density and density–velocity statistics were measured using hot-wire diagnostics and the results are presented below, with an error analysis. Representative values of basic velocity statistics along the centreline are provided in tables 5(*b*) and 5(*c*) for $A_t = 0.03$ and 0.6 measurements respectively.

Diagnostic	x-location (cm)	y-location (cm)	Atwood number
Imaging	5–185	−50 to 50	0.04, 0.097, 0.26 and 0.47
	5–130	−50 to 50	0.6
MPMO	50, 75, 100, 150 and 195	0	0.04 ($\Delta T \sim 2°$C)
	175	−36 to 36 cm (in 9 cm steps)	
S3WCA	100, 125, 150 and 175	0	0.03 ($\Delta T \sim 2°$C)
	40, 60 and 70	0	0.6 ($\Delta T \sim 5°$C)

TABLE 5*a*. Summary of imaging and hot-wire experiments reported. (Note: a y-location of 0 corresponds to the centreline of the RT mixing layer).

A_t	0.03			
x (m)	1.0	1.25	1.5	1.75
τ	0.76	0.95	1.14	1.33
U_m (m s^{-1})	0.65			
u'_{rms} (m s^{-1})	0.057	0.059	0.064	0.070
v'_{rms} (m s^{-1})	0.073	0.078	0.089	0.102
w'_{rms} (m s^{-1})	0.041	0.048	0.055	0.059
ρ'_{rms} (kg m^{-3})	0.023	0.022	0.021	0.020
$\overline{\rho' u'}$ (kg m^{-2} s^{-1})	−0.0002	−0.0004	−0.0002	−0.0002
$\overline{\rho' v'}$ (kg m^{-2} s^{-1})	−0.0013	−0.0014	−0.0014	−0.0016
$\overline{\rho' w'}$ (kg m^{-2} s^{-1})	0.0004	0.0003	0.0003	0.0002
θ	0.62	0.66	0.68	0.7
$R_{u'v'}$	0.312	0.133	0.220	0.216
$R_{v'w'}$	−0.277	−0.288	−0.167	−0.09
$R_{u'w'}$	0.203	−0.008	0.28	0.252
$R_{\rho'u'}$	−0.12	−0.03	−0.12	−0.14
$R_{\rho'v'}$	−0.76	−0.81	−0.74	−0.75
$R_{\rho'w'}$	0.38	0.31	0.30	0.21
S_u	−0.02	0.01	−0.08	0.05
S_v	0.27	0.02	−0.21	0.05
S_w	−0.24	−0.20	0.09	0.14
K_u	2.98	3.02	3.34	2.92
K_v	2.27	2.16	2.34	2.17
K_w	2.82	2.96	3.20	2.97

TABLE 5*b*. Velocity and density statistics at $A_t = 0.03$ based on the S3WCA hot-wire measurements.

5.1. *Flow visualization measurements*

Figure 7(*a*) shows a photograph of the formation and evolution of the buoyancy-driven mixing layer for an $A_t = 0.04$ experiment with green smoke introduced in the lighter air–helium stream. The minimum intensity corresponds to an air–helium mixture fraction of zero, and the maximum intensity corresponds to pure air with a mixture fraction of 1 (a negative of the images are taken so that the photographs for all

A_t	0.6		
x (m)	0.4	0.6	0.7
τ	0.44	0.66	0.78
U_m (m s^{-1})		2.0	
v'_{rms} (m s^{-1})	0.36	0.39	0.44
w'_{rms} (m s^{-1})	0.25	0.26	0.31
ρ'_{rms} (kg m^{-3})	0.27	0.25	0.24
$\overline{\rho' v'}$ (kg m^{-2} s^{-1})	−0.054	−0.071	−0.06
$\overline{\rho' w'}$ (kg m^{-2} s^{-1})	−0.003	0.01	−0.015
θ	0.54	0.46	0.6
$R_{v'w'}$	−0.251	−0.138	0.073
$R_{\rho' v'}$	−0.58	−0.68	−0.54
$R_{\rho' w'}$	−0.04	0.13	−0.18
S_v	−0.49	0.09	0.03
S_w	−0.26	−0.98	−0.43
K_v	3.15	3.14	3.27
K_w	4.40	4.39	4.62

TABLE 5*c*. Velocity and density statistics at $A_t = 0.6$ based on the S3WCA hot-wire measurements.

the experiments are consistent, i.e. black above and white below). To obtain a measured fluid mixture fraction $f_1 (= (\rho(x, y) - \rho_2)/(\rho_1 - \rho_2))$, peaks on the corresponding image histogram were determined with their corresponding intensities i.e. low ($\overline{I_{min}}$) and high ($\overline{I_{max}}$). The fluid mixture fraction was then obtained (having previously established a linear relationship of concentration to intensity using the calibration wedge) (Snider & Andrews 1994) from

$$f_1(x, y) = \frac{I(x, y) - \overline{I_{min}}}{\overline{I_{max}} - \overline{I_{min}}}. \tag{5.1}$$

A close inspection of the photographs reveals that large coherent structures in the light (air–helium) and dark (air–smoke) regions co-exist with finer scales of turbulent mixing. The buoyant mixing layer grows downstream as a front of rising and falling plumes (bubbles and spikes). During the experiment multiple plumes form spanwise and along the channel, and, as suggested in the photographs, plumes at the left of the photograph are formed by pairing with earlier plumes that came from the right. Such bubble competition (Emmons *et al.* 1960) is observed throughout the length of this RT mixing layer. Comparing photographs for an $A_t = 0.6$ experiment (figure 7*b*) with an $A_t = 0.04$ experiment (figure 7*a*), it is observed that well-defined distinct plumes (large scales) develop for $A_t = 0.04$ throughout the development of the RT-driven mixing layer. However, at $A_t = 0.6$, finer structures are observed in the mixing layer with a corresponding reduction of observed large-scale structures. Since both images have similar integral scales, the observations imply a larger range of length scales develop in the $A_t = 0.6$ experiment as the Reynolds number of the RT mixing layer increases from a value of 7500 for the $A_t = 0.04$ experiment to a value of 25 000 for the $A_t = 0.6$ case ($\tau = 1.986$ and 2.142 for the $A_t = 0.04$ and 0.6 experiments respectively).

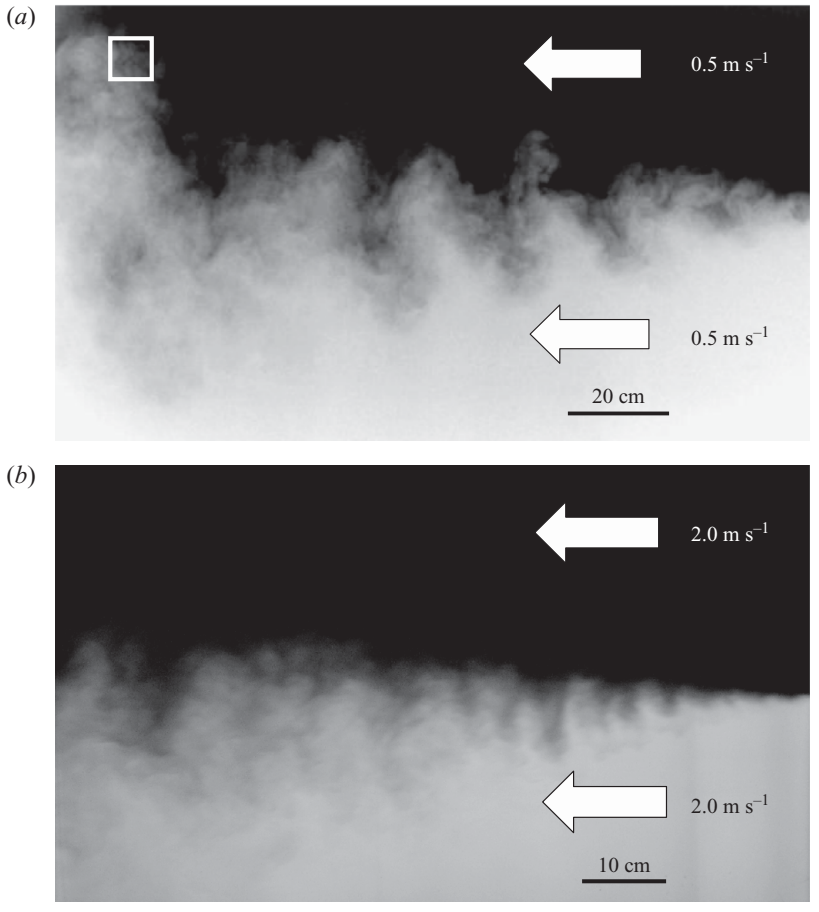

FIGURE 7. Photograph of the mixing layer at (*a*) $A_t = 0.04$ ($U_m = 0.5$ m s^{-1}), (with interrogation window for statistical analysis) and (*b*) at $A_t = 0.6$ ($U_m = 2.0$ m s^{-1}).

Figure 8 shows the measured average fluid mixture fraction variation across the RT mixing layer at axial locations of 0.75 m and 1.75 m (or equivalently, $\tau = 0.851$ and 1.986, and corresponding Reynolds numbers of 900 and 7500), taken from an $A_t = 0.04$ experiment. As observed in earlier experiments (Kucherenko *et al.* 1997; Snider & Andrews 1994; Dimonte & Schneider 2000; Ramaprabhu & Andrews 2004) and in numerical simulations (Youngs 1994; Cook & Dimotakis 2001), the measured mixture fraction profiles were found to vary linearly across the RT mixing layer, with slight rounding at the edges attributed to the shape of the plumes at the RT mix edge. Since $\overline{I_{min}}$ and $\overline{I_{max}}$ are based on the peaks of a corrected histogram, the mix fraction f_1 in figure 8 is not bound between 0 and 1, and noise can be seen outside the RT mixing region that corresponds to values above 1 and below 0 that were retained to indicate the error associated with the measurements. Figure 9 shows measured mix fraction profiles for $A_t = 0.26$ experiment. The mean stream velocity was increased to 1.2 m s^{-1} to maintain a parabolic flow (Snider 1994; Snider & Andrews 1994; Banerjee & Andrews 2006), and thus the spatial growth of the RT mixing layer appears similar to that observed during the $0.04 < A_t < 0.6$ experiments. Inspection of the mix fraction profiles at locations of 0.75 m and 1.75 m downstream from the splitter plate shows them to be slightly asymmetric, with $h_b \sim 32$ cm and $h_s \sim 40$ cm at a location 1.75 m from the splitter plate. Figure 10 plots the corresponding mixture

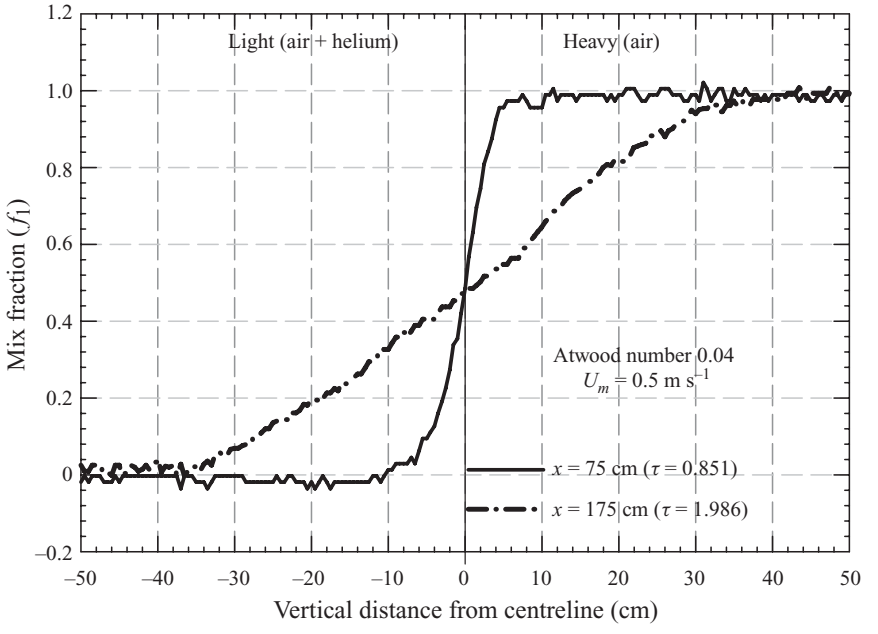

FIGURE 8. Mixture fraction profiles from the experiment at $A_t = 0.04$ ($U_m = 0.5$ m s^{-1}).

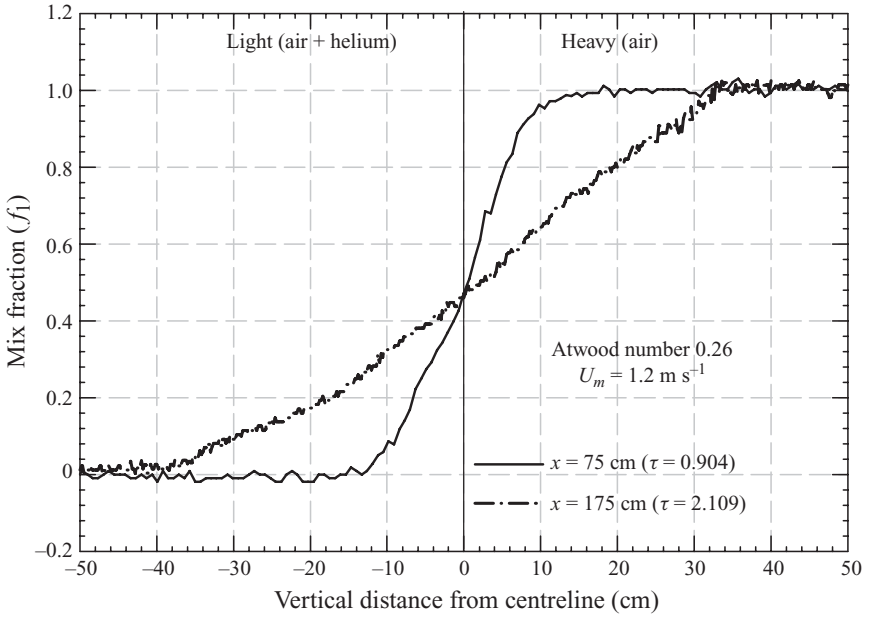

FIGURE 9. Mixture fraction profiles from the experiment at $A_t = 0.26$ ($U_m = 1.2$ m s^{-1}).

fraction profiles for an $A_t = 0.47$ ($U_m = 1.65$ m s^{-1}) experiment that quantitatively reveal the asymmetry in the RT mixing layer with $h_b \sim 30$ cm and $h_s \sim 45$ cm at a downstream location 1.75 m from the splitter plate. The photograph of the RT mixing layer for an $A_t = 0.6$ experiment ($U_m = 2.0$ m s^{-1}) in figure 7(*b*) even more clearly shows a strong penetration asymmetry between the spikes (falling dark plumes) and the bubbles (rising light-coloured plumes); with the falling spikes being narrower (and

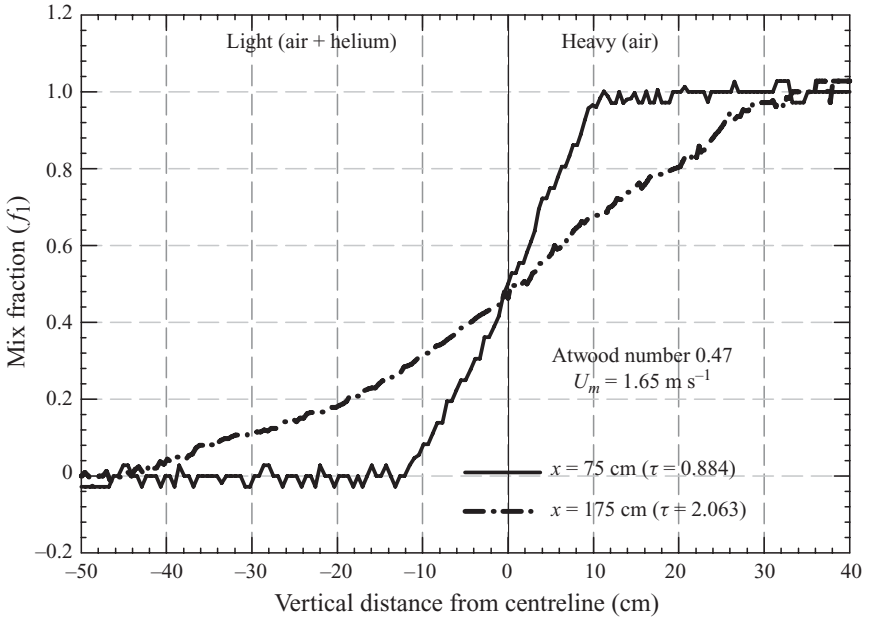

FIGURE 10. Mixture fraction profiles from the experiment at $A_t = 0.47$ ($U_m = 1.65$ m s^{-1}).

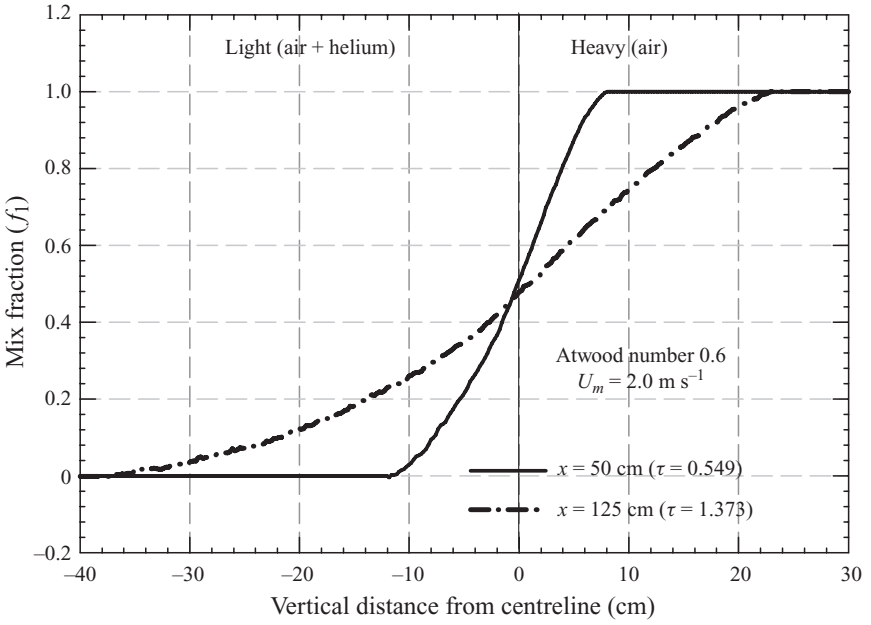

FIGURE 11. Mixture fraction profiles from the experiment at $A_t = 0.6$ ($U_m = 2.0$ m s^{-1}).

penetrating faster) than the rising bubbles. Figure 11 plots the corresponding mixture fraction profiles that quantitatively reveal the asymmetry in the RT mixing layer with $h_b \sim 22$ cm and $h_s \sim 33$ cm at a downstream location 1.25 m from the splitter plate. The mixture fraction profiles are smoother as total number of large independent structures averaged during the run for the $A_t = 0.6$ case is significantly larger than our previous runs. The mixture fraction profiles for $A_t \geqslant 0.47$ (figures 10 and 11)

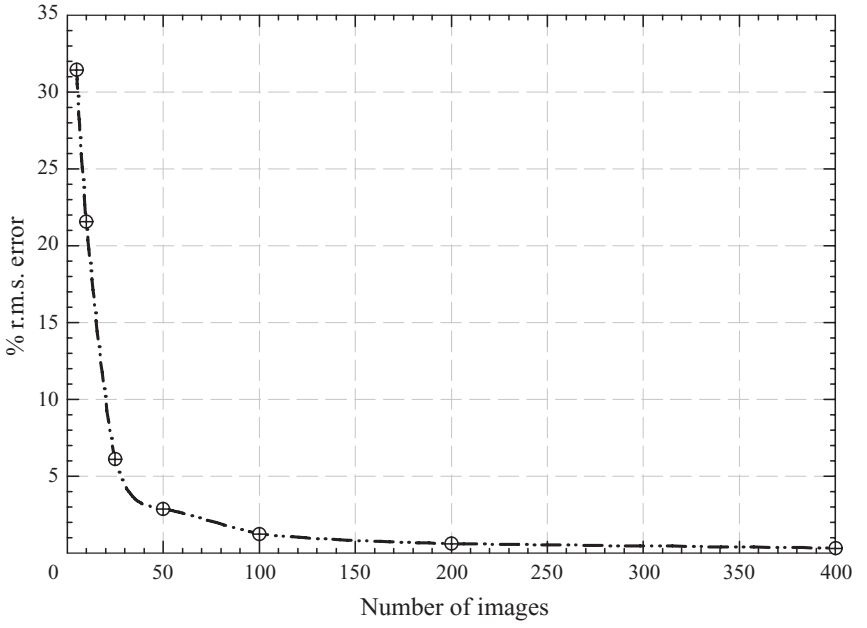

FIGURE 12. Percentage root mean square (r.m.s.) error of density measurements as a function of number of images.

also demonstrate that the position of the centreline of the RT mixing layer, i.e. the position that corresponds to a 50 % mix fraction, no longer corresponds to the initial position of the density interface. It was found that for $A_t = 0.6$, the deviation of the 50 % mix fraction from the original interface location was ~3 % of the total mixing layer width. Similar deviation is also observed in large $A_t (= 0.5$ and $0.9)$ simulations of Youngs (1989, 1991). For the profile shapes observed in experiment and numerical simulations, volume conservation requires the centreline value to drop as the asymmetry increases. Thus, the initial position of the density interface is not an invariant of the flow, and suggests an alternative definition for h_b and h_s based on the position of the 50 % mix fraction.

5.1.1. *Statistical convergence of measurements*

Before describing derived measurements from the data, we consider the statistical convergence of our measurements. A statistical convergence test was performed by finding errors in the measured value of the density variance. An interrogation window was taken downstream at $x = 1.75$ m and close to the edge of the RT mixing layer, as indicated in figure 7(*a*). Assuming that the errors in density measurements are purely random, Ramaprabhu & Andrews (2003) showed that the standard deviation of density (at the edge of the RT mixing layer) falls on a χ^2 distribution. From a series of samples, each of size N, we obtain the variance of density to be $\sigma_1^2, \sigma_2^2, \sigma_3^2, \ldots$, then σ_i^2 falls on a χ^2 distribution. If $n (= N - 1)$ is the number of degrees of freedom in each sample, then $n\overline{\sigma}^2/\sigma^2 = \chi_n^2$, where χ_n^2 is the χ^2 function based on n degrees of freedom. For a given value of n, we may determine the ratio $\overline{\sigma}^2/\sigma^2$ from the χ^2 distribution, and hence determine the error in determining the non-dimensional density variance. Thus, for a sample size N and a 95 % confidence level, the χ^2 distribution was evaluated in Banerjee & Andrews (2006) by giving an estimate of the error in determining density variance as shown in figure 12, and convergence was attained with ~100–150 images in the present experiment. In the current study,

images were captured at a rate of 80 images per minute and each image had ~2 (distinct) large structures, so that ~200 large structures (smaller structures being more numerous and hence not of concern) were averaged during the measurements, thus meeting the convergence requirements.

5.1.2. *Measurements of growth parameters* (α_b, α_s)

Next we review various techniques that have been used to obtain a measurement for the growth parameters α_s and α_b of (1.1), and show how they are intimately related.

In the far field (i.e. at late time), the ensemble averaged half mixing width h was shown by Snider & Andrews (1994) to grow quadratically with time according to (1.1), but did not go to zero at the start of the test section (end of splitter plate). This implies a virtual origin (VO) at the start of the splitter plate that accounts for boundary layer shedding from the splitter plate, and early time non-similarity development of the RT mixing layer. Snider & Andrews (1994) measured the growth parameter $\alpha_{b,VO}$ with an absolute deviation algorithm to define a virtual origin, x_0, by describing the half mix-width as

$$h_b = \alpha_{b,VO} A_t g \left[\frac{x - x_0}{U_m}\right]^2 = \alpha_{b,VO} A_t g [t - t_0]^2. \tag{5.2}$$

A straight line was fitted to the data and the slope of the straight line gave a value for the growth parameter $\alpha_{b,VO}$. In contrast, Banerjee & Andrews (2006) used the moving window (MW) technique of Leicht (1997) to determine a second-order polynomial best-fit line through the data. A window (50 pixels wide) was stepped downstream along the channel (1 pixel at a time) and was used to determine a second-order polynomial best-fit line through the data. The second derivative of the best-fit line was used to calculate $\alpha_{b,MW}$ as

$$\alpha_{b,MW} = \frac{\ddot{h}_b}{2A_t g}, \tag{5.3}$$

thus giving a local measure of the growth parameter as it develops along the length of the channel. Ristorcelli & Clark (2004) (RC), used a self-similar analysis for small-Atwood RT mixing to obtain an ordinary differential equation for the planar average of the mixing layer half-width h_b as

$$\alpha_{b,RC} = \frac{\dot{h}_b^2}{4A_t g h_b}. \tag{5.4}$$

As an exact mathematical result (5.4) validates the form of heuristically derived equations (Sharp 1984; Cook & Dimotakis 2001) that resulted from phenomenological buoyancy-drag type models. For constant $\alpha_{b,RC}$, A_t and g, the solution to (5.4) (taking only the positive root as physically realizable) can be written as

$$h_b = h_0 + 2\sqrt{\alpha_{b,RC} A_t g h_0}\, t + \alpha_{b,RC} A_t g t^2, \tag{5.5}$$

where h_0 is a virtual starting thickness, which effectively depends on how long it takes for the flow to become self-similar, which in turn depends on the spectrum of initial perturbations. Alternatively, if $t = 0$ is assigned to the point when the flow first achieves self-similarity, then h_0 corresponds to the thickness of the mixing region at that time. Interestingly, (5.2) when expanded gives a form similar to (5.5):

$$h_b = \alpha_{b,VO} A_t g (t - t_0)^2 = \left(\sqrt{\alpha_{b,VO} A_t g}\, t - h_0^{1/2}\right)^2, \quad \text{where} \quad h_0 = \alpha_{b,VO} A_t g t_0^2. \tag{5.6}$$

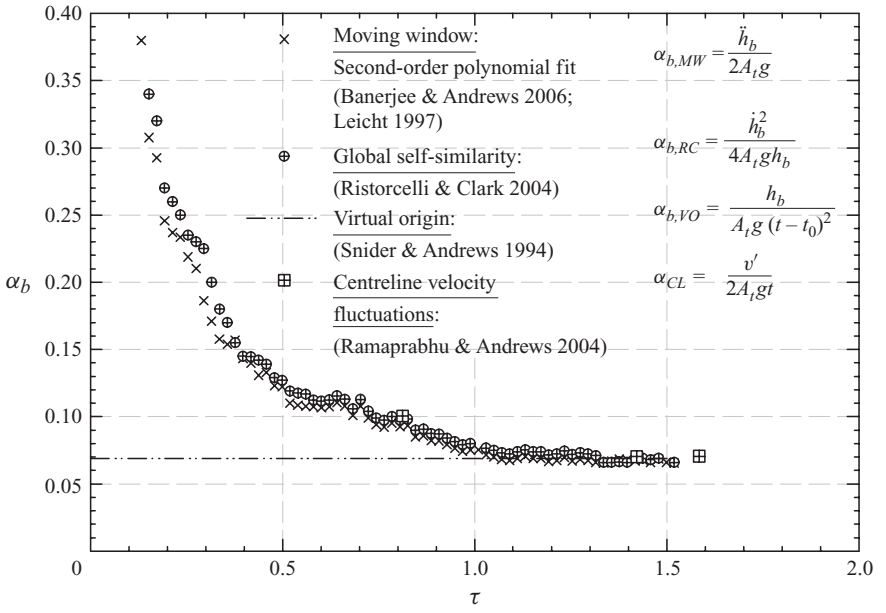

FIGURE 13. Comparisons of measured α_b from different definitions.

By comparing the terms in (5.5) and (5.6) and keeping in mind that $x_0 < 0$ (when accounting for the virtual origin), it is observed that

$$\alpha_{b,VO} = \alpha_{b,RC}. \tag{5.7}$$

A similar relationship may be found between $\alpha_{b,MW}$ and $\alpha_{b,RC}$ based on (5.3) and (5.4) by taking a time derivative of (5.4) gives

$$\alpha_{b,MW} = \alpha_{b,RC} + \dot{\alpha}_{b,RC}\frac{h_b}{\dot{h}_b}. \tag{5.8}$$

For an RT mixing layer, both h_b and $\dot{h}_b$ are positive and as shown in figure 13, $\dot{\alpha}_{RC}$ is negative, thus (5.8) suggests $\alpha_{b,MW} \leqslant \alpha_{b,RC}$, with the two values being nearly equal in figure 13 when the flow is self-similar, i.e. $\dot{\alpha}_{b,RC} \cong 0$ for $\tau > 1.25$.

An alternate method, used by Ramaprabhu & Andrews (2004), defines α based on the vertical r.m.s. velocity fluctuation, v'_{rms}, at the centreline (CL) and relates it to the mix-layer growth by

$$v'_{rms} = 2\alpha_{CL} A_t g t. \tag{5.9a}$$

Observations of the RT mixing layer shown in figure 7(a), where large-scale structures span the RT mixing layer and dominate the velocity fluctuations, suggest that expansion of the RT mix occurs due to large-scale velocity fluctuations that are seen across the whole RT mixing layer and not just the edge. Thus, the growth parameter α_{CL} may be related to the other values of α as

$$\alpha_{CL} = \frac{v'_{rms}}{2A_t g t} \approx \frac{\dot{h}_b}{2A_t g t}. \tag{5.9b}$$

On differentiating (5.5) and equating $\dot{h}_b$ with (5.9b), at late time the third term in (5.5) dominates and

$$\alpha_{CL} \approx \alpha_{b,RC}. \tag{5.9c}$$

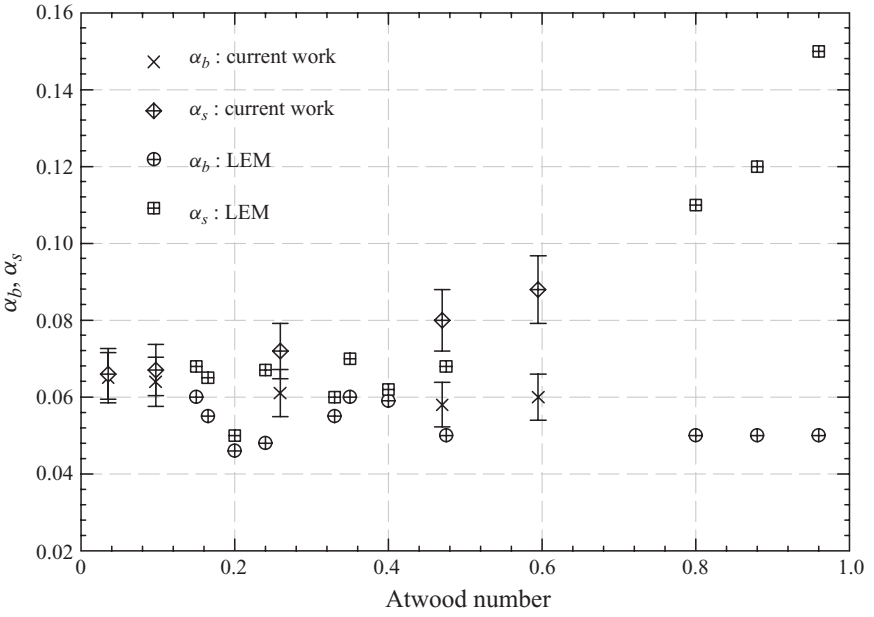

FIGURE 14. Comparisons of α_b and α_s with the LEM data of Dimonte & Schneider (1996).

Based on (5.7), (5.8) and (5.9*c*), we conclude that although the above definitions may give different values of the growth parameter at early times, once the flow becomes self-similar, they all give similar and closely related values of α. Figure 13 plots the values of α based on the above definitions and evaluated from measurements for an $A_t = 0.04$ in the present gas channel. It is observed that at late time ($\tau > 1.2$), when the flow has attained self-similarity, different definitions of α satisfyingly converge to $\alpha_{b,VO} = 0.069$, $\alpha_{b,MW} = 0.065$, $\alpha_{b,RC} = 0.068$ and $\alpha_{CL} = 0.067$. The results given in (5.2) through (5.8) are appropriate for small Atwood RT mixing ($A_t < 0.1$) when $\alpha_b \sim \alpha_s$. However, for large $A_t \geqslant 0.1$, the results are generally valid only for the bubble side.

Using the moving window definition of the growth parameter, the value of α_b was measured as 0.064 ± 0.005 for the current measurement in the range $0.04 \leqslant A_t \leqslant 0.6$. Similarly, the spike value of α_s was measured and it was found to increase with A_t number from a value of 0.065 at $A_t = 0.04$ to a value 0.088 at $A_t = 0.6$. These values of α_b and α_s obtained in the gas channel (plotted in figure 14) are comparable with the LEM experiments of Dimonte & Schneider (1996, 2000) who report an average value for α_b of 0.053 ± 0.006 when $A_t < 0.5$, and a value for α_b of 0.0496 ± 0.003 for $A_t > 0.8$. The present and LEM experiments consistently show an increase of α_s with an increase in Atwood number. However, our measurements of α_b and α_s are higher than the LEM results by approximately 18 % for the entire Atwood number range, with three possible explanations: the initial conditions for the experiments are not the same (a small variation of alpha with initial conditions is now expected); or, as Dimonte (2000, 2004) suggests, the difference may be due to the use of surfactants (LEM fluids were immiscible) which might yield different growth parameters; or perhaps the difference is due to lack of statistical convergence in the high-speed and technically challenging transient LEM experiments.

As mentioned, transient experiments (e.g. the LEM or Rocket Rig) as well as numerical simulations can lack statistical convergence, and it can be difficult to calculate growth rate parameters based on half-mix-width data using (5.3) and (5.4). To deal with this problem, an integral half mix-width for bubbles and spikes can be

	Based on half mix-widths $\alpha_{b,s} = \frac{\dot{h}_{b,s}^2}{4A_t g h_{b,s}}$		Based on integral half mix–widths $\alpha_{b,s,W} = \frac{\dot{W}_{b,s}^2}{4A_t g W_{b,s}}$	
Atwood number	α_b	α_s	$\alpha_{b,W}$	$\alpha_{s,W}$
0.04	0.068	0.068	0.066	0.068
0.097	0.065	0.067	0.065	0.069
0.259	0.064	0.071	0.061	0.074
0.47	0.063	0.081	0.058	0.082
0.6	0.060	0.088	0.056	0.091

TABLE 6. Growth parameters based on half mix-widths (h_b and h_s) and integral half mix-widths (W_b and W_s).

defined following Andrews & Spalding (1990):

$$W_b = 6\int_0^{H/2} f_1(1-f_1)\,\mathrm{d}y = \alpha_{b,W} A_t g t^2, \quad W_s = 6\int_{-H/2}^{0} f_1(1-f_1)\,\mathrm{d}y = \alpha_{s,W} A_t g t^2, \tag{5.10}$$

where f_1 is the plane-averaged volume fraction and the integral was taken over a domain that includes the mixing region. The factor of 6 derives from considering the width of a linear profile: indeed figures 8–11 show that mix profiles are linear except at the edges, where they are slightly rounded, and so W_b and W_s seem reasonable measures of half-integral mix-widths of bubbles and spikes respectively at small Atwood number. The growth parameters ($\alpha_{b,W}$ and $\alpha_{s,W}$) were then calculated by using W and $\dot{W}$ in the definition of 'RC' in (5.4). The results are tabulated in table 6 and show that the growth parameters calculated by using $\dot{h}_{b,s}$ and $\dot{W}_{b,s}$ give similar values for the current measurement range of $0.04 \leqslant A_t \leqslant 0.6$. Also, as shown in figure 15, if the time evolution of the growth parameters are compared, it is seen that $\alpha_{b,W}$ has less noise than α_b. Thus, an integral definition of mix-width may be used to avoid statistical convergence issues in numerical simulations and transient RT experiments. However, as a note of caution, interchanging mix-width measurements (h_b and h_s) by integral mix-widths (W_b and W_s) should be used carefully at high Atwood numbers ($A_t > 0.5$) as a problem occurs due to rounding of the volume fraction profiles at the edges that may lead to similar measures for W_b and W_s with $W_b/W_s \sim 1$; whereas h_b and h_s based on 5 % and 95 % edge detection may give $h_b/h_s < 1$, and thus W_b and W_s will give poor estimates of α if considered as a measure of bubble/spike penetration. This also implies that the asymmetry between the spike and bubble interpenetration will be reduced (at late time) if a ratio of integral mix-widths are taken (W_s/W_b) instead of mix-widths based on the 5 % and 95 % volume fraction values (h_s/h_b).

5.2. *Hot-wire measurements*

The two hot-wire diagnostics (MPMO and S3WCA) described in § 4.2 were used for measurements of various time-averaged and instantaneous statistics in the RT mixing layer at Atwood numbers of 0.04 and 0.6. The MPMO single-wire technique, based on evaluating the wire response function to variations in density, velocity and orientation, was used for measuring detailed time-averaged statistics inside the RT mixing layer at $A_t = 0.04$. However, limitations in the technique restricted its usage to $A_t \leqslant 0.25$. The S3WCA technique, based on the concept of temperature as a fluid marker, was more robust to provide instantaneous statistics for the large range of A_t

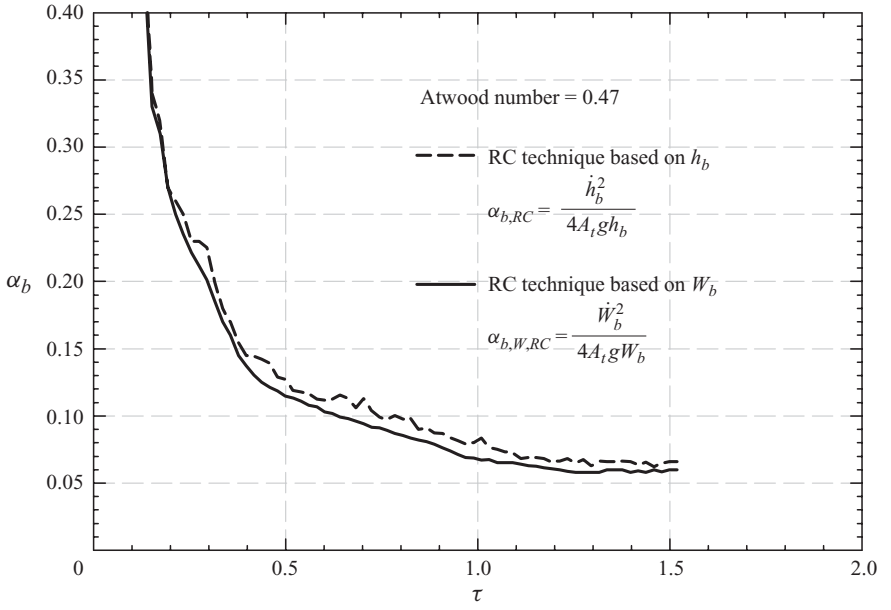

FIGURE 15. Measurements of α_b based on half mix-width (h_b) and integral half mix-width (W_b) obtained by using the Ristorcelli & Clark (2004) definition.

in our air–helium facility. The S3WCA diagnostics was first validated in the small density difference regime ($A_t \leqslant 0.04$), and the results were compared with the MPMO data and similar experiments done in a hot-water/cold-water water channel facility at $A_t \sim 7.5 \times 10^{-4}$. Upon validation in the low-Atwood-number regime, the S3WCA technique was used for large $A_t = 0.6$ experiments. In this section, we report detailed measurements and discuss the associated flow physics for both the low $A_t = 0.04$ experiment using MPMO and S3WCA techniques; and the high $A_t = 0.6$ experiment using the S3WCA technique.

5.2.1. *Detailed measurements in low-Atwood-number Rayleigh–Taylor experiments*

MPMO and S3WCA hot-wire measurements were made across the RT mixing layer, and at various downstream locations in the gas channel (see table 5*a*). The addition of helium to the RT mixing layer caused a small temperature gradient ($\sim 2^{\circ}$C) along the vertical (y) direction (i.e. from the air to the air–helium mixture). Variation in Atwood number due to this small temperature gradient is $\sim 4\,\%$ at an Atwood number of 0.04. We took advantage of this small temperature gradient and used a cold-wire probe (5 μm SN wire), coupled to a constant current anemometer (CCA) unit, to determine the location of the geometric centreline of the RT mixing layer (the reference point for our RT mix-width measurements). Since the Atwood number of 0.04 is small, the RT mixing layer is symmetric as seen in the mix fraction profiles (figure 8). At the start of an experiment, the cold wire was placed close to the centreline of the RT mixing layer and the data were logged. A centreline offset factor ϕ was computed after the logging process (Banerjee & Andrews 2006):

$$\phi = \left[1 + \frac{C_p^{bottom}}{C_p^{top}} \frac{\rho_{bottom}}{\rho_{top}} \left(\frac{T_{bottom} - T_i}{T_i - T_{top}}\right)\right]^{-1}, \tag{5.11}$$

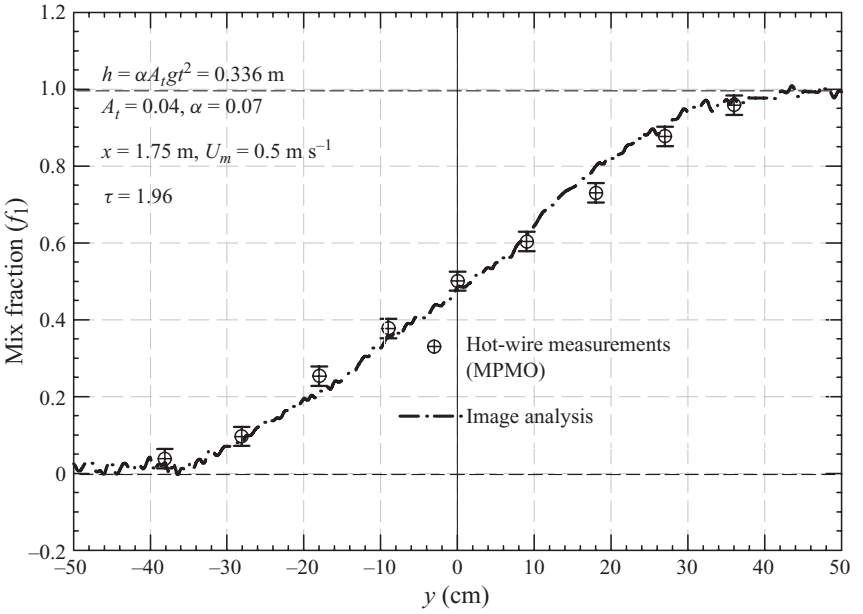

FIGURE 16. Comparison of density profiles measured with the MPMO technique and image analysis for an $A_t = 0.04$ experiment.

where C_p^{bottom} and T_{bottom} were the specific heat and temperature of the helium–air mixture (flow at the bottom section of the channel); C_p^{top} and T_{top} were the specific heat and temperature of air (flow at the top section of the channel); and T_i was the temperature of the mix. If $\phi \neq 0.5$, the position of the cold wire was readjusted and the data logging process repeated. The cold wire was adjusted until ϕ approached a value of 0.5 with an accuracy of $\pm 5\,\%$. Once the centreline was evaluated, a traverse was used, with fixed steps, so that the location of the data point relative to the centreline of the RT mixing layer was accurately known.

Measurements of molecular mix. We next report measurements for mean density, r.m.s. density fluctuations, and molecular mix taken in the gas channel at an Atwood number of 0.04 using the MPMO technique. Measured density fluctuation data of the RT mixing layer were used to obtain a local measure of the degree of molecular mixing θ, at different downstream centreline ($y = 0$) locations ($\tau = 0.56$–2.21), and at various locations across the RT mixing layer at $\tau = 1.986$ ($x = 1.75$m). The hot wire was moved vertically in intervals of $\sim$9 cm across the RT mixing layer. Figure 16 plots the measured mix-fraction f_1 across the RT mixing layer for an Atwood number experiment of 0.04. The measurements obtained with the MPMO technique compare well with mix-fraction profiles obtained from image analysis for the same Atwood number experiment (see figure 8). The profile shape also compares well with our previous results (Snider & Andrews 1994; Wilson & Andrews 2002; Ramaprabhu & Andrews 2004) and those of other experiments (Linden, Redondo & Caulfield 1992; Dalziel *et al.* 1999), as well as numerical simulations (Youngs 1984; Cook *et al.* 2004). As might be expected for a small Atwood number of 0.04, the RT mixing layer is symmetric about the centreline. Figure 17(*a*) shows the measured density fluctuation self-correlations B_2 and B_0 at $x = 1.75$ m ($\tau = 1.986$) downstream from the splitter plate. For these small-Atwood-number measurements, B_2 and B_0 show symmetry

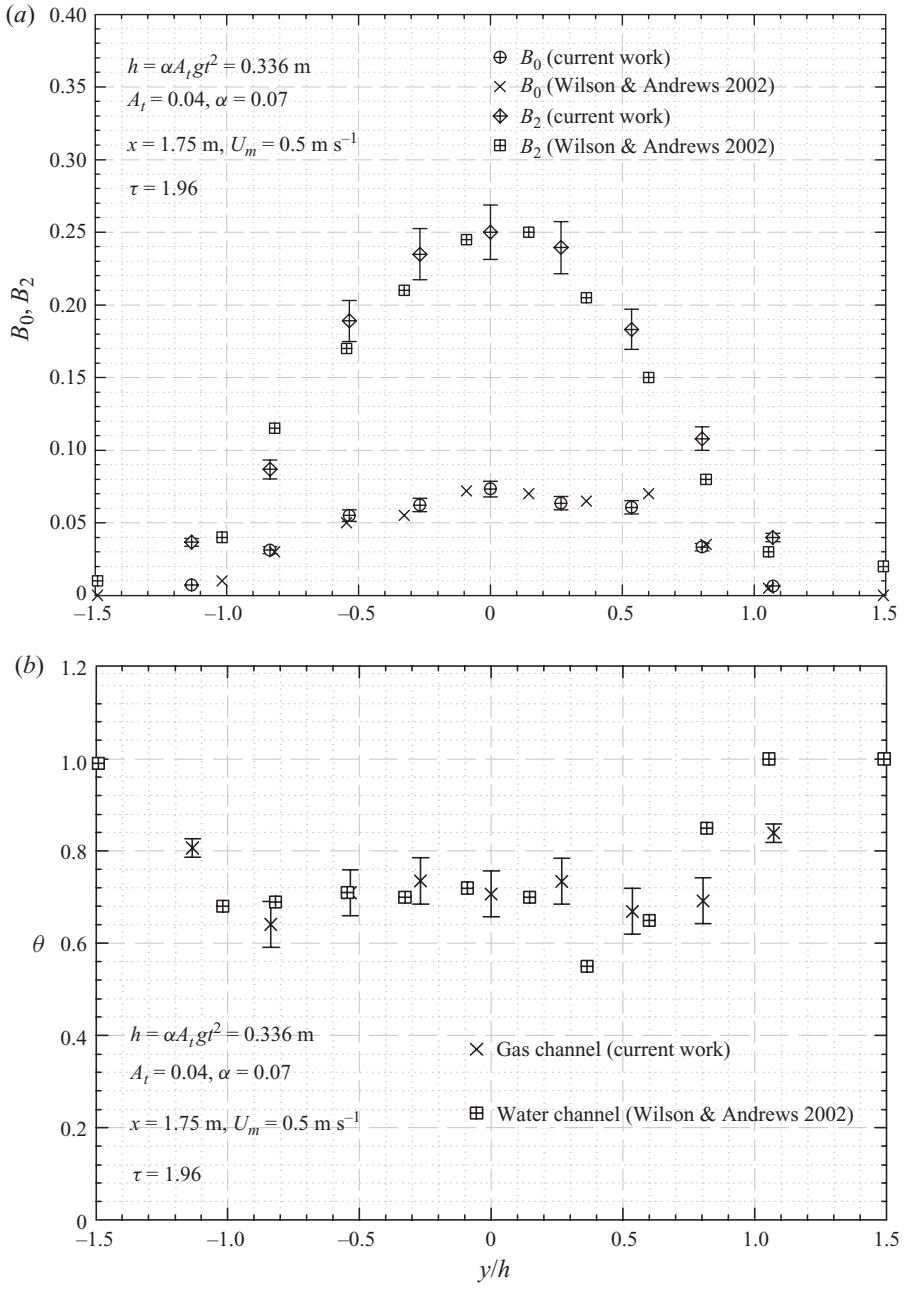

FIGURE 17. Comparison of molecular mix parameters (*a*) B_0, B_2, and (*b*) θ across the RT mixing layer at $\tau = 1.986$ ($A_t = 0.04$, $x = 1.75$ m from the splitter plate) with Wilson & Andrews (2002).

about the centreline at $y = 0$. Since at the centreline both fluids are present with equal probability, i.e. $f_1 = f_2 = 0.5$, the two-fluid density fluctuation self-correlation, B_2, takes a value of 0.25. However, B_2 quickly collapses to zero at the edges of the RT mixing layer, which implies the presence of a single fluid. The mix density fluctuation

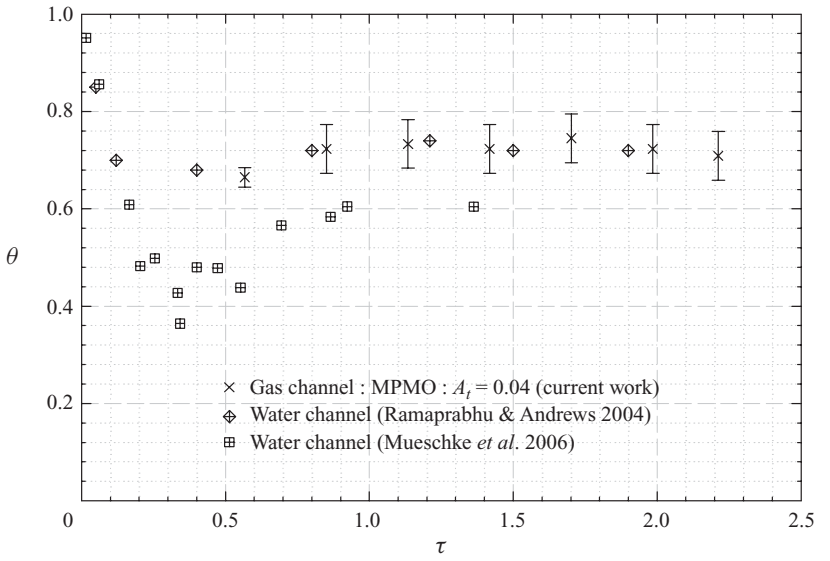

FIGURE 18. Comparison of the evolution of the molecular mix parameter θ measured at the centreline with Ramaprabhu & Andrews (2004) and Mueschke *et al.* (2006) as a function of non-dimensional time.

self-correlation, B_0, is about three times smaller at the centreline, and also collapses to zero at the edges. Figure 17(b) plots the molecular mix parameter θ across the RT mixing layer and inspection reveals that θ remains reasonably constant ($\sim$0.7) across this $Sc \sim 1$ RT mixing layer, in agreement with earlier results (Wilson & Andrews 2002; Ramaprabhu & Andrews 2004) from the small-Atwood-number water channel. However, beyond the edge of the RT mixing layer, where the probe sees only one fluid, the value of θ increases. These high values of θ outside the mixing region imply randomness and diffusion, which is due to noise in the density measurements because there is only one fluid outside the mixing region. Hence, these large values of θ outside the mixing layer ($y/h < -1$ and $y/h > 1$) should be ignored as the molecular mix parameter is not well defined in that region. Measured values for the molecular mix parameter θ in the gas channel ($Sc \sim 1$) are comparable with the water channel measurements of Ramaprabhu & Andrews (2004) ($Pr \sim 7$), and the brine/water experiments of Dalziel *et al.* (1999) ($Sc \sim 600$), who report a late-time value of $\theta \sim 0.6$–0.7.

The measured centreline time (downstream)-evolution of θ is shown in figure 18. Ramaprabhu & Andrews (2004) report measurements of θ that reach a value of 0.7 at late time when the flow becomes self-similar. Mueschke *et al.* (2006) report lower values of θ than Ramaprabhu & Andrews (2004) at the water channel facility, and attributed this to a difference in the size of their thermocouple probes and to the noise elimination techniques used in their work (Mueschke & Andrews 2006). Since our probe is also limited to scales about two times bigger than the Kolmogorov scale (see (5.13a)) we compare well with Ramaprabhu & Andrews (2004), but we would expect lower values for θ if the probe was smaller. Figure 18 reveals two stages of evolution for the molecular mixing fraction θ as the flow develops downstream, namely a decrease in θ for $\tau < 0.4$, followed by an increase for $\tau \geqslant 0.4$. For the first stage of the development period when $\tau < 0.4$, the value of θ decreases rapidly during the early time linear and weakly nonlinear growth of the initial perturbations,

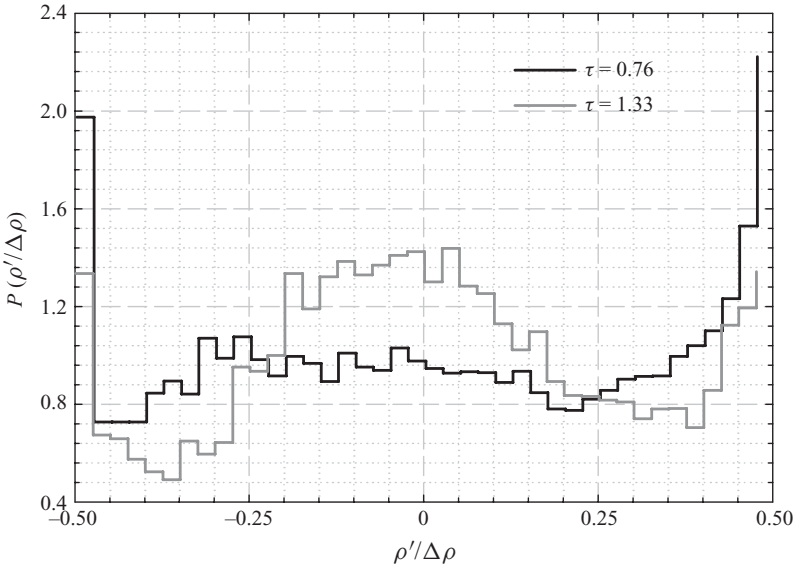

FIGURE 19. P.d.f. of density fluctuations at the centreline of the mixing layer using the SW3CA technique.

when there has been insufficient time for molecular diffusion to develop. In particular, this early time behaviour of θ is attributed to an increase in the fluctuation levels with the onset of instability, which in turn leads to a straining of the initial density interface shed from the splitter plate that sharpens the density gradient and lowers θ. Thus, at the centre plane the two fluids are 'stirred' with little molecular mixing for $\tau < 0.4$. The second late stage when $\tau \geqslant 0.4$ is characterized by an increase in θ and a transition to turbulent mixing. This is also demonstrated by inspecting the probability density function (p.d.f.) of the density fluctuations as shown in figure 19 which was obtained using the SW3CA technique at different downstream locations of $\tau = 0.76$ and $\tau = 1.33$. At early time, $\tau = 0.76$, the p.d.f. exhibits a bi-modal distribution with peaks that correspond to two pure fluids. However, at late time the probability of small density fluctuations (mixed fluid) increases, resulting in a broad peak in the centre of the distribution. This broad peak confirms an increased level of molecular mixing shown in figure 18 at late time.

A similar transition at $\tau \geqslant 0.4$ was observed by Wilson & Andrews (2002) in their related 'water channel' experiment. They ascribed development of θ during this second stage as due to flow complexity associated with the development of strong nonlinearities. In particular, secondary Kelvin–Helmholtz instabilities develop between rising bubbles and falling spikes, rapidly increasing the interfacial area between the fluids and thus associated molecular diffusion. Our flows were observed to act in the same fashion, and agree with this description. Ristorcelli & Clark (2004) also report a similar two-stage behaviour of θ; however, their simulations used a zero initial velocity field and perturbed the density field, whereas, in the present experiments, perturbations shed by the splitter plate are velocity fluctuations, which in turn induce density fluctuations (Ramaprabhu & Andrews 2004), and so a direct comparison cannot be made. Perhaps more usefully, the data for θ have been replotted in figure 20 as a function of the Reynolds number (Re_1) for the developing RT mixing layer. Inspection of figure 20 reveals that θ becomes self-similar (i.e. constant) at a Re_1 of $\sim$2000 for three data sets, i.e. the current work at low Atwood number $\sim$0.04,

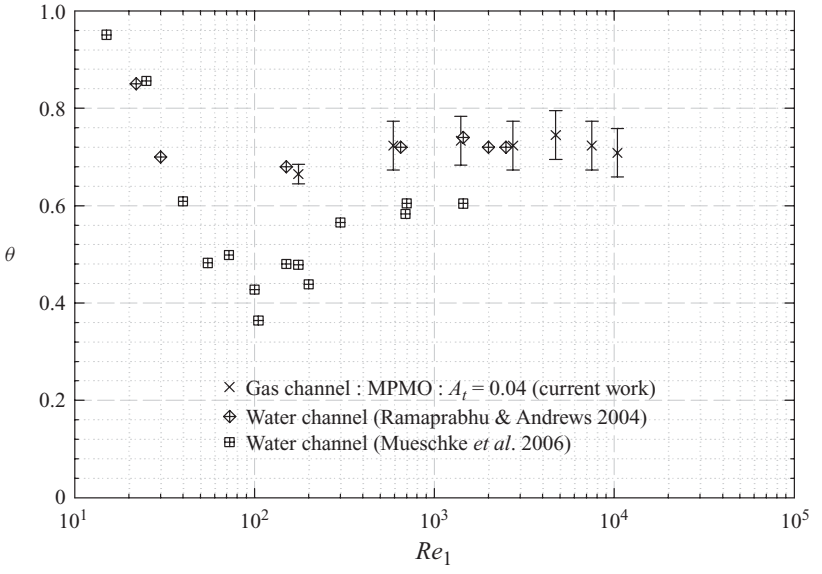

FIGURE 20. Comparison of the evolution of the molecular mix parameter θ measured at the centreline ($A_t = 0.04$) with Ramaprabhu & Andrews (2004) and Mueschke *et al.* (2006) as a function of (a) non-dimensional time τ.

and the hot/cold water channel measurements of Ramaprabhu & Andrews (2004) and Mueschke *et al.* (2006) that operated at small Atwood number $\sim 1.0 \times 10^{-3}$ and Prandtl number of 7. Moreover, the minimum value for θ (i.e. the end of the first stage of mixing) occurs at $Re \sim 100$. Thus, we identify a nonlinear mixing transition region (Dimotakis 2000) that runs from $100 < Re < 2000$, and leads from the development of single modes associated with a high-strain field, through mode coupling and continued development of long wavelength initial conditions, to a region with sufficient time and interfacial area between the gases that allows the development of self-similarity in the molecular mixing. Similar time variations of θ has been reported in recent large (3072^3) direct numerical simulations (Cabot & Cook 2006) of RT flows. We next compare θ with an alternate molecular mix parameter Ξ, defined to quantify molecular mixing for a fast reaction (Cook & Dimotakis 2001; Cook *et al.* 2004; Youngs 2003). The parameter Ξ measures the total product formed in the RT mixing layer relative to the product that would be formed if all the entrained fluid were completely mixed in each plane (assuming $f_1 = 0.5$ is stoichiometric). The value of Ξ is limited by the amount of lean reactant (light fluid) in the mixture (Cook & Dimotakis 2001) and is defined as (Youngs 2003)

$$\Xi = \frac{\int \overline{\min(f_1, f_2)}\, \mathrm{d}t}{\int \min(\overline{f}_1, \overline{f_2})\, \mathrm{d}t}. \tag{5.12}$$

The parameters Ξ and θ have been measured at various downstream centreline locations (see figure 21) as well as across the RT mixing layer for an Atwood number experiment of 0.04 (see figure 22). It is observed that both Ξ and θ are approximately equal, and this trend is also observed in numerical simulations (Cook *et al.* 2004; Youngs 2003).

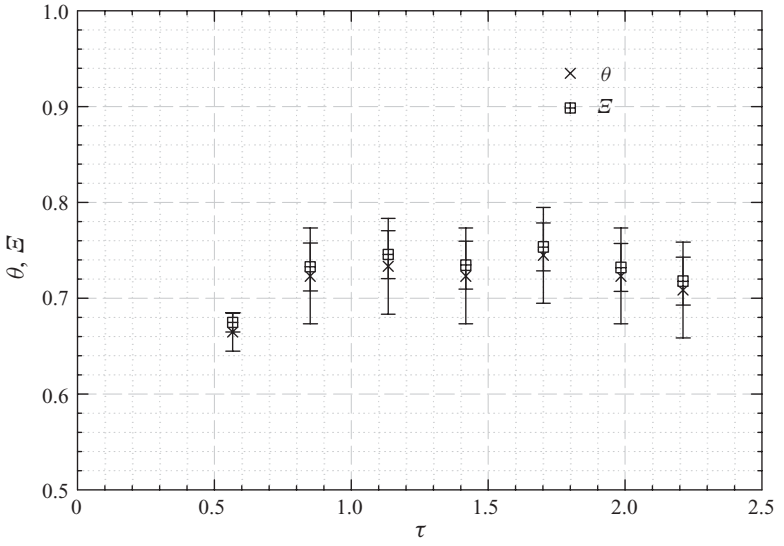

FIGURE 21. The evolution of mix parameters θ (for slow reaction) and Ξ (for fast reaction) measured at the centreline ($A_t = 0.04$).

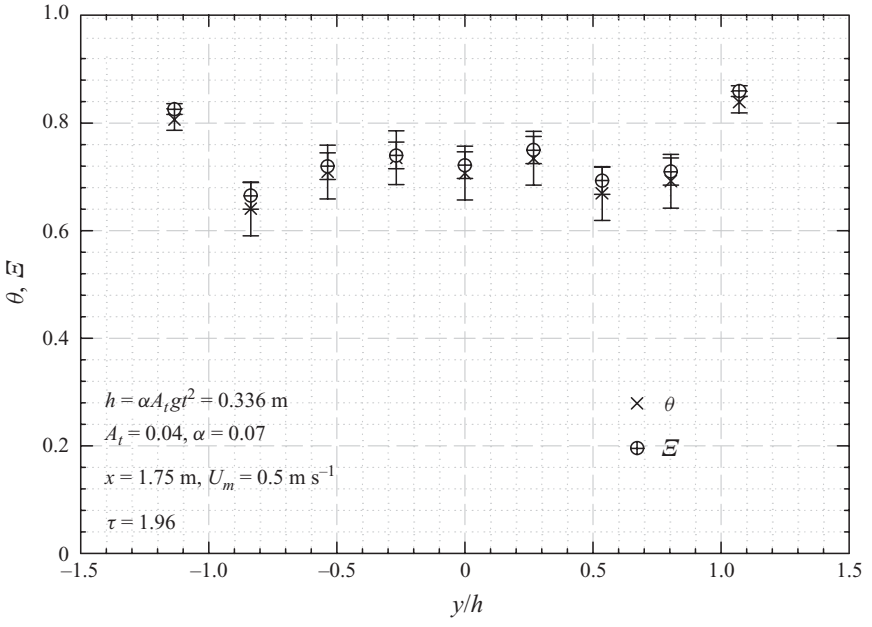

FIGURE 22. Comparison of molecular mix parameters θ (for slow reaction) and Ξ (for fast reaction) across the RT mixing layer at $\tau = 1.986$ ($A_t = 0.04$, $x = 1.75$ m from the splitter plate).

Turbulence length and time scales. Turbulent mixing may be viewed as a three-stage process of entrainment, dispersion and diffusion, spanning a full spectrum of length and time scales in the flow (Eckart 1948). For fluid entrained at the largest scales of the flow, scalar dispersion and mixing is hosted on the full spectrum of scales encountered in the turbulence cascade. Dimotakis (2005) noted that entrainment is driven by large-scale dynamics, dispersion by large- and intermediate-scale dynamics, and molecular mixing by the small (viscous/diffusive) scales. With this in mind, we review various inner scales of turbulence in our RT flow, with the outer scale being h_b or h_s.

The Kolmogorov scale, η_k, gives an estimate of the smallest eddies that are responsible for dissipation of energy (Pope 2000) and is represented for our experiment as

$$\eta_k \sim L Re_1^{-3/4}, \tag{5.13a}$$

where L is a measure of large-scale turbulence and was taken to be $(h_b + h_s)/2$. The definition (5.13*a*) holds true only when Re_1 (see (3.1)) is a Reynolds number based on the integral scale characteristic velocity ($\sqrt{gh}$) and the integral length scale ($2h = h_b + h_s$). In the present experiment, at $\tau = 1.986$ ($x = 1.75$ m) the $Re \sim 7500$, giving η_k as 0.048 cm. The Taylor microscale length scale, η_T, is given by Pope (2000):

$$\eta_T \sim \sqrt{10} L Re_1^{-1/2}, \tag{5.13b}$$

giving η_T as 1.168 cm (the Taylor–Reynolds number: $Re_T = \eta_T v'/\nu \sim 110$). The Taylor length scale defines the spatial scale across which local velocity values may be treated as approximately invariant (Pope 2000). The hot-wire probe used for the present measurements were 5 μm in diameter and 0.125 cm long. Since, the mean channel velocity was 50 cm s^{-1} for the $A_t = 0.04$ experiment, the maximum frequency component in the density fluctuations based on the mean velocity and η_k is $\omega_{max} = U_m/2\eta_k = 520$ Hz, where ω_{max} is the smallest frequency component of the density fluctuations that corresponds to a size of twice η_k. The spatial resolution of the hot wire allows for a maximum measurable frequency of $\omega_{max} = U_m/2l_{probe} = 200$ Hz. This implies that the probe has approximately half the necessary resolution to resolve the highest frequency component of the density fluctuations and cannot resolve the complete wavenumber range of the velocity and density (for simultaneous measurements) fluctuation power spectra. However, Wilson & Andrews (2002) examined the cumulative energy distribution of density fluctuations in RT mixing and their measurements show that only 1 % of the energy content is in the top 10 % of the largest wavenumbers of the spectrum. Thus, although we do not resolve to the Kolmogorov length scale η_k, we infer from the cumulative distribution plot (Wilson & Andrews 2002) that our hot wire measures over 90 % of the wavenumber range and thus represents over 99 % of the power spectrum associated with the density fluctuations.

For an energy cascade, a quantity of central importance is the rate at which energy is transferred from the large eddies to the smaller scales (Pope 2000). We thus review various turbulent time scales that are of relevance to our flow. The Kolmogorov time scale is calculated according to Pope (2000) as

$$\tau_k \sim \frac{h_b}{v'_{rms}} Re_1^{-1/2}, \tag{5.14}$$

where h_b is the half mix-width and v'_{rms} is the r.m.s. vertical velocity fluctuation, giving τ_k in the present experiment as 0.0217 s. The integral turbulent time scale is of the same order as the large-scale entrainment time scale and is calculated as

$$\tau_L \sim \frac{h_b}{v'_{rms}}. \tag{5.15}$$

The integral time scale for our RT mixing layer is ∼1.882 s. The time scale for scalar molecular mixing is of the same order as the Kolmogorov time scale and is calculated as

$$\tau_m \sim \frac{\eta_k^2}{\nu_{mix}} \sim \frac{h_b}{v'_{rms}} Re_1^{-1/2}, \tag{5.16}$$

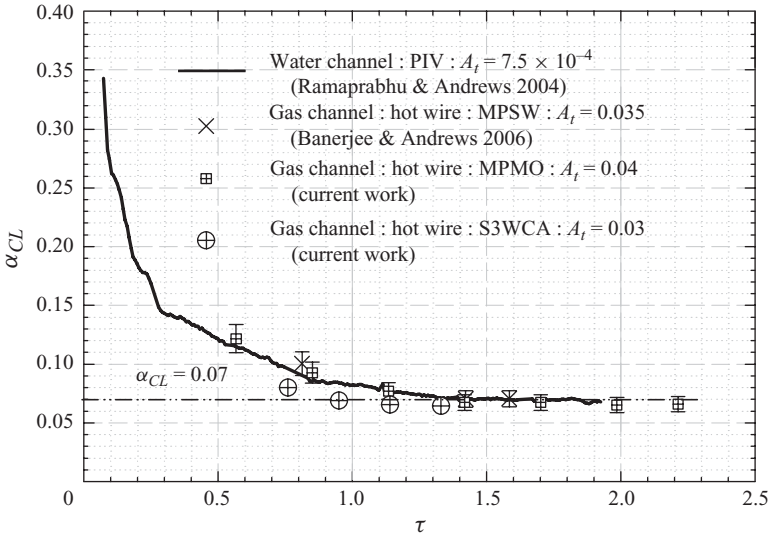

FIGURE 23. Comparison of measured α_{CL} by different techniques: MPMO, multi-position multi-overheat method (current work) at $A_t = 0.04$; S3WCA, combined three-wire and cold-wire method (current work) at $A_t = 0.03$; MPSW, multi-position method (Banerjee & Andrews 2006) at $A_t = 0.035$; and PIV, particle-image-velocimetry measurements done at the water channel (Ramaprabhu & Andrews 2004) at $A_t = 7.5 \times 10^{-4}$.

where η_k is the Kolmogorov length scale defined in (5.10), giving τ_m as 0.0217 s. For reference, we take the molecular mixing time scale to characterize the 'mixing rate' in our Rayleigh–Taylor flow. If the two fluids are immiscible, the molecular mixing time $\tau_m \to \infty$ and the scalar mixing-rate are considered to be 'slow'. The mixing rate is defined to be 'fast' when the molecular mixing time scale $\tau_m \to 0$ and is shorter than the Kolmogorov time scale, which occurs in cases where the two fluids are highly miscible ($Sc \ll 1$). Recent measurements by Mueschke *et al.* (2009) in a high-Schmidt-number ($\sim 10^3$) RT mixing layer have indicated that Schmidt number has a smaller effect on the degree of molecular mixing at higher Reynolds number. Based on the measured time scales for our air–helium experiment, the molecular mixing rate described here is considered as 'moderate'. This is also supported by our measure of the molecular mix parameter for both slow and fast reaction rates (θ and Ξ) that are almost identical values.

Measurements of velocity–velocity correlations. The centreline r.m.s. values of the vertical, v'_{rms}, horizontal, u'_{rms}, and spanwise, w'_{rms} velocities were measured using the MPMO technique (at seven downstream locations: $\tau = 0.567$, 0.851, 1.135, 1.418, 1.702, 1.986 and 2.213) and the S3WCA technique (four downstream locations: $\tau = 0.76$, 0.95, 1.14 and 1.33) in experiments with an Atwood number $\sim$0.03–0.04. As defined in (5.9*a*), a vertical r.m.s. velocity fluctuation, v'_{rms}, can be related to the RT mixing layer width by (Ramaprabhu & Andrews 2004):

$$v'_{rms} = \frac{\mathrm{d}h}{\mathrm{d}t} = 2\alpha_{CL} A_t g t = 2\alpha_{CL} A_t g \frac{x}{U_m}. \tag{5.17}$$

Figure 23 plots the measured growth parameter, α_{CL}, at these 11 downstream locations, compared with the MPSW hot-wire technique in the gas channel (Banerjee & Andrews 2006) at Atwood number 0.035, and a particle image velocimetry (PIV) measurement in the water channel at Atwood number 7.5×10^{-4} (Ramaprabhu & Andrews 2004). Figure 23 shows that all four sets of measurements are found to be consistent, and

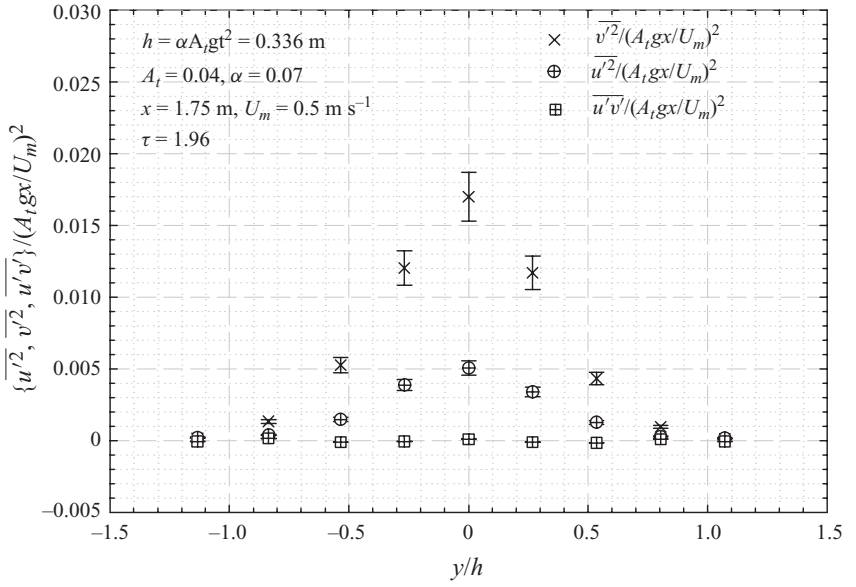

FIGURE 24. Velocity correlations across the RT mixing layer at $x = 1.75$ m ($\tau = 1.986$) for an $A_t = 0.04$ experiment. (Note: The error in these measurements of $\overline{u'v'}$ non-dimensionalized as shown is $\pm 2\,\%$).

α asymptotes to a value of 0.065–0.07 at late time so that the RT mixing layer grows quadratically far downstream from the splitter plate. For the low-Atwood-number experiments ($A_t = 0.03 \sim 0.04$ with the MPMO and S3WCA techniques), the RT mix is symmetric and hence $v'_b = v'_s = v'_{rms}$. However, for high-Atwood-number experiments ($A_t > 0.25$), the flow becomes asymmetric and a conditional sampling technique (described later in § 5.2.3) must be used to measure the bubble and spike vertical velocity fluctuations, v'_b and v'_s.

The MPMO measurements in figure 16 show that the two end points were outside the RT mixing layer and have been neglected in what follows. Figure 24 plots non-dimensional velocity correlations: $\overline{v'^2}$, $\overline{u'^2}$ and $\overline{u'v'}$ across the RT mixing layer. The velocity correlations were non-dimensionalized by using a 'free-fall' velocity scale of $A_t g x/U_m$. In this no shear experiment, gravity drives the vertical velocity fluctuations, generating the characteristic 'mushroom' shape of a Rayleigh–Taylor instability, and so $\overline{v'^2}$ dominates over $\overline{u'^2}$ everywhere across the RT mixing layer. In buoyancy-driven mixing, there is no source to correlate the two components of velocity, as in shear-driven flows, thus the measured cross-correlation $\overline{u'v'}$ shown in figure 24 was found to be negligible across the RT mixing layer. The lack of a cross-correlation between the two components of velocity may also be explained graphically by the RT mushroom-shaped structures that have left–right symmetry about the centre (see figure 25). The ratio v'_{rms}/u'_{rms} across the RT mixing layer is plotted in figure 26, and is approximately constant across the RT mixing layer at ~ 1.8, suggesting an existing equilibrium between the u'_{rms} and the v'_{rms} kinetic energy production terms everywhere in the RT mixing layer. This also implies that mushroom-shaped structures are convected up and down the RT mixing layer with little change in shape. Ristorcelli & Clark (2004) suggest that large-scale anisotropy between $\overline{u'^2}$ and $\overline{v'^2}$ can be characterized through the normalized anisotropy tensor, b_{ij}, defined as (Pope 2000)

$$b_{ij} = \frac{\overline{u_i u_j}}{\overline{u_k u_k}} - \frac{\delta_{ij}}{3}. \tag{5.18}$$

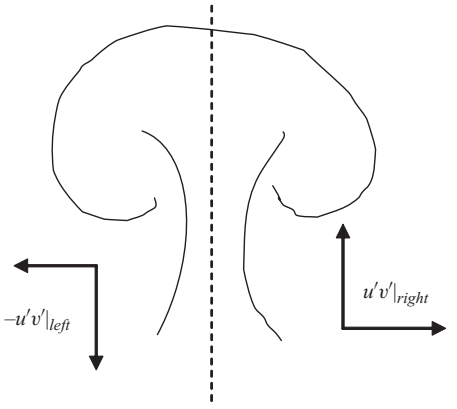

FIGURE 25. Illustration of the left–right symmetry about the centre of a mushroom-shaped structure so that $u'v'|_{right} = -u'v'|_{left}$.

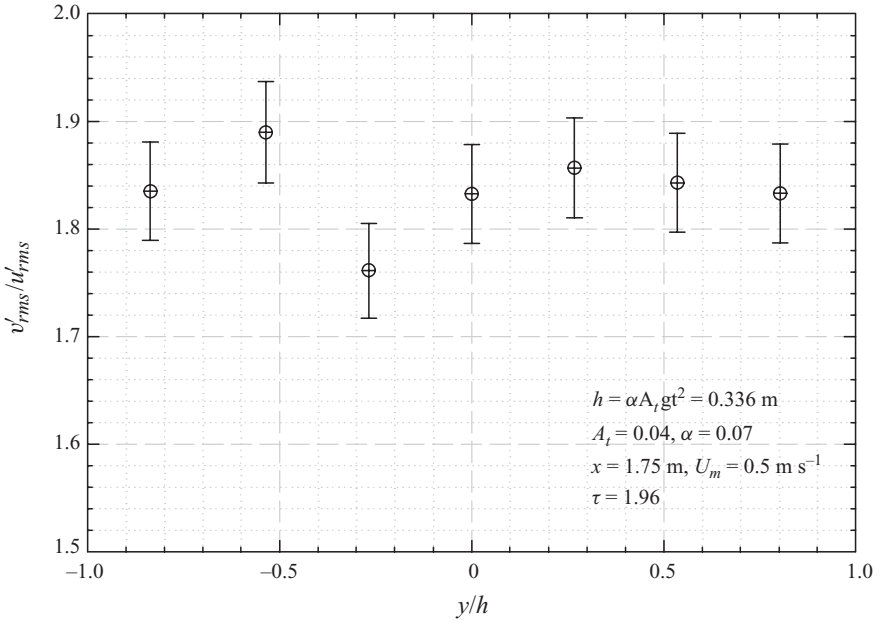

FIGURE 26. Ratio of v'_{rms}/u'_{rms} across the RT mixing layer at $x = 1.75$ m ($\tau = 1.986$) for an experiment at $A_t = 0.04$. The data points at $y/h = \pm 1.15h$ are omitted as $v'_{rms} \sim 0$ outside the RT mixing layer.

Equation (5.16) reduces to the following form for RT:

$$b = \begin{pmatrix} b_{uu} & b_{uv} & b_{uw} \\ b_{vu} & b_{vv} & b_{vw} \\ b_{wu} & b_{wv} & b_{ww} \end{pmatrix} = \begin{pmatrix} \dfrac{\overline{u'u'}}{2k} - \dfrac{1}{3} & 0 & 0 \\ 0 & \dfrac{\overline{v'v'}}{2k} - \dfrac{1}{3} & 0 \\ 0 & 0 & \dfrac{\overline{w'w'}}{2k} - \dfrac{1}{3} \end{pmatrix}, \tag{5.19}$$

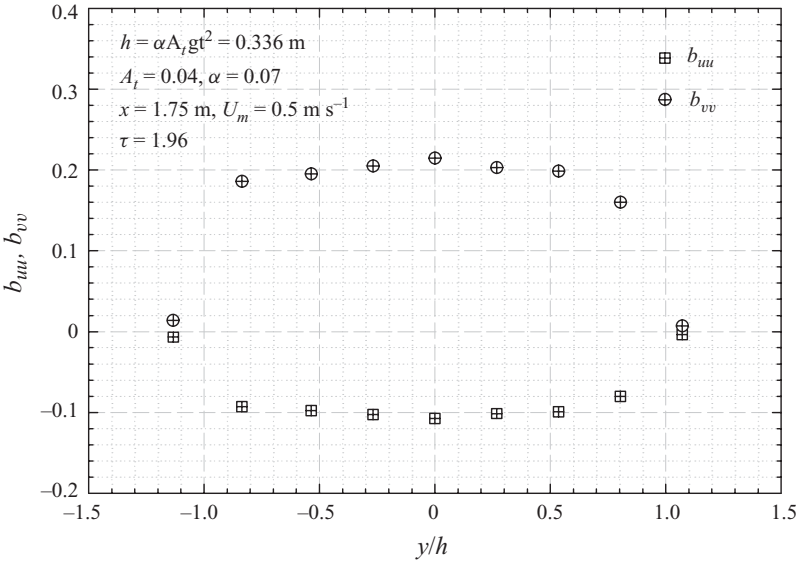

FIGURE 27. Profiles of the anisotropic tensor (b_{uu} & b_{vv}) across the RT mixing layer at $x = 1.75$ m ($\tau = 1.986$) for an experiment at $A_t = 0.04$.

where k ($= \overline{u_k u_k}/2$) is the turbulent kinetic energy, and b is the deviatoric part of the Reynolds stress tensor normalized by the kinetic energy term. For isotropic turbulence, $b_{uu} = b_{vv} = b_{ww} = 0$, and thus $b = 0$. More generally, $-1/3 \leqslant b_{ij} \leqslant 2/3$, where the upper and lower limits represent one-dimensional and two-dimensional distributions of the turbulent kinetic energy respectively (Ristorcelli & Clark 2004). Thus, b_{ij} characterizes the geometry of turbulence and is independent of the amplitude of the fluctuations. Figure 27 plots the anisotropy tensor across the RT mixing layer at a downstream location of $x = 1.75$ m ($\tau = 1.986$) from the splitter plate. As expected, most of the turbulent transport appears in the vertical direction. It also appears that $b_{\alpha\alpha} \rightarrow 0$ near the edges of the RT mixing layer suggesting isotropy. The velocity fluctuation statistics are reasonably constant across the RT mixing layer, and this is consistent with the observations of Ramaprabhu & Andrews (2004).

Anisotropy and dominance of the vertical velocity fluctuations, v'_{rms}, can also be observed in the p.d.f.s of the measured centreline velocity fluctuations of the mixing layer, as shown in figure 28. The vertical velocity fluctuations, v', exhibit a flat p.d.f. due to a broad spectrum of scales that develop from the rising bubbles and falling spikes within the mixing layer. However, both streamwise and cross-stream velocity fluctuations, u' and w', exhibit approximately Gaussian behaviour, as small velocity fluctuations dominate and were more likely to be present. Quantitatively, the flatness of these p.d.f.s can be compared using the kurtosis for the velocity fluctuations as $K_u = \overline{u'^4}/(\overline{u'^2})^2$, $K_v = \overline{v'^4}/(\overline{v'^2})^2$, $K_w = \overline{w'^4}/(\overline{w'^2})^2$. For a Gaussian distribution the kurtosis is 3; as kurtosis decreases the distribution flattens. For the measured velocity fluctuations at $\tau = 1.33$, a kurtosis of 2.9, 3.0 and 2.2 was found for u', w' and v', respectively. This compares well with the measured kurtosis for the centreline vertical velocity fluctuations in the water channel facility (Ramaprabhu & Andrews 2004) who measured values of $K_v = 2.3$ at $\tau = 1.21$. The low value of K_v (< 3.0) implies that rather than having short, intermittent bursts of v' and related turbulence, the vertical velocity fluctuations and turbulent structure of the rising bubbles and

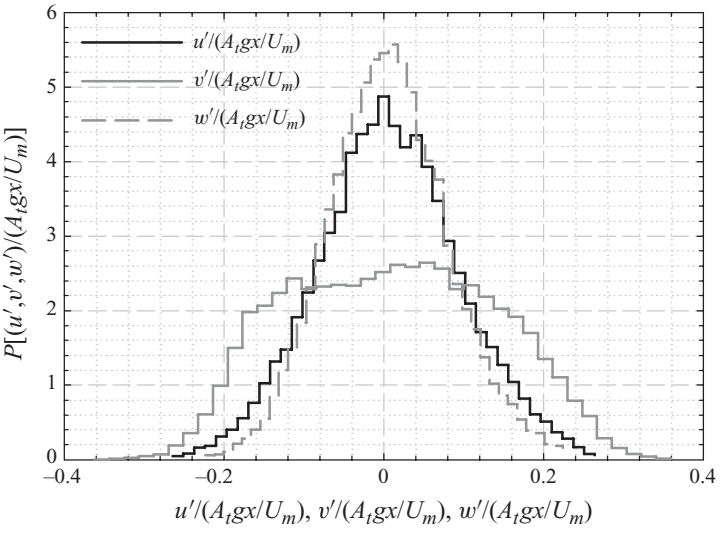

FIGURE 28. P.d.f. of the measured centreline velocity fluctuations using the S3WCA technique at the centreline of the mixing layer for $A_t = 0.03$ and $\tau = 1.33$.

falling spikes generates a broad spectrum of scales. Dominance of vertical velocity fluctuations is consistent across the mixing layer (Ramaprabhu & Andrews 2004). The third moment of the velocity field represents the skewness of the velocity p.d.f.s as $S_u = \overline{u'^3}/(\overline{u'^2})^{3/2}$, $S_v = \overline{v'^3}/(\overline{v'^2})^{3/2}$, $S_w = \overline{w'^3}/(\overline{w'^2})^{3/2}$. The measured values of S_u, S_v and $S_w \sim 0$ at the centreline. However, the distribution of the measured vertical velocity fluctuations does change the behaviour away from the mixing layer centreline as indicated by the skewness. Measured p.d.f.s of the vertical velocity fluctuations at $\tau = 1.33$ are shown in figure 29 at the mixing layer centreline ($\overline{f}_{v,1} = 0.51$, $S_v = 0.05$), and in the top half of the mixing layer with average volume fractions of $\overline{f}_{v,1} = 0.65$ ($S_v = 0.43$) and $\overline{f}_{v,1} = 0.77$ ($S_v = 0.90$). As the volume fraction of $\overline{f}_{v,1}$ increases (moving into the top half of the mixing layer) more heavy fluid is present, and negative velocity fluctuations become more likely as heavy fluid entrained at the edge of the mixing layer is transported down through the mixing layer. This results in the observed asymmetry in the measured vertical velocity fluctuation p.d.f. In addition, the intensity of the turbulence in the mixing layer decreases towards the edges of the mixing layer, resulting in a narrower range (smaller variance) of measured vertical velocity fluctuations.

Measurements of velocity–density correlations. Figure 30 shows the evolution of measured centreline values obtained from the hot-wire techniques for the mass flux term $\overline{\rho' v'}$, which serves as the primary turbulent mass transport term in our RT mixing layer. The correlation has been normalized by the product of the density difference, $\Delta\rho$, and $A_t g x/U_m$ (the free-fall velocity). The figure shows that the normalized mass flux term $\overline{\rho' v'}/(\Delta\rho A_t g\, x/U)$ reaches a constant value when the flow becomes self-similar at approximately a value of $\tau = 1.5$. Ristorcelli & Clark (2004) show similar behaviour in their normalized mass flux term (normalized by $h^{1/2}$) as the flow attains self-similarity. The molecular mix parameter, θ, reaches self-similarity at a value of $\tau = 0.9$ as shown in figure 18. It is perhaps not surprising that θ attains self-similarity before the mass flux, as density fluctuations (ρ') drive velocity fluctuations (v') in our 'moderately' fast experiment, and so must settle first. Figure 31 shows the

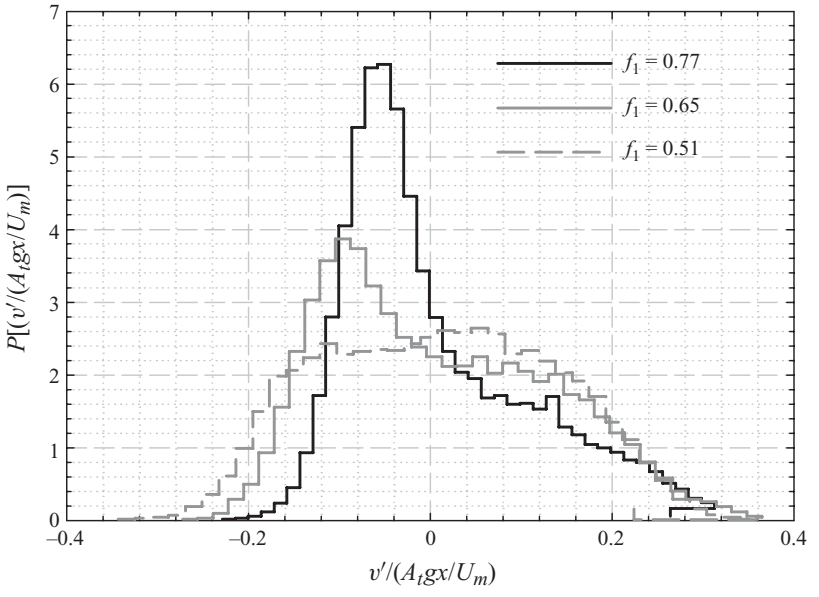

FIGURE 29. P.d.f. of the vertical velocity fluctuations using the S3WCA technique for $A_t = 0.03$ at $\tau = 1.33$ across the mixing layer with average volume fractions of fluid 1, $\overline{f}_{v,1} = 0.77$, 0.65, and 0.51. The properties of the these distributions are determined for $\overline{f}_{v,1} = 0.51$ where $\overline{v'^2} = 0.010$, $K_v = 2.17$, $S_v = \overline{v'^3}/(\sqrt{\overline{v'^2}})^3 = 0.05$; $\overline{f}_{v,1} = 0.65$ where $\overline{v'^2} = 0.0096$, $K_v = 2.3$, $S_v = 0.43$; and $\overline{f}_{v,1} = 0.77$ where $v'^2 = 0.0067$, $K_v = 3.1$, $S_v = 0.90$.

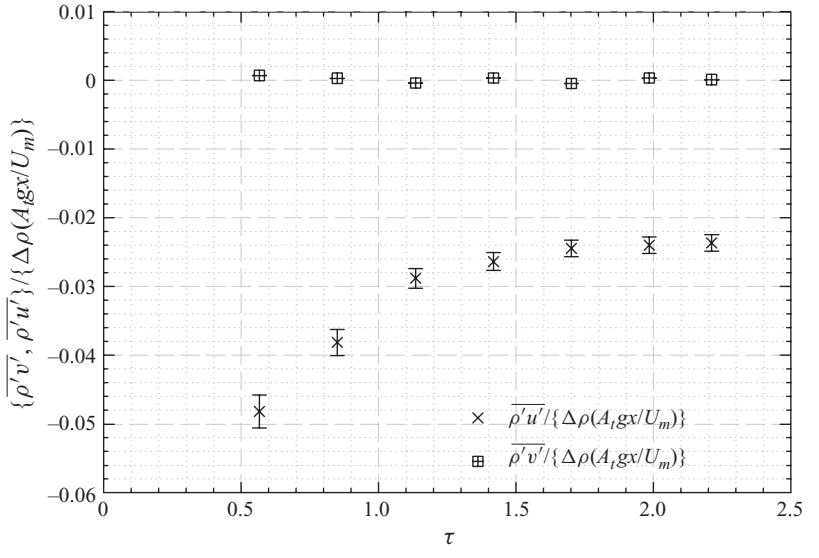

FIGURE 30. Evolution of non-dimensional $\overline{\rho' v'}$ (primary transport term) and $\overline{\rho' u'}$ for $A_t = 0.04$.

non-dimensional values of $\overline{\rho' v'}$ and $\overline{\rho' u'}$ across the RT mixing layer at $\tau = 1.986$. It is seen that $\overline{\rho' u'}$ is negligible across the RT mixing layer, due to the left–right symmetry of the mushroom-shaped structures, but $\overline{\rho' v'}$ has a peak, at the centre of the RT mixing layer where the density and the vertical velocity fluctuations are

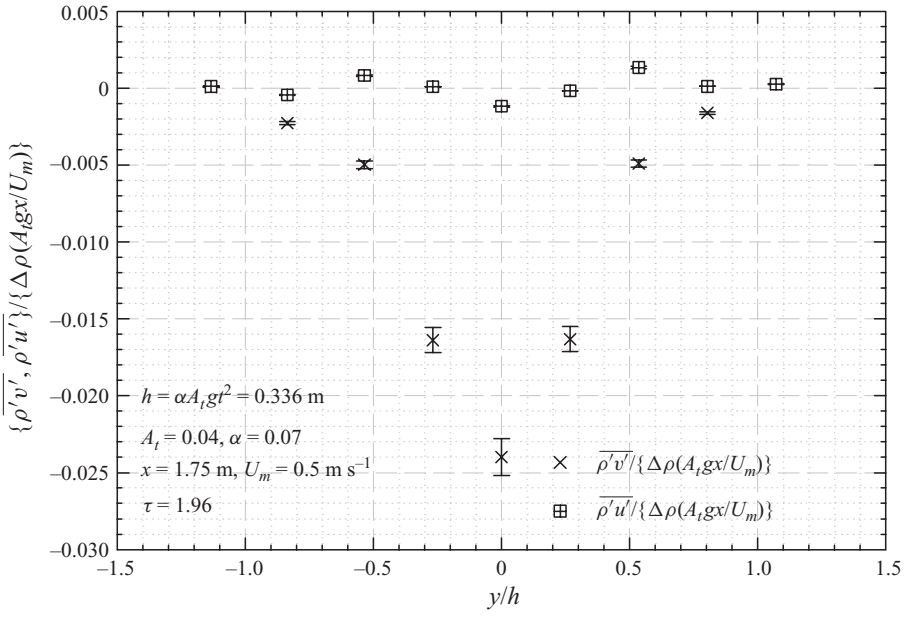

FIGURE 31. Profiles of non-dimensional $\overline{\rho' v'}$ and $\overline{\rho' u'}$ across the RT mixing layer at $\tau = 1.986$ for $A_t = 0.04$ (Note: the error in these measurements of $\overline{\rho' u'}$ non-dimensionalized as shown is $\pm 2.5\,\%$).

strongly correlated. The vertical mass flux is negative because a light packet of fluid is associated with a $\rho' \equiv \rho - \overline{\rho} < 0$ and travels upwards with a velocity $v'(v' > 0)$ and vice versa for a heavy packet of fluid ($\rho' > 0$, $v' < 0$), giving a negative correlation between ρ' and v'.

Figure 32 shows the p.d.f. for $\rho' v'$ inside the RT mixing layer. As in free shear flows, where a bell-shaped distribution (non-Gaussian) is expected (Pope 2000), a significant deviation from Gaussian behaviour was found. The $\rho' v'$ p.d.f. at the RT mixing layer centreline for $\tau = 1.33$ has a large kurtosis, $K_{\rho' v'} = 10.6$, and skewness, $S_{\rho' v'} = -3.8$ ($K = 3$, $S = 0$ for Gaussian), which implies that the mass of fluid at the centreline (vertical mass flux) is predominantly falling. A large peak is found about 0 where small density fluctuations, corresponding to molecularly mixed fluid, result in weak correlations of the velocity and density fluctuations. However, when comparing early- and late-time p.d.f.s, larger negative magnitudes of the turbulent mass flux become more likely as the mixing layer continues to grow. As the RT mixing layer develops downstream gas is entrained into the RT mixing layer at a faster rate, and the layer becomes more turbulent, resulting in large magnitudes of the turbulent mass flux as fluid is transported across the mixing layer. Indeed, the differences in the vertical and horizontal turbulent mass fluxes can also be observed through the measured p.d.f. of $\rho' v'$ and $\rho' w'$ shown in figure 33. The distribution of $\rho' w'$ is centred, and approximately symmetric about zero ($S_{\rho' w'} = 0$), differing sharply with the p.d.f. of $\rho' v'$. Due to symmetry of the mushroomed-shaped plumes (see figure 25), the symmetric behaviour of $\rho' w'$ results in the negligible net contribution of the horizontal mass flux, in contrast with the vertical direction, where mass is transported across the mixing layer through the rising and falling bubbles and spikes. These differences highlight the uniqueness of the buoyancy-driven turbulence and the importance of the vertical turbulent mass flux in the RT mixing layers.

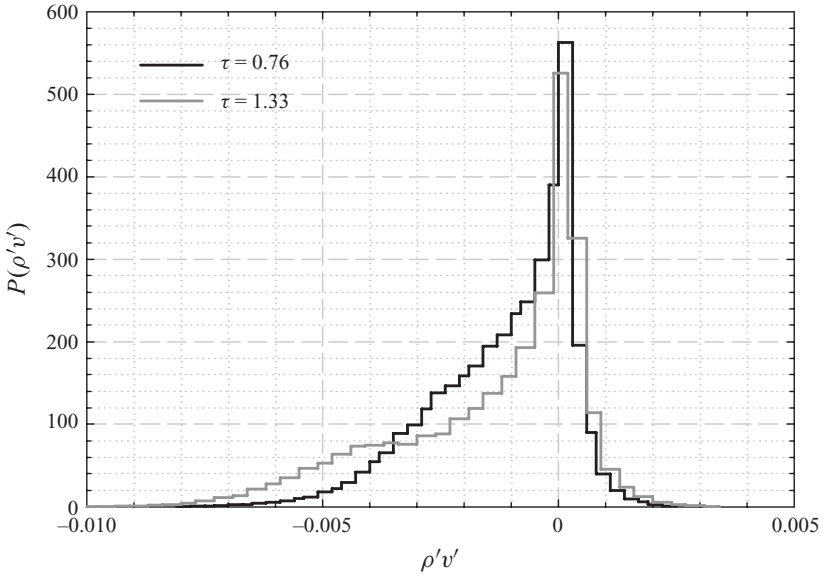

FIGURE 32. The p.d.f. of $\rho'v'$ (kg m^{-2} s^{-1}) at the centreline of the mixing layer for two non-dimensional times technique for an $A_t = 0.03$ experiment.

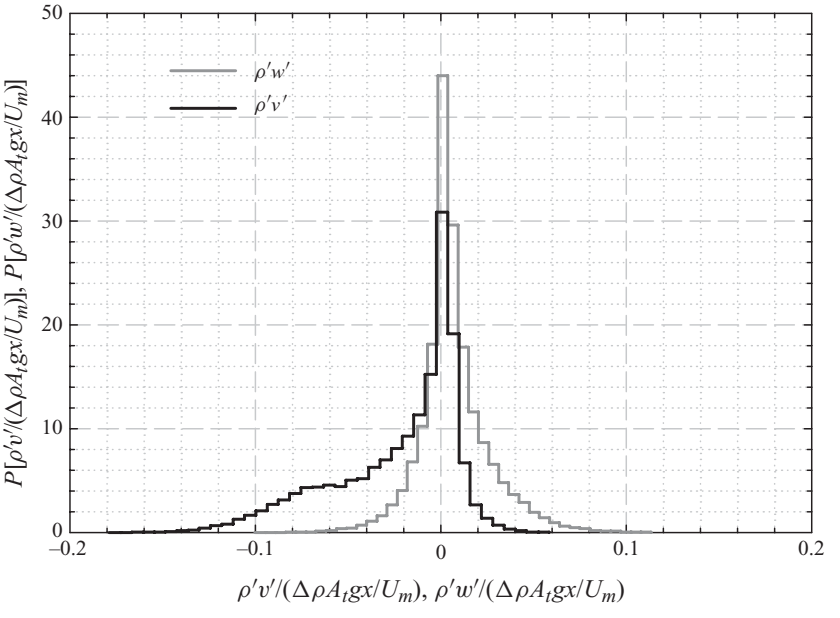

FIGURE 33. Comparison of the $\rho'v'$ and $\rho'w'$ p.d.f. at $\tau = 1.33$ for an $A_t = 0.03$ experiment.

Measurement of energy density spectra. The measured energy density spectra for v', $\overline{f}_{v,1}$ and $\rho'v'$ (mass flux) at the centreline of the mixing layer using the S3WCA technique are shown in figure 34(*a–c*) for early and late times corresponding to $\tau = 0.76$ ($Re_1 = 750$) and $\tau = 1.33$ ($Re_1 = 1450$) at Atwood number 0.03. Fiducials corresponding to $k^{-5/3}$ and k^{-3} are also shown in figure 34(*a–c*), which correspond

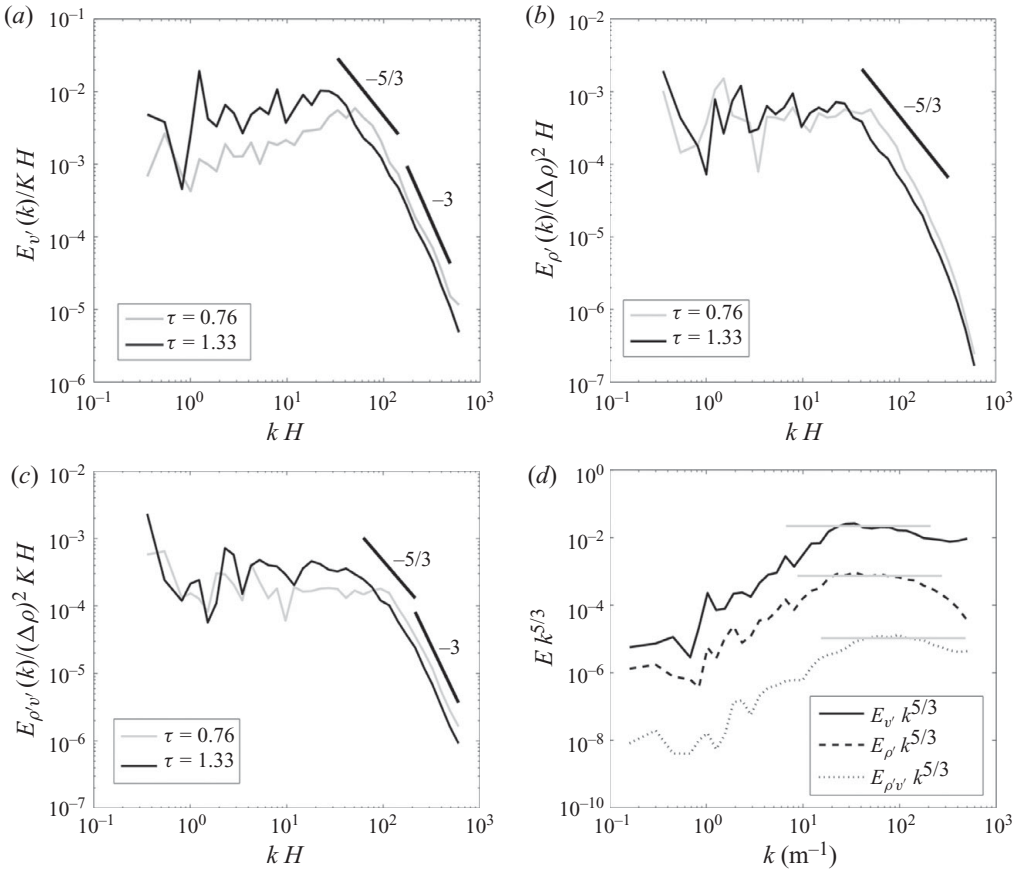

FIGURE 34. The measured energy density spectra for v', ρ' and $\rho'v'$ at the centreline of the mixing layer using the S3WCA technique for an $A_t = 0.03$ experiment. Compensated spectra demonstrating the $-5/3$ slope as a flat line is also shown at $\tau = 1.33$ for each energy density spectra. The spectra are normalized by $\Delta\rho$, K and H.

to the spectral slopes of the two-dimensional Kolmogorov spectrum for the inertial and dissipation subranges of length scales for high Re turbulent flows, respectively. Single-point hot-wire measurements result in a one-dimensional spectrum; however, the Kolmogorov spectrum can still be used as reference. At early time the mixing layer is transitioning to turbulence and an inertial subrange of scales, which transfers energy from the large energy containing length scales to the small viscosity dominated scales, responsible for dissipation, is not found. However, at $\tau = 1.33$ the mixing layer becomes turbulent and loses its two-dimensional nature from the initial conditions and develops three-dimensional structure. The energy cascade from large to small length scales results in an observable inertial subrange of scales in the v' and ρ' fluctuations, as shown by the compensated energy density spectrum, $Ek^{5/3}$, in figure 34(d). Compensated energy density spectra demonstrate the $k^{-5/3}$ behaviour as a flat region in the spectra which allows the inertial subrange of scales to be identified. The observation of inertial scales at Re_h of 1400 and $\tau = 1.33$ is consistent with previous measurements in the water channel by Ramaprabhu & Andrews (2004) and Mueschke *et al.* (2006). From the $\rho'v'$ energy density spectra also shown in figure 34(c), it is evident that fluctuations in the turbulent mass flux are contained

mostly in the large scales of the developing turbulence. This corresponds to large-scale bubbles and spikes of interpenetrating fluid that expand the mixing layer as it develops. As the mixing layer grows, the integral scales increase as larger quantities of fluid are entrained into the edges of the mixing layer, giving an increase in the fluctuations of the turbulent mass flux for large scales of the turbulence. It is unclear in the $\rho' v'$ energy density spectra, however, what power law decay is observed and no previous measurements have been found in the literature for RT-driven turbulence. For low-Reynolds-number turbulent flows, such as decaying grid turbulence with passive scalars (Mydlarski 2003), the co-spectrum for velocity and passive scalars was found to closely follow the behaviour of the velocity field (although this is not buoyancy-driven). We plot the power spectral density of the mass flux $\overline{\rho' v'}$ as it a primary transport term in an RT flow and a complete characterization is important for development and validation of closure models for such flows. There also appears to be a strong correlation between the $\rho' v'$ energy density spectra and the v'spectrum measured here. Therefore, the $k^{-5/3}$ and k^{-3} lines are added as a reference. However, the mixing layer does not have a sufficient range of scales to make a definitive assessment of the spectral behaviour. To better determine the spectral distribution of energy in turbulent fluctuations, a higher Reynolds number (larger range of scales) is required. Similarities between the distribution of energy in $v'$and $\rho' v'$ are more clearly seen in the compensated energy density spectra of figure 34(d), as both compensated spectra show similar distributions of energy throughout the range of length scales measured.

Energy budget. From our simultaneous measurements of velocity and density fields, the net kinetic energy dissipation per unit cross-section from the initial state of the flow has been calculated, in a fashion similar to Youngs (1994) and Ramaprabhu & Andrews (2004). However, our use of MPMO differs from Ramaprabhu & Andrews (2004) who used a particle image velocimetry diagnostic to simultaneously measure density and turbulent KE. The initial potential energy per horizontal unit cross-section, PE_i, associated with the flow, is calculated assuming a step-function at $y = 0$ (centreline) for the density profile at $\tau = 0$. Thus,

$$PE_i = \int_{-h_s}^{h_b} \rho_{step} g y \, \mathrm{d}y = \int_{-h_s}^{0} \rho_1 g y \, \mathrm{d}y + \int_{0}^{h_b} \rho_2 g y \, \mathrm{d}y. \tag{5.20a}$$

At $\tau = 0$, the kinetic energy per unit cross-section $KE_i \sim 0$, since there is negligible energy associated with initial velocity fluctuations. Further downstream the potential energy at $\tau = 1.986$ is computed from the measured density profile as

$$PE_f = \int_{-h_s}^{h_b} \bar{\rho} g y \, \mathrm{d}y = \int_{-h_s}^{0} \overline{\rho} g y \, \mathrm{d}y + \int_{0}^{h_b} \overline{\rho} g y \, \mathrm{d}y \cong \sum_{i=0}^{n} \rho_i g y_i \Delta y. \tag{5.20b}$$

The potential energy released to the flow by $\tau = 1.986$ is then given by $PE_{released} = PE_f - PE_i$. Some of this energy is converted into kinetic energy, which can be directly obtained from our measured velocity profiles of u'_{rms} and v'_{rms}, and the remainder has been dissipated. Axisymmetric mushroom structures imply we may take the turbulence as homogeneous with respect to the streamwise direction x and the spanwise direction z, and set $\overline{u'^2} = \overline{w'^2}$ based on known properties for the RT mixing layer. Then,

$$KE_{generated} = \frac{1}{2} \int_{-h_s}^{h_b} \rho (2\overline{u'^2} + \overline{v'^2}) \, \mathrm{d}y, \tag{5.21}$$

and the net kinetic energy dissipation is given by

$$D = PE_{released} - KE_{generated}. \tag{5.22}$$

Thus, the net KE dissipation as a fraction of the potential energy released, $D/PE_{released}$, was determined from our measurements at $A_t = 0.04$ in the present gas channel to be 0.48 (i.e. 48 %) at $\tau \sim 1.986$ (for $A_t = 0.04$). Ramaprabhu & Andrews (2004) obtained a value of 0.49 at $\tau \sim 1.21$. Youngs (1991) reported a value of 0.54 obtained from three-dimensional numerical simulations at $A_t = 0.2$. The value obtained from two-dimensional simulations (Youngs 1991) was significantly less ($D/PE_{released} \sim 0.06$) since dissipation is primarily a three-dimensional mechanism. For a self-similar mix, characterized by the length scale gt^2, it is expected that $D/PE_{released}$ and $KE_{generated}/PE_{released}$ become constant in the self-similar regime (Youngs 1991; Ramaprabhu & Andrews 2004). Thus, we find good agreement between the present experiments and related, but higher Atwood number, three-dimensional simulations and the PIV-based measurements of Ramaprabhu & Andrews (2004).

Evaluation of turbulence model constants. Our data for $A_t = 0.04$ are sufficient for us to perform several turbulence model constant evaluations. In particular, we consider the primary momentum transport flux $\overline{\rho' v'}$, for which a model representation is to use the gradient diffusion hypothesis (Pope 2000) as

$$\overline{\rho' v'} = -\frac{\nu_t}{\sigma_t}\frac{\partial \rho}{\partial y} = -\frac{C_\mu k^{1/2} \ell_m}{\sigma_t}\frac{\partial \rho}{\partial y}, \tag{5.23}$$

where ν_t is the turbulent viscosity and the scalar turbulent Prandtl number, σ_t, takes a value of 0.7 (as will become evident this value is somewhat arbitrary and is selected because it is a typical value used in free mixing layer calculations; Blackwell 1973; White 1991; Snider & Andrews 1996). The primary transport in our small Atwood experiments is associated with the largest structures and these are of size h_b ($= h_s$ at small Atwood), thus we take the integral length scale l_m as h_b, and the density gradient $\partial\rho/\partial y = \Delta\rho/2h_b$ (the factor 2 arises because h_b is the half RT mixing width and, as figure 8 shows, the density profile is reasonably linear across the small Atwood RT mixing layer). Our measurements at the centreline indicate that $\overline{u'^2} = \overline{w'^2} = 0.3\,\overline{v'^2}$ so the turbulence kinetic energy [$k = (\overline{u'^2} + \overline{v'^2} + \overline{w'^2})/2$] is given by $k = 0.8\overline{v'^2}$. Figure 23 plots the collapse of the centreline r.m.s. vertical velocity (v'_{rms}) to obtain a measured centreline α_{CL} of 0.07. Using (5.9*b*), the centreline turbulence kinetic energy is given by $k = 0.8(2\alpha_{CL} A_t g\, x/U_m)^2$. Substitution into (5.23) gives the following expression for a measurement of C_μ:

$$C_\mu = -\frac{\sigma_t}{\sqrt{0.8}\Delta\rho\alpha_{CL}}\frac{\overline{\rho' v'}}{\left\{A_t g \dfrac{x}{U_m}\right\}}. \tag{5.24}$$

Figure 30 plots measured values of $\overline{\rho' v'}/(\Delta\rho(A_t g\, x/U_m))$, that at late time ($\tau = 1.986$) reach a value of -0.024, giving a corresponding value for C_μ of 0.288. A typical value quoted for C_μ for a homogeneous turbulent fluid is 0.09 (Speziale 1991; Launder & Spalding 1974), that corresponds to turbulent shear flows and flow situations where the mixing layer grows at t or a fractional power of t (Pope 2000). In our present buoyancy-driven flow case, the mixing layer grows as t^2 and there is time-lag in transferring the turbulent kinetic energy to the smaller scales, resulting in a change in value of the constant C_μ. Measured C_μ at the centreline for the different downstream locations are given in table 7, and show that the value of C_μ remains approximately constant at various downstream locations, and is independent of the Reynolds number

x (cm)	τ	$\frac{\overline{\rho' v'}}{\Delta\rho(A_t g t)}$	α_{CL}	C_μ
50	0.567	−0.0482	0.12169	0.3098
75	0.851	−0.03812	0.09268	0.3219
100	1.135	−0.02878	0.07709	0.2922
125	1.418	−0.02634	0.06743	0.3057
150	1.702	−0.02444	0.06741	0.2838
175	1.986	−0.02397	0.06520	0.2877
195	2.213	−0.02363	0.06583	0.2809

TABLE 7. Turbulence modelling constant (C_μ) at different downstream distances (x) and corresponding non-dimensional times (τ).

of the developing flow. This constant value for C_μ is because it is determined at the integral scales of the flow, which in our case are dominated by large-scale developing plumes. The gradient diffusion model constant C_μ can also be evaluated from the measurement of the integrated dissipation D given in (5.22). Based on a mixing-length model, the dissipation ε can be modelled as (Pope 2000)

$$\varepsilon = C_\mu \frac{k^{3/2}}{l_m}, \tag{5.25}$$

where l_m is a mixing length. Integrating (5.25) across the mixing layer, we obtain

$$\int_{-h_s}^{h_b} \varepsilon \mathrm{d}z = D = C_\mu \int_{-h_s}^{h_b} \frac{k^{3/2}}{l_m} \mathrm{d}z. \tag{5.26}$$

Since D is the integrated dissipation and C_μ does not change significantly along the flow (see table 7), we can use (5.26) to check our measurement of C_μ from the gradient diffusion approximation. As before $l_m \sim h_b$, then from (5.26) we obtain a value for C_μ of 0.26 at $x = 1.75$ m ($\tau = 1.986$) from the splitter plate in good agreement with the value of 0.288 from the gradient diffusion approximation above.

5.2.2. *Detailed measurements in high-Atwood-number Rayleigh–Taylor experiments*

We also report the first experimental measurements of turbulent statistics in the RT mixing layer at large Atwood numbers. The S3WCA diagnostic was used in conjunction with temperature as a fluid marker to measure both instantaneous and time-averaged statistics and their spectra at $A_t = 0.6$. A temperature difference of $\sim 5^\circ$C was used between the inlet streams. Since the RT mixing layer at these high-Atwood-number experiments contain large concentrations of helium, $f_{v,He} \leqslant 0.88$, special care has been exercised in analysing the hot- and cold-wire traces. The raw data were filtered to four times the spatial resolution of the combined probes ($freq_{max} = 83$ Hz) to increase the probability that both the cold- and hot-wire sensors measure the same fluid structure. Details about the hot-wire analysis and data reduction procedure may be found elsewhere (Bruun 1995; Kraft 2008; Kraft *et al.* 2009).

Figure 35(a) shows a comparison of the molecular mix parameter θ measured in the $A_t = 0.6$ RT mixing layer with our low-Atwood experiments. Since the cold-wire thermometer and subsequent measurements of density can be analysed independently of the hot-wire diagnostic, the cold-wire data were re-analysed at its Nyquist limit of 666 Hz at $U_m = 2.0$ m s^{-1} to include the maximum range of scales possible in the measurement of θ. The values are plotted in figure 35(a) to compare with our low-Atwood-number measurements. It was found that the time evolution of θ at $A_t = 0.6$ is similar to the low-Atwood measurements (using the MPMO technique), and as before,

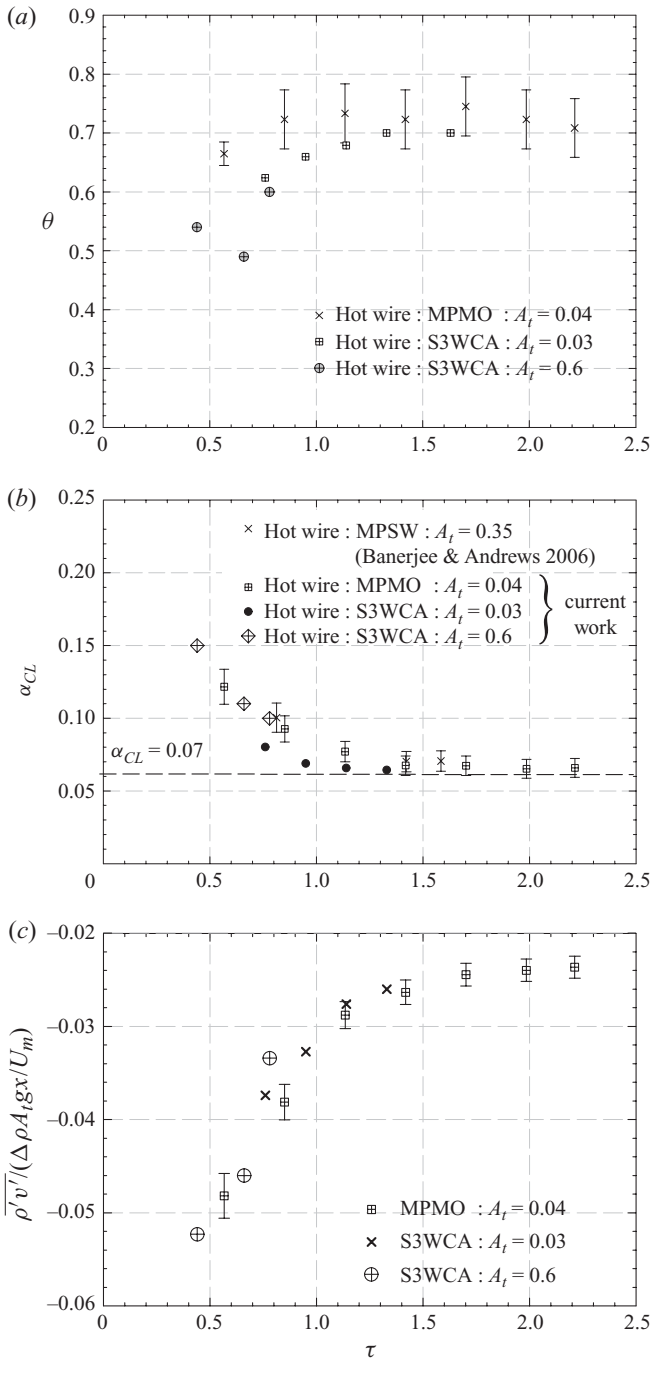

FIGURE 35. Measurements of (*a*) molecular mix parameter θ, (*b*) growth parameter α_{CL} and (*c*) non-dimensional vertical turbulent mass flux at the mixing layer centreline for $A_t = 0.6$ compared with the low $A_t = 0.03$–0.04 measurements using MPMO and S3WCA techniques.

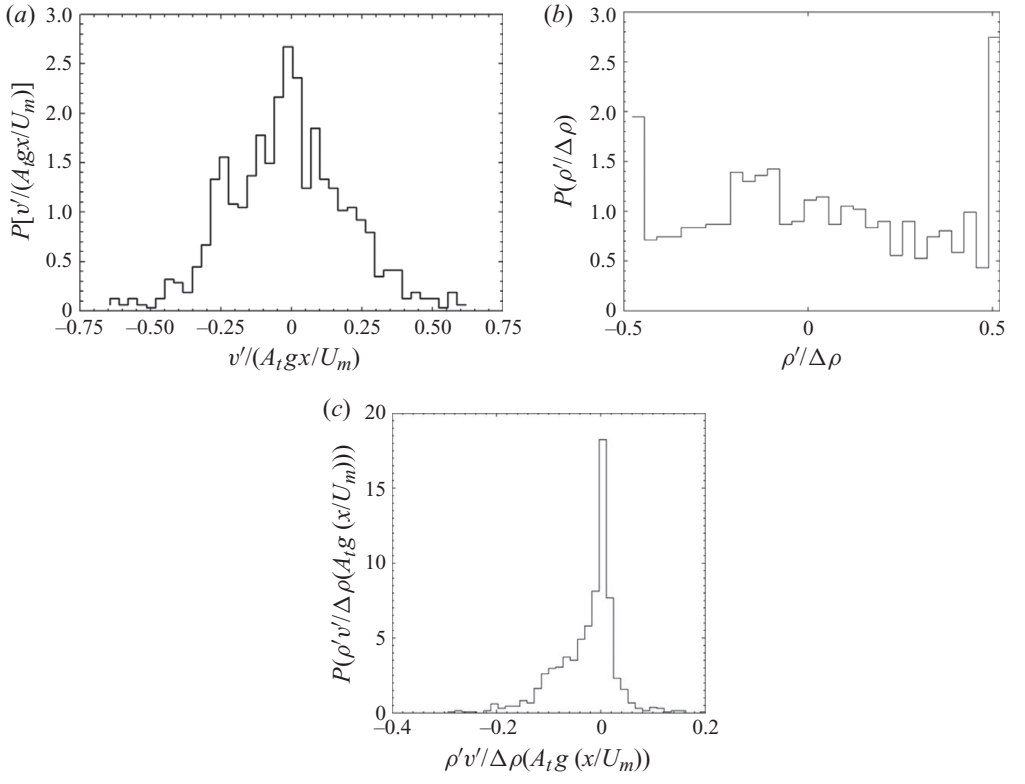

FIGURE 36. P.d.f. of the (*a*) velocity fluctuations, v' (m s^{-1}), (*b*) density fluctuations, ρ' (kg m^{-3}) and (*c*) turbulent mass flux (velocity–density fluctuations), $\rho' v'$ (kg m^{-2} s^{-1}) at $\tau = 0.78$ at the mixing layer centreline for $A_t = 0.6$.

demonstrates a significant decrease in the amount of molecular mixing at early time in the developing buoyancy-driven mixing layer. In addition, when considering the combined data from our current work at low- and high-Atwood-number mixing layers of helium and air ($Sc \sim 1$), larger magnitudes of molecular mixing are found overall when compared with the water channel results of Mueschke *et al.* (2006) with $Pr \sim 7$. Mixing layers associated with higher Sc (or Pr in the water channel experiments) show a reduced amount of molecular mixing due to lower rates of molecular diffusion (whether mass or temperature diffusion). Details about molecular mixing at high Sc flows can be found in Mueschke *et al.* (2009) who have used a reacting RT flow to determine the effect of molecular diffusivities on the dynamics of turbulent mixing in RT mixing layers. Figure 35(*b*) compares the growth parameter, α_{CL} at $A_t = 0.6$ with low-Atwood measurements. The figure shows that early time ($\tau \leqslant 0.78$) values of α_{CL} for the high-Atwood measurement are similar to the measured values for $A_t \leqslant 0.04$, and that the primary turbulent mass flux, $\overline{\rho' v'}$, at $A_t = 0.6$, when non-dimensionalized using (5.24) was similar to the measured values at $A_t < 0.04$ (see figure 35*c*).

Since the S3WCA diagnostic also yields instantaneous information for the fluid turbulence, p.d.f.s for density and velocity fluctuations at $\tau = 0.78$ are shown in figure 36(*a–c*) at the mixing layer centreline ($y = 0$) for $A_t = 0.6$. The kurtosis of the velocity fluctuation distributions, a measure of the flatness of

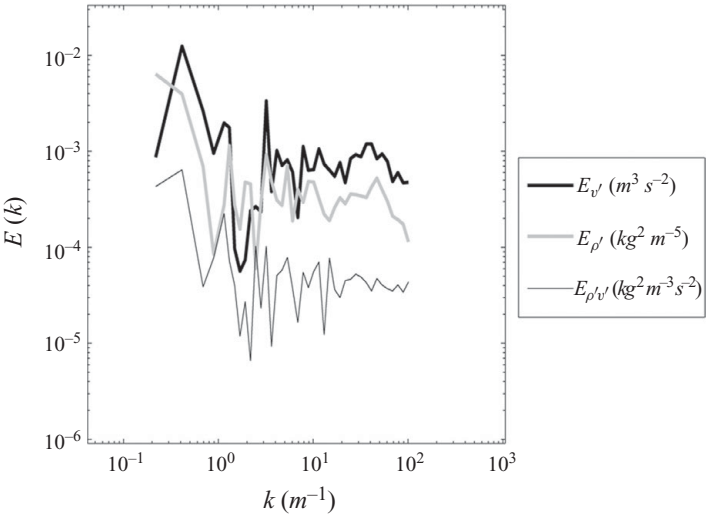

FIGURE 37. The measured energy density spectra for v', ρ' and $\rho'v'$ at the centreline of the mixing layer for $A_t = 0.6$, $\tau = 0.78$ and $U_m = 2.0\ \mathrm{m\,s^{-1}}$. The reduced resolution to compensate for large concentrations of helium limits the frequency response to 83 Hz.

the distribution, is $K_v = 3.3$ and $K_w = 4.6$. These values are larger than reported earlier for $A_t = 0.03$ at $\tau = 1.33$ of $K_v = 2.17$ and $K_w = 2.97$. The kurtosis of the cross-stream velocity fluctuations is 40 % larger than the kurtosis of the vertical velocity fluctuations, demonstrating the anisotropy of buoyancy-driven turbulence. For $\tau = 0.78$ and $A_t = 0.6$ the ratio of the r.m.s. of vertical to cross-stream velocity fluctuations is 1.5. The density fluctuation p.d.f., also shown in figure 36(b), shows a bi-modal distribution as seen at $A_t = 0.03$ for a similar time of evolution. The p.d.f. of the vertical turbulent mass flux, $\rho'v'$ at $\tau = 0.78$ is shown in figure 36(c), and is similar to that found at the low-Atwood-numbers experiment (see figure 32). Primarily negative turbulent mass fluxes in the vertical direction were expected, as bubbles of mostly light fluid rise and spikes of mostly heavy fluid fall through the mixing layer. This negative correlation of vertical velocity and density fluctuations results in a broad tail of the p.d.f. towards negative values of the turbulent mass flux. In addition, the presence of mixed fluid in both the rising bubbles and falling spikes results in the large peak about zero. The skewness (third moment of the distribution) and kurtosis (fourth moment of the distribution) of the p.d.f. can be used to quantitatively characterize the shape of the distribution. For the p.d.f. shown in figure 36(c), $K_{\rho'v'} = 9.5$ and $S_{\rho'v'} = -2.7$. These are similar to those found at $A_t = 0.03$ and $\tau = 1.33$ of $K_{\rho'v'} = 10.6$ and $S_{\rho'v'} = -3.8$. However, the negative tail of the p.d.f. does extend to larger non-dimensional values of the turbulent mass flux which can be attributed to the asymmetries between the bubbles and spikes at large A_t flows. Figure 37 shows the measured energy density spectra of v', ρ' and $\rho'v'$. The frequency of these measurements is restricted to the actual sampling frequency of 83 Hz, or a final spatial resolution within the Nyquist limit of $\sim$3.5 cm, which was done to ensure that both the hot- and cold-wire probes measured the same fluid inside the RT mixing layer. When compared with the measured spectra for $A_t = 0.03$, it is evident that only the large-scale energy-containing region is captured by the diagnostic for $A_t = 0.6$. The measured spectrum of figure 37, though limited by the sampling frequency, is the first of its kind at these high-Atwood-number flows. The energy spectra does not exhibit an inertial

range as the measurements were made at early time ($\tau = 0.76$) and the turbulence was not fully mature. This limitation in spectra can be improved by using a customized commercial probe with a smaller spatial resolution and integrated cold wires. Thus, our early time ($\tau \leqslant 0.78$) high-Atwood measurements at the mixing layer centreline are consistent with those obtained from the low Atwood numbers ($A_t \leqslant 0.04$). Although the penetration of the bubbles and spikes clearly grows asymmetrically, as indicated by the measurements of h_b and h_s, time-averaged statistics of velocity and density fluctuations and the velocity–density correlation at the mixing layer centreline show striking similarities to the more symmetric lower-Atwood-number mixing layers as shown in figure 35(*c*). The only difference that was observed was in the measured p.d.f. of $\rho' v'$ that extended to larger normalized negative magnitudes of the turbulent mass flux than observed at low Atwood numbers. Table 5(*c*) reports all the turbulent statistics measured at three downstream location in a $A_t = 0.6$ RT mixing layer. We do not report measurements of streamwise $\overline{u'^2}$ as the error associated with measuring the mean streamwise velocity, $U(= 2\ \mathrm{m\,s^{-1}}$ at $A_t = 0.6)$, overwhelms the $\overline{u'^2}$ measurement (Jorgenson 1971; Andreopoulos 1983; Frota & Moffat 1983; Bruun 1995). The mean cross-stream velocities V and W are ~ 0, making the measurements of $\overline{v'^2}$ and $\overline{w'^2}$ reliable (errors of $\sim 10\,\%$).

5.2.3. *Conditional statistics in Rayleigh–Taylor mixing layers*

Conditional averaging of our instantaneous measurements using the S3WCA diagnostic was utilized to separately investigate the bubble and spike dynamics inside the air–helium RT mixing layer. Although conditional averaging techniques have been used extensively for shear-driven turbulent flows (Antonia 1981), the authors believe that the conditional measurements reported here are the first of their kind for RT experiments and allow investigation of interesting aspects in the buoyancy-driven mixing layer, which is observed through conventional averaging techniques.

Bubble and spike dynamics using conditional statistics. The measured data traces were conditionally sampled using the density fluctuation $\rho'(= \rho - \bar{\rho}_{mix})$ in the intermittency function of (3.10). At the geometric centreline of our air–helium mixing layer, the average density of the mixing layer is approximately $\overline{\rho}_{mix}$, so that if $\rho' > 0$, the passing fluid is composed mostly of air (heavy fluid : spike), the inverse being true if $\rho' < 0$. The p.d.f.s of ρ', v' and $\rho' v'$ plotted (see figure 38*a–c*) at $A_t = 0.03$ and $\tau = 1.33$ demonstrate this procedure. It is observed that the p.d.f.s for the vertical (dominant) velocity fluctuations v', separated into spikes and bubbles, are nearly symmetric (figure 38*b*). The lighter fluid, $\rho' < 0$, associated with the rising bubbles corresponds to mostly positive vertical velocity fluctuations. The opposite is true of the heavy fluid, $\rho' > 0$. This is expected as RT mixing layers are dominated by the formation of bubbles and spikes, resulting in a strong negative correlation of density and vertical velocity fluctuations. Figure 38(*b*) also shows an overlap of the two distributions, which implies that the heavy fluid ($\rho' > 0$) does not always correspond with negative vertical velocity fluctuations, and light fluid ($\rho' < 0$) does not always correspond with positive vertical velocity fluctuations. The entrainment of the heavy fluid in the rising bubbles occurs through the Kelvin–Helmholtz-driven roll-up of the buoyant plumes and shearing of the bubbles and spikes as they move past each other. The inverse is also true as light fluid is entrained into the falling spikes. Also, as expected for the low-Atwood-number RT mixing layers, the amount of heavy fluid entrained into rising bubbles and vice versa appears to be equal about the mixing layer centreline. This is indicated by the equal and opposite tails of the v' p.d.f.s

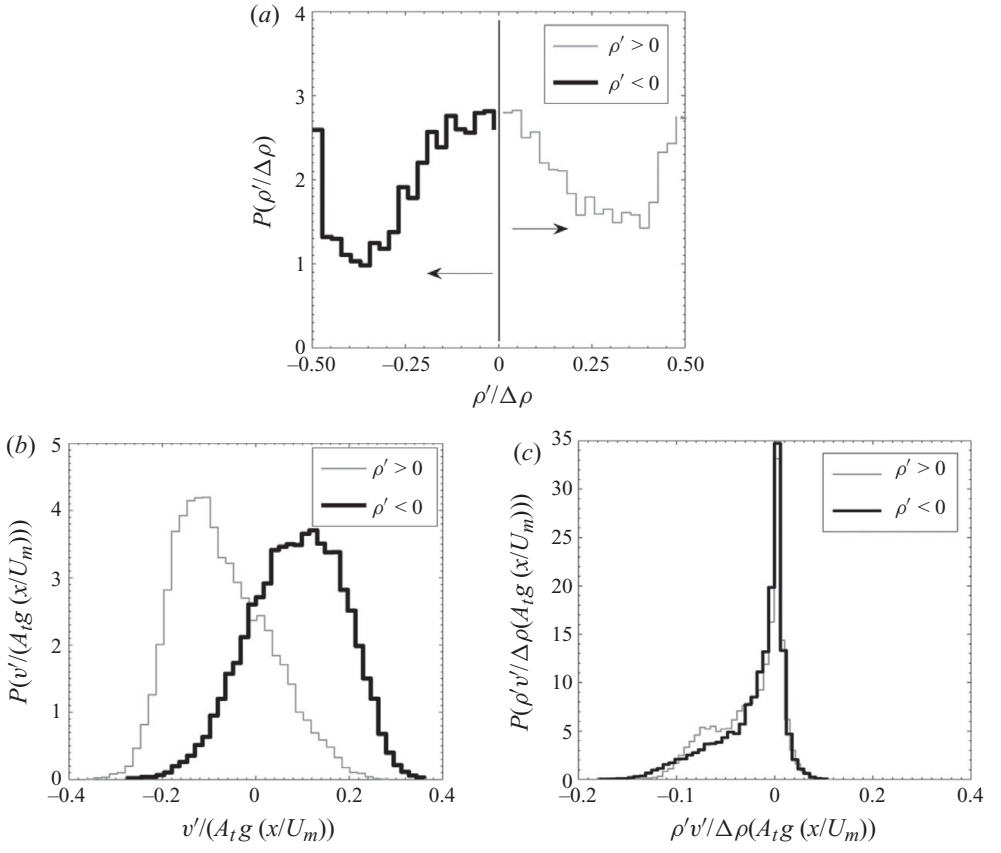

FIGURE 38. P.d.f. of ρ', v' and $\rho' v'$ at the mixing layer centreline for $A_t = 0.03$ and $\tau = 1.33$, using the sampling condition of $\rho' > 0$ and $\rho' < 0$ to approximate the measured fluctuations as two fluids (heavy or light). The sampling condition used is illustrated in the p.d.f. of ρ' in (a).

at $|v'(A_t g\, x/U_m)| = 0.2$ (see figure 38b). The symmetric penetration and behaviour of bubbles and spikes is also demonstrated in the conditional p.d.f. of the vertical turbulent mass flux, $\rho' v'$. Both conditions, $\rho' < 0$ and $\rho' > 0$, demonstrate identical p.d.f.s with approximately equal mean vertical turbulent mass fluxes, $\overline{\rho' v'}$, which are listed in table 8. The original intent of using the density fluctuation ($\rho' < 0$ and $\rho' > 0$) for the conditional measurements was to separate the flow measurements into bubbles and falling spikes. However in the p.d.f.s of figure 38(b), it was shown that when using the $\rho' < 0$ and $\rho' > 0$ conditions to separate the bubble and spike behaviours of the buoyancy-driven flow, not all of the fluid in either condition was rising ($+v'$) or falling ($-v'$). Therefore it seems appropriate to also examine an additional conditional statistic based on the sign of the vertical velocity fluctuation v' to decompose the measurements approximately into bubble and spike dynamics such that $v' < 0$ corresponds to falling spikes and $v' > 0$ indicates rising bubbles. P.d.f.s of ρ', v' and $\rho' v'$ at $A_t = 0.03$ and $\tau = 1.33$ are shown in figure 39(a–c). An illustration of the vertical velocity condition is shown in the p.d.f. of v' (figure 39a). The entrainment of light fluid into the spikes and heavy fluid into the bubbles is clearly evident in the p.d.f. of ρ'plotted in figure 39(b). The p.d.f.s of $\rho' v'$ based on the of v', plotted in figure 39(c), were also found to be approximately identical. A summary of conditional statistics

	Conditional averaging				
	Method 1		Method 2		Conventional averaging
Variables	$\rho' > 0$	$\rho' < 0$	$v' > 0$	$v' < 0$	
v'_{rms}	0.079	0.079	0.054	0.056	0.10
$\overline{v'}$	−0.065	0.063	−0.086	0.085	0
ρ'_{rms}	0.011	0.011	0.016	0.015	0.020
f_1	0.72	0.27	0.67	0.31	0.51
$\frac{\overline{\rho' v'}}{\Delta\rho(A_t g t)}$	−0.027	−0.026	−0.027	−0.026	−0.026

TABLE 8. Summary of conditional averages for $A_t = 0.03$ ($\Delta\rho = 0.074$ kg m^{-3}) and $\tau = 0.78$ at the mixing layer centreline ($y = 0$).

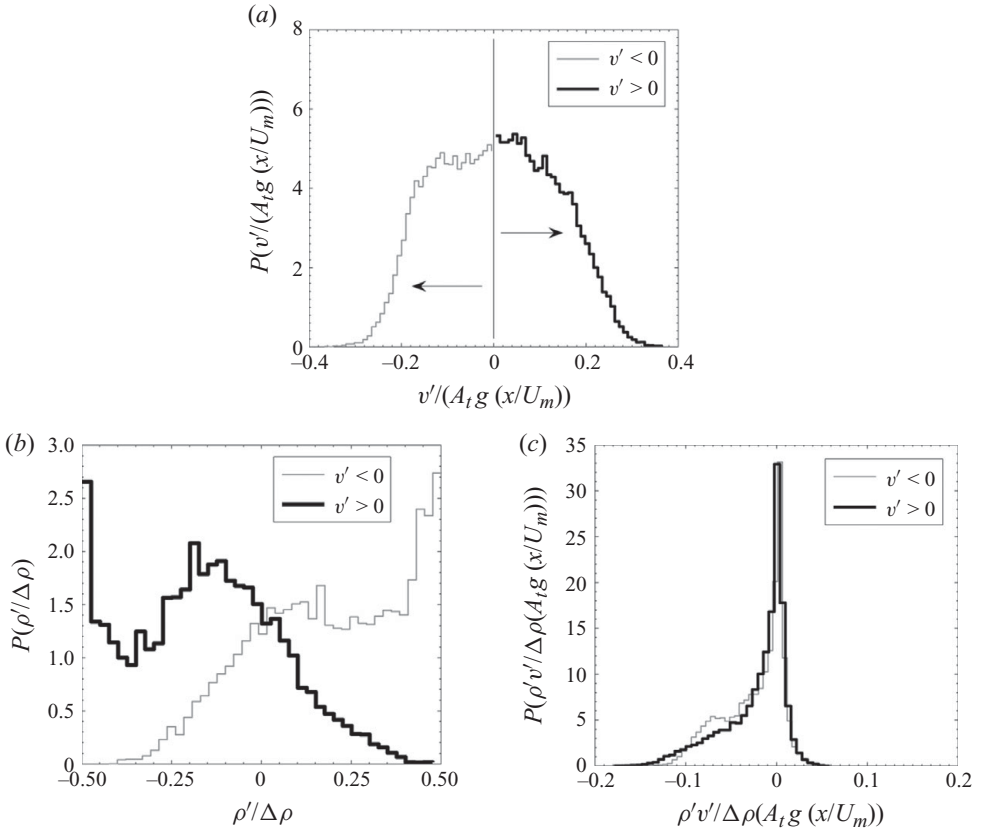

FIGURE 39. P.d.f. of ρ', v' and $\rho' v'$ at the mixing layer centreline for $A_t = 0.03$ and $\tau = 1.33$, using the sampling condition of $v' < 0$ and $v' > 0$ to approximate the measured fluctuations as a bubble (rising fluid) or spike (falling fluid). The sampling condition used is illustrated in the p.d.f. of v' in (*a*).

using the described conditions is presented in table 8. It is observed that depending on whether the mean or r.m.s. of the conditioned v' distributions is considered based on conditional parameters, ρ' or v', the magnitudes are approximately equal as expected at the centreline, with the symmetrical penetration of bubbles and spikes at $A_t = 0.03$.

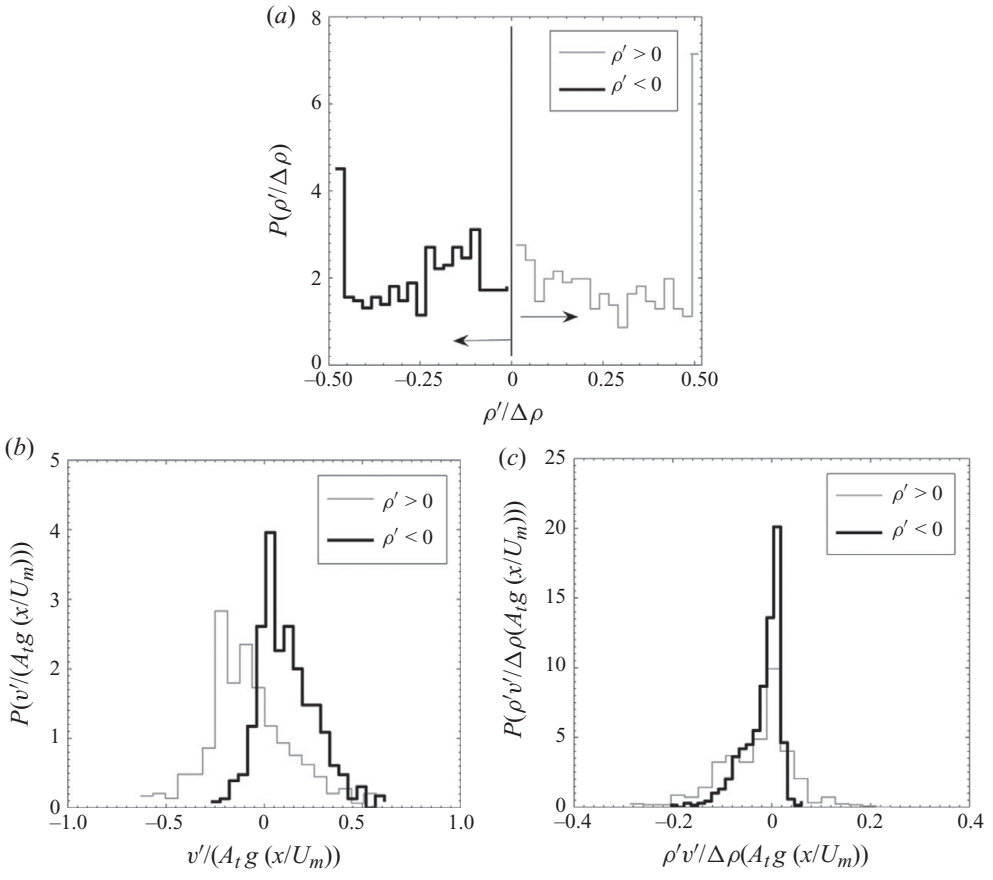

FIGURE 40. P.d.f. of ρ', v' and $\rho' v'$ at the mixing layer centreline for $A_t = 0.6$ and $\tau = 0.78$, using the sampling condition of $\rho' > 0$ and $\rho' < 0$ to approximate the measured fluctuations as two fluids (heavy or light). The sampling condition used is illustrated in the p.d.f. of ρ' in (*a*).

However, no inference can be made regarding which conditioning method or velocity statistic is better suited to determining a characteristic velocity scale for the bubbles or spikes.

Measurements of various parameters at $A_t = 0.6$ (described in § 5.2.2) were found to be consistent with the low A_t measurements at the mixing layer centreline. Although the asymmetric behaviour and differing dynamics of the bubbles and spikes were evident through our imaging measurements of the RT mixing layer (see figure 7*b*), such asymmetries were not observed in the turbulent and mixing statistics obtained from the hot-wire data (on using conventional averaging techniques). Further investigation into the mixing layer dynamics was performed by re-examining the measured conditional statistics at $A_t = 0.6$ using the conditional sampling procedure described for the low A_t measurements. Figure 40(*a–c*) shows p.d.f.s of ρ', v' and $\rho' v'$ for $A_t = 0.6$ and $\tau = 0.78$ at the mixing layer centreline ($y = 0$) using the $\rho' > 0$ and $\rho' < 0$ conditions. Unlike the low A_t conditional measurements (figure 38*a*,*b*), the p.d.f.s of the vertical velocity fluctuations plotted in figure 40(*b*) were not symmetric. Instead, more of the heavier fluid ($\rho' > 0$) was carried back up towards the top of the mixing layer after being entrained into the rising bubbles, than light fluid being carried down back down through the mixing layer by the falling spikes. As a result, v'_{rms} for each condition is not equal; rather, v'_{rms} for the fluid associated with $\rho' > 0$ (heavier fluid) is approximately

	Conditional averaging				
	Method 1		Method 2		Conventional averaging
Variables	$\rho' > 0$	$\rho' < 0$	$v' > 0$	$v' > 0$	
v'_{rms}	0.45	0.31	0.35	0.25	0.44
$\overline{v'}$	−0.21	0.19	−0.33	0.34	0
ρ'_{rms}	0.15	0.13	0.24	0.22	0.26
f_1	0.76	0.25	0.64	0.34	0.51
$\frac{\overline{\rho' v'}}{\Delta\rho(A_t g t)}$	−0.042	−0.025	−0.046	−0.021	−0.033

TABLE 9. Summary of conditional averages for $A_t = 0.6$ ($\Delta\rho = 0.88\,\mathrm{kg\ m^{-3}}$) and $\tau = 0.78$ at the mixing layer centreline ($y = 0$).

Averaging method		A_t	τ	$\overline{\rho v'}/\overline{\rho}$	$\overline{\rho v'^2}/\overline{\rho}$	$\overline{\rho v' w'}/\overline{\rho}$	$\overline{\rho}$
Conditional averaging	$\rho' > 0$	0.03	1.33	−0.065	0.011	4×10^{-5}	1.15
	$\rho' < 0$			0.062	0.010	-1.1×10^{-3}	1.12
	$v' > 0$			−0.086	0.010	2.0×10^{-4}	1.15
	$v' > 0$			0.085	0.010	-2.0×10^{-4}	1.12
Conventional averaging				−0.001	0.010	-5.2×10^{-4}	1.14
Conditional averaging	$\rho' > 0$	0.6	0.78	−0.24	0.26	−0.004	0.97
	$\rho' < 0$			0.19	0.14	0.026	0.51
	$v' > 0$			−0.39	0.22	0.007	0.86
	$v' > 0$			0.37	0.22	0.007	0.60
Conventional averaging				−0.018	0.21	0.007	0.76

TABLE 10. Conditional statistics using density-weighted averages.

1.5 times larger (see table 9) than that of the fluid determined from the condition $\rho' < 0$ (lighter fluid). Imaging measurements at $A_t = 0.6$ (figure 11) clearly shows that spikes of heavy fluid penetrate into the light fluid farther than bubbles of light fluid penetrate into the heavy fluid. Therefore, it can be inferred that negative vertical velocities associated with the spikes could be larger in magnitude. From the v' p.d.f., it was also observed that a larger amount of heavy fluid was entrained into the bubbles than the amount of light fluid entrained in the faster moving spikes. As a result, the v'_{rms} from each of the ρ' conditions are not equal. However, $\overline{v'}$ for the bubbles and spikes are approximately equal and opposite, which is expected since, at the mixing layer centreline, approximately equal quantities of the two fluids are present. Since the mean of the conditional v' measurements are approximately equal but opposite in sign, the net volume flux of the incompressible flow is approximately zero, satisfying volume conservation at the mixing layer centreline for the incompressible mixing layer. It is of interest to compare the $\rho' v'$ p.d.f. for the vertical turbulent mass flux for each ρ' condition (see figure 40*c*). Unlike the low A_t conditional measurements, the $\rho' v'$ p.d.f. is not identical as the heavy fluid is more likely to contain negative vertical turbulent mass flux of larger magnitude. Once these conditional distributions are averaged, it is observed that there is an imbalance in the turbulent vertical mass flux; where $\overline{\rho' v'}$ for the heavy fluid is 1.7 times larger than that for the lighter fluid (table 10). Thus consistency between the conventional and conditioned averages that is observed in the low A_t measurements (where the mixing layer is symmetric) is not observed in the high A_t measurements (where the mixing layer is asymmetric). So

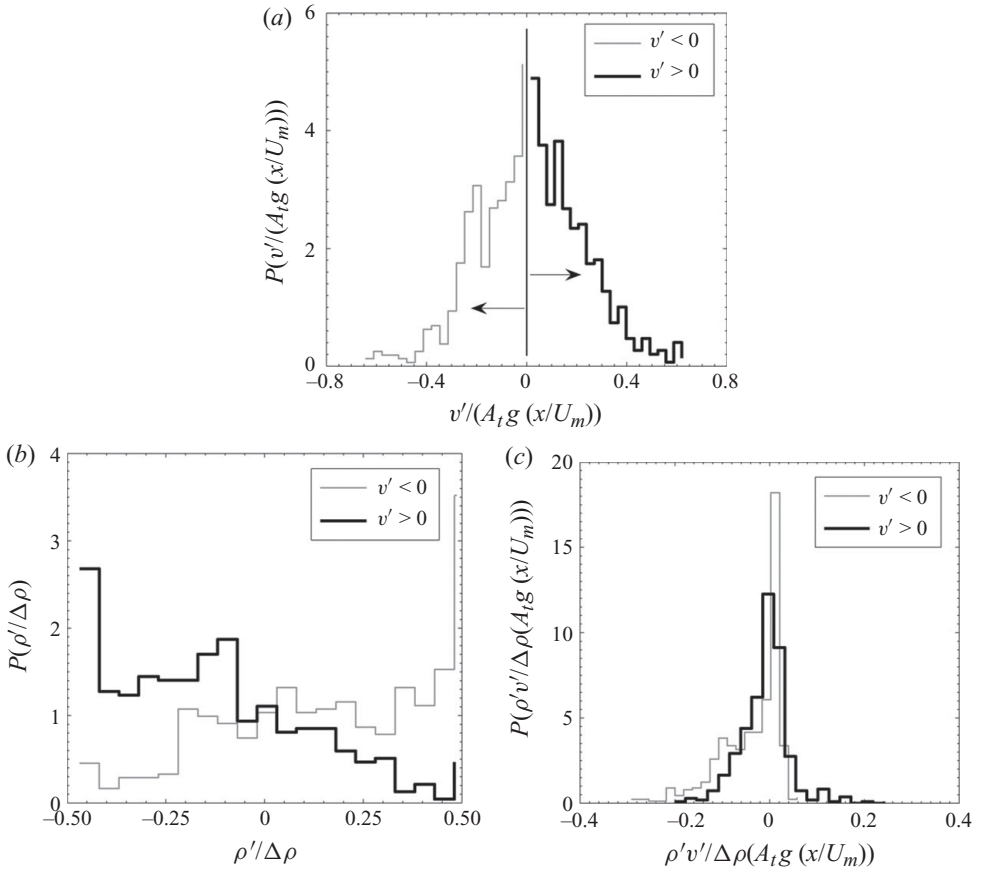

FIGURE 41. P.d.f. of ρ', v' and $\rho' v'$ at the mixing layer centreline for $A_t = 0.6$ and $\tau = 0.78$, using the sampling condition of $v' < 0$ and $v' > 0$ to approximate the measured fluctuations as a bubble (rising fluid) or spike (falling fluid). The sampling condition used is illustrated in the p.d.f. of v' in (a).

the conditional averaging technique provides a powerful tool to highlight differences in high A_t mixing layers and should be used when distinction between bubble and spike dynamics needs to be made. As with the low A_t data, conditions of $v' < 0$ (falling spike) and $v' > 0$ (rising bubble) were also applied to the $A_t = 0.6$ data and conditioned statistics were calculated. Conditional p.d.f.s of ρ', v' and $\rho' v'$ are shown in figure 41(a–c). Similar to the ρ' conditioned measurements, it is observed that the $\rho' v'$ p.d.f. for each of the v' conditions are different, showing a larger negative vertical turbulent mass flux for the falling fluid (spike), where $v' < 0$. These results are summarized in table 9. The p.d.f.s of v' also demonstrated that bubbles are not completely composed of the light fluid and entrain the heavy fluid as they move up (and vice versa). Thus, it would seem advantageous to also use averages based on the conditional sampling to determine characteristics associated with the bubbles and spikes. Specifically, the characteristic velocities for bubbles and spikes are determined as

$$v_1' = \overline{v'}\big|_{v' < 0} \quad \text{and} \quad v_2' = \overline{v'}\big|_{v' > 0}, \tag{5.27}$$

where the subscripts 1 and 2 denote the heavy (spike) and light (bubble) conditions. Using these definitions, characteristic velocities for the spike and bubble dynamics for $A_t = 0.6$ at $\tau = 0.78$ are $v_1' = -0.39\ \mathrm{m\,s^{-1}}$ and $v_2' = 0.37\ \mathrm{m\,s^{-1}}$. These velocities also satisfy volume conservation for the incompressible flow at the mixing layer centreline, where approximately equal amounts of fluid 1 and 2 are found, implying that the characteristic velocities for the turbulent bubbles and spikes should be of opposite sign but approximately equal in magnitude. The magnitudes of v_1' and v_2' are also similar to $v_{rms}' = 0.44\ \mathrm{m\,s^{-1}}$ from the conventional averaging measurement. The r.m.s. of the centreline vertical velocity fluctuations would have been typically considered a relevant velocity scale for the mixing layer at low Atwood numbers, where the bubble and spike dynamics are symmetric (Ramprabhu & Andrews 2004; Banerjee & Andrews 2006). A summary of these statistics determined using the described conditioning procedures and density-weighted averages are included in table 10. The tabulated values show a dominance of the Reynolds stress in the vertical direction (direction of gravity) over the horizontal direction for both the conventional and conditional measurements. In addition, the off-diagonal Reynolds stress component is small when compared with the diagonal components, due to symmetry of the mushroom-shaped plumes.

This framework can be further extended to include the vertical turbulent mass flux, where the conventional miscible measurement is denoted by the subscript 0,

$$a_0 = \frac{\overline{\rho' v'}}{\overline{\rho}}. \tag{5.28}$$

The quantity a_0 is a fundamental parameter for variable density turbulence models such as the BHR model (Besnard *et al.* 1992). Steinkamp (1995) derived a two-fluid definition for the turbulent mass flux (immiscible case),

$$a_2 = \frac{f_{v,1} f_{v,2} (\rho_1 - \rho_2)(v_1' - v_2')}{\overline{\rho}}. \tag{5.29}$$

It is useful to delineate differences in the vertical turbulent mass flux between the miscible (experimental) and immiscible (two-fluid) approaches to buoyancy-driven turbulence. From the miscible $A_t = 0.03$ case summarized in table 8, the turbulent mass flux parameters are $a_0 = -0.0014$ and $a_2 = -0.0021$. A lower value of a_0 illustrates that molecular mixing in the current experiment reduces the magnitude of the turbulent mass flux when compared with an idealized immiscible two-fluid mixing layer. This is also observed in the $A_t = 0.6$ case summarized in table 9, which gives $a_0 = -0.070$ and $a_2 = -0.12$. Following the analysis in our θ definition, we identify a mixing parameter based on the vertical turbulent mass flux as follows:

$$\kappa = 1 - \frac{a_0}{a_2}, \tag{5.30}$$

where $\kappa = 1$ when a_0 is zero (e.g. when the mixing layer is completely molecularly mixed), and $\kappa = 0$ when $a_0 = a_2$ when there is only interpenetration of the heavy and light fluids but no molecular mixing (immiscible two-fluid case). For the measurements summarized in tables 8 and 9 for $A_t = 0.03$ and $A_t = 0.6$, the values of the turbulent mixing parameter κ are 0.33 and 0.42, respectively. This conditioning procedure has been extended to the remaining experimental measurements at the mixing layer centreline to determine the values of κ. Figure 42 includes these results for both the $A_t = 0.03$ and $A_t = 0.6$ data sets plotted versus τ and Reynolds number $[Re_{v'} = (h_b + h_s) v_{rms}'/\upsilon_{mix}]$. The molecular mixing parameter, θ, is also shown for comparison. The

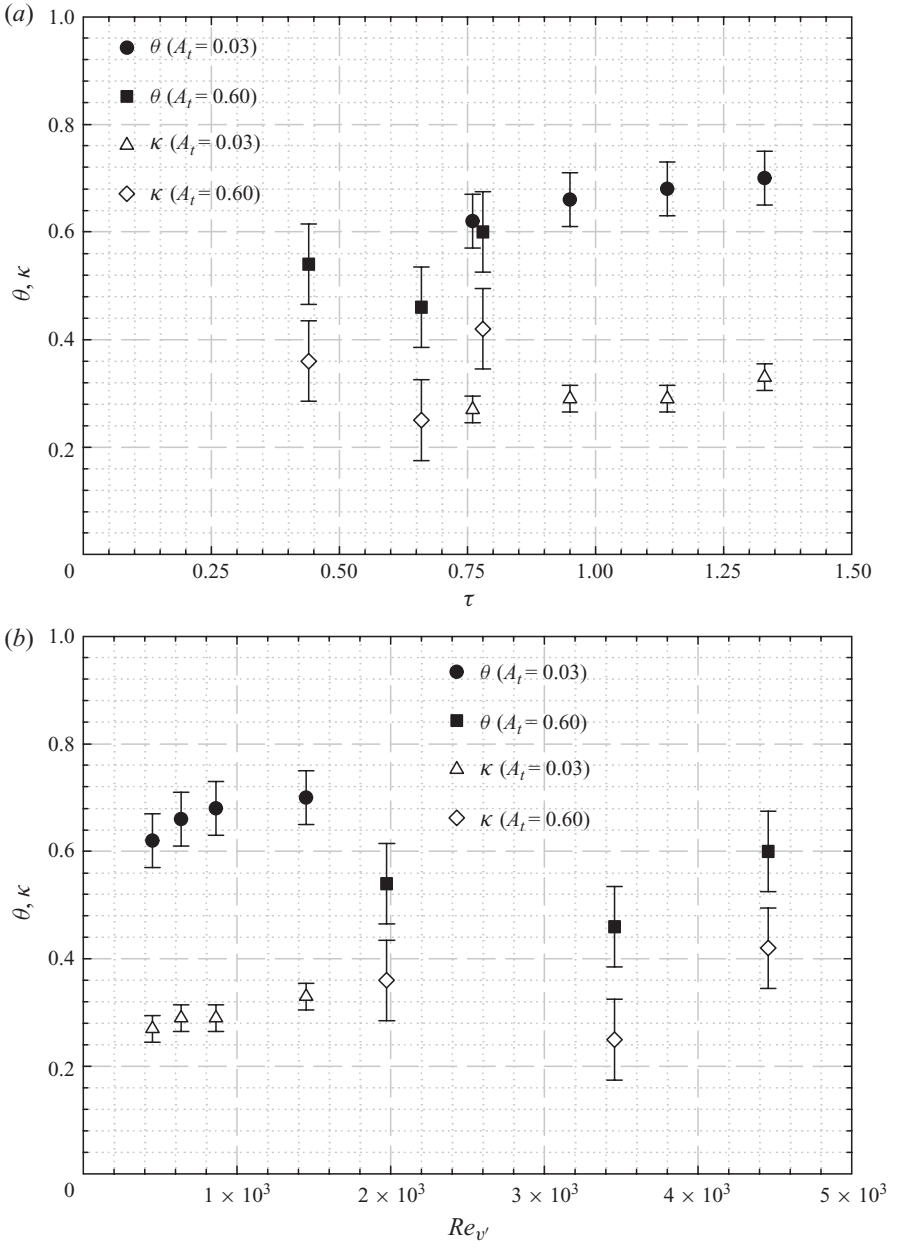

FIGURE 42. Evolution of the turbulent mass flux mixing parameter, κ, at the mixing layer centreline for $A_t = 0.03$ and $A_t = 0.6$ plotted versus τ and Reynolds number. The molecular mixing parameter, θ, is also shown for comparison.

average turbulent mass flux mixing parameter for all experiments at the mixing layer centreline is $\kappa = 0.32$, which is smaller than the measurements of $\theta = 0.70$ at late time. The differing magnitudes of the two measures of mixing, κ and θ, implies that the two mixing parameters capture different physical effects within the mixing process. The turbulent mass flux mixing parameter, κ, relies on measurement of $\overline{\rho' v'}$, which is directly related to the growth of the mixing layer and production of

turbulent kinetic energy. Coupling between the vertical velocity fluctuation, v'_{rms}, and the density fluctuation comes through buoyancy. Such buoyancy coupling is a dynamic effect giving rise to an acceleration of RT plumes, which in turn feel the effect of drag and shear. Inspection of figure 42 shows a time delay for κ compared with θ, and we attribute the delay to the acceleration and drag on the velocity fluctuation. Therefore, the turbulent mass flux mixing parameter, κ, provides an alternative method for examining turbulent mixing in Rayleigh–Taylor mixing layers, which has more direct physical connections to the self-similar and buoyancy-driven growth of the mixing layer.

6. Conclusions

The present air–helium gas channel experiment has been used to study the development of RT mixing, and experimental measurements have been reported for Atwood numbers ranging from 0.03 to 0.6. The experiment places a heavy fluid (air) over a light fluid (air/helium) with a long duration to study the resultant RT mixing. To eliminate gravity currents that develop for $A_t > 0.1$, the exit plenum was redesigned from previous work by introducing an exit splitter plate that served to prevent heavy fluid from falling in the exit plenum and forming gravity currents that flowed back into the channel. Diagnostics used include digital image analysis and hot-wire anemometry. We report measured density profiles (using digital image analysis) across the RT mixing layer at Atwood numbers of 0.04, 0.26, 0.47 and 0.6. The self-similarity growth rate parameters α_b and α_s of (1.1) exhibit the same trend as in the LEM experiments. The growth rate parameter for the spikes increases from a value of $\alpha_s = \alpha_b = 0.068 \pm 0.005$ at the $A_t = 0.04$ experiment to a value of $\alpha_s = 0.081 \pm 0.009$ at the large $A_t = 0.6$ experiment. Various definitions used over the last decade for measuring the growth parameter α were explored. It was found that α measured by using a virtual origin technique, based on half-mix-width data (Snider & Andrews 1994), was identical to the value measured by using a self-similar analysis (Ristorcelli & Clark 2004). Other definitions were also compared and cross-related, including a moving window technique to obtain a second-order best fit line through the half-mix-width data (Banerjee & Andrews 2006), and a growth parameter based on centreline velocity fluctuations (Ramaprabhu & Andrews 2004). It was found that although the above definitions gave different values of the growth parameter at early times, once the flow becomes self-similar they all gave closely similar values of α of $\alpha_{b,VO} = 0.069$, $\alpha_{b,MW} = 0.065$, $\alpha_{b,RC} = 0.068$ and $\alpha_{CL} = 0.067$, respectively.

Two hot-wire flow diagnostics were developed to measure turbulence and mixing statistics in the RT mixing layer. The first hot-wire diagnostic uses an MPMO single-wire technique, and is based on evaluating the wire response function to variations in density, velocity and orientation, and gives time-averaged statistics inside the mixing layer. The second hot-wire diagnostic utilizes the concept of temperature as a fluid marker, and employs an S3WCA technique to measure both time-averaged and instantaneous statistics. Both of these diagnostics have been used in a low-Atwood-number ($A_t \leqslant 0.04$), small density difference regime, which allowed validation of the diagnostics with similar experiments done in a hot-water/cold-water water channel facility. The MPMO method was found to be limited to $A_t < 0.25$ because it assumes a linear voltage–density response that fails to account for a nonlinear voltage–density response when $A_t > 0.25$. The S3WCA method was used to report the first detailed statistical measurements in a large-Atwood-number ($A_t = 0.6$) RT mixing layer. From

our hot-wire measurements, it was observed that the internal structure of the self-similar RT mixing layer is anisotropic, with vertical r.m.s. velocity fluctuation v'_{rms} dominating the horizontal (streamwise and transverse) u'_{rms} and w'_{rms} components. The ratio of v'_{rms}/u'_{rms} was measured as $\sim$1.8, and appears to be constant across the RT mixing layer, supporting the observation that mushroom-shaped structures are convected up and down the RT mixing layer with little change in shape. An energy budget analysis using the measured data showed a 48 % kinetic energy dissipation at $A_t = 0.04$, which was attributed to the presence of highly three-dimensional structures at all scales of the flow. This value for our air–helium experiment compares well with the hot/cold water channel value of 49 %. Similarly at $A_t = 0.04$, the molecular mix fraction, θ, was determined to be $\sim$0.70 in the self-similar region, and approximately constant across the mix. The primary momentum turbulent transport flux $\overline{\rho' v'}$ has been used in conjunction with the gradient diffusion hypothesis to obtain measurements of the gradient diffusion model constant C_μ as 0.288. The integrated dissipation D (from an energy budget) was also used in a mixing-length model to check the value of C_μ and was measured as 0.26 in good agreement with the gradient diffusion value. Additional statistical data have also been presented for cross-correlation mix profiles that may be used to validate direct numerical simulations and turbulence models such as the Reynolds stress/Boussinesq models, spectral transport model and two-fluid models of RT mixing.

Also reported for the first time experimentally are instantaneous measurements of the vertical turbulent mass flux for a Rayleigh–Taylor mixing layer, $\overline{\rho' v'}$. At the centreline of the mixing layer for $A_t = 0.03$, where production of turbulent kinetic energy is at its maximum, the p.d.f. of the primary turbulent mass flux is significantly skewed. Rather than being symmetric about a flux of zero, as found with the horizontal turbulent mass fluxes, the vertical turbulent mass flux is likely to be negative, with a narrow peak at zero associated with mixed fluid. The likelihood of large negative turbulent mass fluxes decreases away from the mixing layer centreline as the production of turbulent kinetic energy decreases and smaller average turbulent mass fluxes are found. The universal p.d.f. of $\rho' v'$ at the mixing layer centreline was found for non-dimensional times $\tau = 0.76$–1.33 at low Atwood number when the turbulent mass flux was non-dimensionalized using a velocity scale of $A_t g x / U_m$ and $\Delta\rho$ as the corresponding density scale. The energy density spectra for $\rho' v'$ was measured experimentally for the first time in a Rayleigh–Taylor mixing layer. For the non-dimensional times measured, the distribution of energy for fluctuations of the primary turbulent mass flux closely follows the behaviour of the turbulent fluctuations of the vertical velocity component. This illustrates the importance of the velocity spectrum for its influence on $\rho' v'$ and the role of the vertical turbulent mass flux on the growth of the mixing layer.

The S3WCA diagnostic was successfully used at $A_t = 0.6$ to obtain the first statistical experimental measurements of $\overline{v'^2}$, $\overline{w'^2}$, $\overline{\rho'^2}$ and $\overline{\rho' v'}$ at a large Atwood number. However, special considerations had to be made that limit the performance of the diagnostic. Measured time-averaged statistics of the velocity and density fluctuations at the mixing layer centreline from $0.44 \leqslant \tau \leqslant 0.78$ agree well with small-Atwood-number ($A_t \leqslant 0.04$) results when non-dimensionalized with self-similar velocity and density scales. Although conventional time-averaging did not illustrate the uniqueness of large-Atwood-number turbulence, conditional statistics highlight differences in the mixing layer resulting from the developing asymmetry. In particular, a larger turbulent mass flux, $\overline{\rho' v'}$, and larger vertical velocity fluctuations are observed for the downward-moving spikes. Conditional statistics based on the sign of the vertical

velocity fluctuations effectively separated the dynamics of the mixing layer into the bubble and spike dynamics. Using density-weighted averages of the bubble and spike distributions may provide a basis for describing the non-Boussinesq turbulent flow. An interesting consequence of using conditional analysis is the ability to identify a new turbulent mixing parameter based on the vertical turbulent mass flux, which is similar to the molecular mixing parameter, θ, defined for the density variance. This turbulent mass flux mixing parameter, κ, relies on measurement of $\overline{\rho' v'}$, which is directly related to the growth of the mixing layer and production of turbulent kinetic energy and may provide an alternative method for examining turbulent mixing in Rayleigh–Taylor mixing layers, which has more direct physical connections to the self-similar and buoyancy-driven growth of the mixing layer. The use of conditional statistics allows for measurement of the turbulent mass flux for both the miscible and the corresponding immiscible case.

This paper is based upon the work that is supported by the US Department of Energy under contract number DE-FG03-02NA00060. The authors thank Nicholas Mueschke and Michael Peart for their help in the visualization analysis and construction of the facility.

REFERENCES

Allred, J. C. & Blount, G. H. 1954 Experimental studies of Taylor instability. Report LA-I-600, University of California.

Andreopoulos, J. 1983 Statistical errors associated with probe geometry and turbulence intensity in triple hot-wire anemometry. *J. Phys.* E *Sci. Instrum.* **16**, 1264–1271.

Andrews, M. J. 1986 Turbulent mixing by Rayleigh–Taylor instability. PhD thesis, Imperial College of Science and Technology, London.

Andrews, M. J. & Spalding, D. B. 1990 A simple experiment to investigate two-dimensional mixing by Rayleigh–Taylor instability. *Phys. Fluids* A **2**, 922–927.

Antonia, R. A. 1981 Conditional sampling in turbulence measurement. *Annu. Rev. Fluid Mech.* **13**, 131–156.

Anuchina, N. N., Kucherenko, Y. A., Neuvazhaev, V. E., Ogibina, V. N. & Shibarshov, L. I. 1978 Turbulent mixing at an accelerating interface between liquids of different densities. Translated from *Izv. Akad. Nauk SSSR Mekh. Zhidk. Gaza* **6**, 157–160.

Atzeni, S. & Meyer-ter-Vehn, J. 2004 The physics of inertial fusion: beam plasma interaction, hydrodynamics, hot dense matter. In *International Monographs on Physics* (ed. J. Birman, S. F. Edwards, R. Friend, M. Rees, D. Sherrington & G. Veneziano), vol. 125, pp. 129–194. Oxford University Press.

Banerjee, A. 2006 Statistically steady measurements of Rayleigh–Taylor mixing in a gas channel. PhD dissertation, Texas A&M University, College Station, TX.

Banerjee, A. & Andrews, M. J. 2006 Statistically steady measurements of Rayleigh–Taylor mixing in a gas channel. *Phys. Fluids* **18**, 035107.

Banerjee, A. & Andrews, M. J. 2007 A convection heat transfer correlation for a binary air–helium mixture at low Reynolds number. *J. Heat Transfer* **129**, 1494–1505.

Besnard, D. C., Harlow, F. H., Rauenzahn, R. M. & Zemach, C. 1992 Turbulence transport equations for variable-density turbulence and their relationship to two-field models. *Tech. Rep.* LAUR-12303. Los Alamos National Laboratory.

Betti, R., Umansky, M., Lobatchev, V., Goncharov, V. N. & McCrory, R. L. 2001 Hot-spot dynamics and deceleration-phase Rayleigh–Taylor instability of imploding inertial confinement fusion capsules. *Phys. Plasmas* **8**, 5257–5267.

Blackwell, B. F. 1973 The turbulent boundary layer on a porous plate: an experimental study of the heat transfer behaviour with adverse pressure gradients. PhD dissertation, Stanford University, Stanford, CA.

Browand, F. K. & Weidman, P. D. 1976 Large scales in the developing mixing layer. *J. Fluid Mech.* **76**, 127–144.

Brown, G. L. & Roshko, A. 1974 On density effects and large structures in turbulent mixing layers. *J. Fluid Mech.* **64**, 775–816.

Bruun, H. H. 1972 Hot-wire corrections in low and high turbulence intensity flows. *J. Phys.* E *Sci. Instrum.* **5**, 812–818.

Bruun, H. H. 1995 *Hot-Wire Anemometry*. Oxford University Press.

Chandrasekhar, S. 1961 *Hydrodynamic and Hydromagnetic Stability*. Dover.

Chassaing, P., Antonia, R. A., Anselmet, F., Joly, L. & Sarkar, S. 2002 Variable density fluid turbulence. In *Fluid Mechanics and its Applications* (ed. R. Moreau), vol. 69, pp. 79–117. Kluwer Academic.

Clarke, J. S., Fisher, H. N. & Mason, R. J. 1973 Laser-driven implosion of spherical DT targets to thermonuclear burn conditions. *Phys. Rev. Lett.* **30**, 89–92.

Cole, R. L. & Tankin, R. S. 1973 Experimental study of Taylor instability. *Phys. Fluids* **16**, 1810–1820.

Cook, A. W. & Cabot, W. 2006 Reynolds number effects on Rayleigh–Taylor instability with possible implications for type-Ia supernovae. *Nat. Phys.* **2**, 562–568.

Cook, A. W., Cabot, W. & Miller, P. L. 2004 The mixing transition in Rayleigh–Taylor instability. *J. Fluid Mech.* **511**, 333–362.

Cook, A. W. & Dimotakis, P. E. 2001 Transition stages of Rayleigh–Taylor instability between miscible fluids. *J. Fluid Mech.* **443**, 69–99. Corrigendum. 2002 *J. Fluid Mech.* **457**, 410–411.

Corrsin, S. 1949 Extended applications of the hot-wire anemometer. *Tech. Rep.* TA 1864. NACA.

Cui, A. Q. & Street, R. L. 2004 Large-eddy simulation of coastal upwelling flow. *Environ. Fluid Mech.* **4**, 197–223.

Daly, B. J. 1967 Numerical study of two-fluid Rayleigh–Taylor instability. *Phys. Fluids* **10**, 297–307.

Dalziel, S. B., Linden, P. F. & Youngs, D. L. 1999 Self-similarity and internal structure of turbulence induced by Rayleigh–Taylor instability. *J. Fluid Mech.* **399**, 1–48.

Danckwerts, P. V. 1952 The definition and measurement of some characteristics of mixtures. *Appl. Sci. Res.* **3**, 279–296.

Dimonte, G. & Schneider, M. 1996 Turbulent Rayleigh–Taylor instability experiments with variable acceleration. *Phys. Rev.* E **54**, 3740–3743.

Dimonte, G. & Schneider, M. 2000 Density ratio dependence of Rayleigh–Taylor mixing for sustained and impulsive acceleration histories. *Phys. Fluids* **12**, 304–321.

Dimonte, G., Youngs, D. L., Dimits, A., Weber, S., Marinak, M., Wunsch, S., Garasi, C., Robinson, A., Andrews, M. J., Ramaprabhu, P., Calder, A. C., Fryxell, B., Biello, J., Dursi, L., Macneice, P., Olson, K., Ricker, P., Rosner, R., Timmes, H., Tufo, H., Young, Y.-N. & Zingale, M. 2004 A comparative study of the turbulent Rayleigh–Taylor (RT) instability using high-resolution 3D numerical simulations: the Alpha-Group collaboration. *Phys. Fluids* **16**, 1668–1693.

Dimotakis, P. 2000 The mixing transition in turbulent flows. *J. Fluid Mech.* **409**, 69–98.

Dimotakis, P. 2005 Turbulent mixing. *Annu. Rev. Fluid Mech.* **37**, 329–356.

Eckart, C. 1948 An analysis of stirring and mixing processes in incompressible fluids. *J. Mar. Res.* **7**, 265–275.

Emmons, H. W., Chang, C. T. & Watson, B. C. 1960 Taylor instability of finite surface waves. *J. Fluid Mech.* **7**, 177–193.

Fabris, G. 1983*a* Third-order conditional transport correlations in the two-dimensional turbulent wake. *Phys. Fluids* **26**, 423–427.

Fabris, G. 1983*b* Higher-order statistics of turbulent fluctuations in the plane wake. *Phys. Fluids* **26**, 1437–1445.

Fox, R. O. 2003 *Computational Models for Turbulent Reacting Flows*. Cambridge University Press.

Frota, M. N. & Moffat, R. J. 1983 Effect of combined roll and pitch angles on triple hot-wire measurements of mean and turbulence structure. *DISA Inf.* **28**, 15–23.

Goncharov, V. N. 2002 Analytical model of nonlinear, single mode, classical Rayleigh–Taylor instability at arbitrary Atwood numbers. *Phys. Rev. Lett.* **88**, 134502.

Gull, S. F. 1975 The X-ray, optical and radio properties of young supernova remnants. *R. Astron. Soc. Mon. Not.* **171**, 263–278.

Hishida, M. & Nagano, Y. 1978 Simultaneous measurements of velocity and temperature in nonisothermal flows. *Trans. ASME J. Heat Transfer* **100**, 340–345.

Jacobsen, R. T., Clarke, W. P., Penoncello, S. G. & McCarty, R. D. 1990 A thermodynamic property formulation for air. Part I. Single-phase equation of state from 60 to 873 K at pressures to 70 MPa. *Intl J. Thermophys.* **11**, 169–177.

Jitschin, W., Weber, U. & Hartmann, H. K. 1995 Convenient primary gas flow meter. *Vacuum* **46**, 821–824.

John, J. E. A. 1984 *Gas Dynamics*. Prentice-Hall.

Jorgenson, F. E. 1971 Directional sensitivity of wire and fibre-film probes. *DISA Info* **11**, 31–37.

Koop, G. K. 1976 Instability and turbulence in a stratified shear layer. PhD dissertation, University of Southern California, Los Angeles, CA.

Kovasznay, L. S. G. 1950 The hot-wire anemometer in supersonic flow. *J. Aerosp. Sci.*, **17**, 565–572.

Kraft, W. N. 2008 Simultaneous and instantaneous measurements of velocity and density in Rayleigh–Taylor mixing layers. PhD dissertation, Texas A&M University, College Station, TX.

Kraft, W. N., Banerjee, A. & Andrews, M. J. 2009 On hot-wire diagnostics in Rayleigh–Taylor mixing layers. *Experiments in Fluids* **47**, 49–68.

Kucherenko, Y. A., Balabin, S. I., Cherret, R. & Haas, J. F. 1997 Experimental investigation into inertial properties of Rayleigh–Taylor turbulence. *Laser and Particle Beams* **15**, 25–31.

LaRue, J. C. & Libby, P. A. 1980 Further results related to the turbulent boundary layer with slot injection of helium. *Phys. Fluids* **23**, 1111–1118.

Launder, B. E. & Spalding, D. B. 1974 The numerical computation of turbulent flows. *Comput. Methods Appl. Mech. Engng* **3**, 269–289.

Leicht, K. A. 1997 Effects of initial conditions on Rayleigh–Taylor mixing development. MS thesis, Texas A&M University, College Station, TX.

Lewis, D. J. 1950 The instability of liquid surfaces when accelerated in a direction perpendicular to their planes. Part 2. *Proc. R. Soc. Lond.* **202**, 81–96.

Linden, P. F., Redondo, J. M. & Caulfield, C. P. 1992 Molecular mixing in Rayleigh–Taylor instability. In *Advances in Compressible Turbulent Mixing* (ed. W. P. Dannevik, A. C. Buckingham & C. E. Leith), pp. 95–104. Princeton University.

Linden, P. F., Redondo, J. M. & Youngs, D. L. 1994 Molecular mixing in Rayleigh–Taylor instability. *J. Fluid Mech.* **265**, 97–124.

Loehrke, R. I. & Nagib, H. M. 1972 Experiments on management of free-stream turbulence. *Tech. Rep.* AGARD Report 598. Illinois Institute of Technology.

Marmottant, P. & Villermaux, E. 2004 On spray formation. *J. Fluid Mech.* **498**, 73–111.

McCarty, R. 1973 Thermodynamic properties of helium 4 from 2 to 1500 K at pressures up to 108 Pa. *J. Phys. Chem. Ref. Data* **2**, 923–1042.

Molchanov, O. A. 2004 On the origin of low- and middle-latitude ionospheric turbulence. *Phys. Chem. Earth* **29**, 559–567.

Mueschke, N. J. & Andrews, M. J. 2006 Investigation of scalar measurement error in diffusion and mixing processes. *Exp. Fluids* **40**, 165–175. Erratum. *Exp. Fluids* **40**, 176 (2006).

Mueschke, N., Andrews, M. J. & Schilling, O. 2006 Experimental characterization of initial conditions and spatio-temporal evolution of a small Atwood number Rayleigh–Taylor mixing layer. *J. Fluid Mech.* **567**, 27–63.

Mueschke, N., Schilling, O., Youngs, D. L. & Andrews, M. J. 2009 Measurements of molecular mixing in a high-Schmidt-number Rayleigh–Taylor mixing layer. *J. Fluid Mech.* **632**, 17–48.

Mydlarski, L. 2003 Mixed velocity-passive scalar statistics in high-Reynolds-number turbulence. *J. Fluid Mech.* **475**, 173–203.

Pope, S. B. 2000 *Turbulent Flows*. Cambridge University Press.

Ramaprabhu, P. & Andrews, M. J. 2003 Simultaneous measurements of velocity and density in buoyancy-driven mixing. *Exp. Fluids* **34**, 98–106.

Ramaprabhu, P. & Andrews, M. J. 2004 Experimental investigation of Rayleigh–Taylor mixing at small Atwood numbers. *J. Fluid Mech.* **502**, 233–271.

Ratafia, M. 1973 Experimental investigation of Rayleigh–Taylor instability. *Phys. Fluids* **16**, 1207–1210.

Rayleigh, Lord 1884 Investigation of the equilibrium of an incompressible heavy fluid of variable density. *Proc. Lond. Math. Soc.* **14**, 170–177.

Read, K. I. 1984 Experimental investigation of turbulent mixing by Rayleigh–Taylor instability. *Physica* D **12**, 45–58.

Ristorcelli, J. R. & Clark, T. T. 2004 Rayleigh–Taylor turbulence: self-similar analysis and direct numerical simulations. *J. Fluid Mech.* **507**, 213–253.

Rose, W. C. 1973 The behaviour of a compressible turbulent boundary layer in a shock-wave-induced adverse pressure gradient. PhD dissertation, University of Washington, Seattle, Washington.

Sharp, D. H. 1984 An overview of Rayleigh–Taylor Instability. *Physica* D **12**, 3–10.

Snider, D. M. 1994 A study of buoyancy and shear mixing. PhD dissertation, Texas A&M University, College Station, TX.

Snider, D. M. & Andrews, M. J. 1994 Rayleigh–Taylor and shear driven mixing with an unstable thermal stratification. *Phys. Fluids* **6**, 3324–3334.

Snider, D. M. & Andrews, M. J. 1996 The simulation of mixing layers driven by compound buoyancy and shear. *J. Fluids Engng* **118**, 370–376.

Speziale, C. G. 1991 Analytical methods for the development of Reynolds-stress closures in turbulence. *Annu. Rev. Fluid. Mech.* **23**, 107–157.

Steinkamp, M. J. 1995 Spectral analysis of the turbulent mixing of two fluids. PhD dissertation, University of Illinois, Urbana, IL.

Steinkamp, M. J., Clark, T. & Harlow, F. H. 1995 Stochastic interpenetration of fluids. *Tech Rep.* LA-131016. Los Alamos National Laboratory.

Stillinger, D. C., Head, M. J., Helland, K. N. & Van Atta, C. W. 1983 A closed-loop gravity-driven water channel for density-stratified flow. *J. Fluid Mech.* **131**, 73–89.

Tan-Atichat, J., Nagib, H. M. & Loehrke, R. I. 1982 Interaction of free-stream turbulence with screens and grids: a balance between turbulence scales. *J. Fluid Mech.* **114**, 501–528.

Taylor, G. I. 1938 The spectrum of turbulence. *Proc. R. Soc. Lond. Ser.* A **164**, 476–490.

Taylor, G. I. 1950 The instability of liquid surfaces when accelerated in a direction perpendicular to their planes. *Proc. R. Soc. Lond.* **201**, 192–196.

Vukoslavcevic, P. V., Radulovic, I. M. & Wallace, J. M. 2005 Testing of a hot- and cold-wire probe to measure simultaneously the speed and temperature in supercritical CO_2 flow. *Exp. Fluids* **3**, 703–711.

White, F. M. 1991 *Viscous Fluid Flow*. McGraw-Hill.

Wilke, C. R. 1950 A viscosity equation for gas mixtures. *J. Chem. Phys.* **18**, 517–519.

Wilson, P. N. & Andrews, M. J. 2002 Spectral measurements of Rayleigh–Taylor mixing at low Atwood number. *Phys. Fluids* A **14**, 938–945.

Wygnanski, I. & Fiedler, H. E. 1970 The two-dimensional mixing region. *J. Fluid Mech.* **41**, 327–361.

Youngs, D. L. 1984 Numerical simulation of turbulent mixing by Rayleigh–Taylor instability. *Physica* D **12**, 32–44.

Youngs, D. L. 1989 Modelling turbulent mixing by Rayleigh–Taylor instability. *Physica* D **37**, 270–287.

Youngs, D. L. 1991 Three-dimensional numerical simulation of turbulent mixing by Rayleigh–Taylor instability. *Phys. Fluids* A **3**, 1312–1320.

Youngs, D. L. 1994 Numerical simulation of mixing by Rayleigh–Taylor and Richtmyer–Meshkov instabilities. *Laser Part. Beams* **12**, 725–750.

Youngs, D. L. 2003 Application of MILES to Rayleigh–Taylor and Richtmeyer–Meshkov mixing. In *Sixteenth AIAA Computational Fluid Dynamics Conference*. Tech. Rep. no. 4102.